

École doctorale n° 432 : Sciences des Métiers de l'ingénieur

Doctorat

T H È S E

pour obtenir le grade de docteur délivré par

l'École Nationale Supérieure d'Arts et Métiers

Spécialité “ Mécanique - matériaux ”

présentée et soutenue publiquement par

Bin JIA

le 11 décembre 2019

**Experimental characterization and behavior modelling of 304
stainless steel under various strain rates and temperatures**

Superviseurs de thèse : **Alexis RUSINEK, Raphaël PESCI, Tudor BALAN**

Jury

M. Francis COLLOMBET, Professeur, MSC, IUT GMP de Toulouse
M. Eric MARKIEWICZ, Professeur, LAMIH, Université Polytechnique Hauts-de-France
M. Ramón ZAERA POLO, Professeur, University Carlos III, Madrid
Mme. Teresa FRAS, Attachée de recherches, ISL Saint-Louis
M. Alexis RUSINEK, Professeur, LEM3, Université de Lorraine, Metz
M. Raphaël PESCI, Maître de conférences, LEM3, Arts et Métiers ParisTech, Metz
M. Tudor BALAN, Maître de conférences HDR, LCFC, Arts et Métiers ParisTech, Metz

Président
Rapporteur
Rapporteur
Examineur
Examineur
Examineur
Examineur

**T
H
È
S
E**

To my beloved parents for their sacrifices

To my beloved sister for her support

To my dear supervisors for their guidance

To all my dear friends for their help

Acknowledgements

The work has been conducted in Laboratory LEM3 (Laboratoire d'Étude des Microstructures et de Mécanique des Matériaux) and Laboratory LCFC (Laboratoire de Conception Fabrication Commande) in Metz Campus of ENSAM (École Nationale Supérieure et d'Arts et Métiers). Here, I want to thank everyone who has helped me during the past three years.

First of all, I want to thank my thesis supervisors Alexis RUSINEK, Raphaël PESCI and Tudor BALAN, who gave me the opportunity to pursue a doctor degree. I am grateful for their dedicated support, kind guidance and invaluable advice. Without them, it is impossible for me to complete the thesis. It is really a pleasure for me to work here with them for such a long time.

I sincerely thank Prof. Francis COLLOMBET from IUT GMP de Toulouse for being the president of my PhD thesis committee. I would like to express my gratitude to the two reporters, Prof. Eric MARKIEWICZ from Université Polytechnique Hauts-de-France and Prof. Ramon ZAERA from Universidad Carlos III de Madrid, for their insightful comments and inspiring reports. I am deeply grateful to Dr Teresa FRAS from ISL Saint-Louis, for accepting the invitation and taking her precious time to attend my thesis defense. It is my honor to be able to invite such famous and knowledgeable researchers as the referees.

I would like to thank the China Scholarship Council (CSC) for providing the scholarship (Grant 201606220056) to support my study in ENSAM, France.

Special thanks to my two colleagues, Richard BERNIER and Slim BAHI. Thank you for your continual support of my experiments and the detailed discussion. You really help me a lot with my thesis. In addition, I would like to thank all my colleagues in the two labs, Anne-Laure LEBAUDY, Boris PIOTROWSKI, Christophe LESCALIER, Denis BOUSCAUD, Francois CRISTOFARI, Laurent PELTIER, Marc WARY, Patrick MOLL, Stéphanie SCHIAPPA, Pierre SIMON etc., and also my Chinese friends, Fan LI, Haitao TIAN, Jianchang ZHU, Peng WANG, Qing XIA, Tian ZHANG, Xianqiong ZHAO, Yanfeng YANG, Zhicheng HUANG, Zhaozhi LONG, as

well as my girlfriend Xuan WU, with whom I shared the unforgettable daily life memory in Metz.

I am extremely grateful to my family, my father Dongpan JIA, my mother Guanghua WANG, my sister Lin JIA and my uncle Guangzhen WANG. I grow up under your encouragement, support and sacrifice.

Last but not least, I also want to thank all the people who helped me and filled my life with laugh and happiness.

Table of contents

General introduction	1
Chapter 1 Literature review on deformation behavior of 304 ASS	5
1. Introduction.....	6
2. Martensitic transformation and deformation behavior of 304 ASS.....	7
<i>2.1 Martensitic transformation in 304 ASS.....</i>	<i>7</i>
<i>2.2 Deformation behavior of 304 ASS.....</i>	<i>10</i>
3. Constitutive behavior and martensitic transformation modelling in 304 ASS	13
<i>3.1 Constitutive behavior modelling of metallic alloys.....</i>	<i>13</i>
<i>3.2 Constitutive modelling of martensitic transformation</i>	<i>23</i>
4. Dynamic shear testing techniques of metallic alloys	27
<i>4.1 Dynamic shear specimens</i>	<i>28</i>
<i>4.2 Dynamic shear testing devices</i>	<i>31</i>
5. Perforation behavior of metallic alloys.....	35
<i>5.1 Effect of several parameters on perforation behavior of thin plates</i>	<i>36</i>
<i>5.2 Perforation behavior of thin plates under various temperatures.....</i>	<i>39</i>
Conclusion	41
References.....	42
Chapter 2 Thermo-viscoplastic behavior of 304 ASS.....	57
1. Introduction.....	58
2. Material behavior and set-up description.....	59
<i>2.1 Material and specimen.....</i>	<i>59</i>
<i>2.2 Quasi-static and dynamic compression tests</i>	<i>59</i>

3. Calibration and heat transfer modelling of the heating furnace/cooling device	62
4. Experimental results and discussion	68
4.1 True stress-true strain relations of 304 ASS	68
4.2 Strain rate and temperature sensitivity of 304 ASS.....	72
5. Thermo-viscoplastic behavior modelling of 304 ASS	75
5.1 The extended R-K constitutive equation.....	80
5.2 Comparison between experimental and predicted flow stress for 304 ASS.....	84
6. Conclusion	88
References.....	89
Chapter 3 A new shear testing technique for extreme high strain rates	95
1. Introduction.....	96
2. The new shear specimen	97
3. Preliminary experimental results	99
4. Numerical analysis of the new shear specimen	103
4.1 Validity of the pulse signals in dynamic shear tests.....	103
4.2 Analysis of stress state in specimen shear zone	108
4.3 Determination of shear stress-shear strain relations.....	114
5. Shear stress-shear strain relations of 304 ASS	121
6. Conclusion	127
Reference	128
Chapter 4 Perforation behavior of 304 ASS.....	131
1. Introduction.....	132
2. Material and setup description	133
2.1 Ballistic impact setup	133

2.2 Projectile and target description.....	134
2.3 Thermal chamber/cooling device for high/low temperature perforation tests	137
3. Reliability verification of the cooling device.....	140
3.1 Temperature evolution and distribution along the diagonal line of the target	141
3.2 Calibration and heat transfer modelling.....	143
4. Influence of testing temperature on the perforation process.....	147
4.1 Effect of temperature on failure mode.....	147
4.2 Effect of temperature on the ballistic curves.....	149
4.3 Effect of temperature on the energy absorption capacity	151
5. X-ray diffraction analysis of perforated specimens	155
6. Numerical simulations of the perforation process	159
6.1 Numerical model description	159
6.2 Numerical results of the ballistic curves and the fracture patterns	165
7. Conclusions.....	171
References.....	172
Conclusions.....	177
Future work.....	179

General introduction

As a representative of Transformation Induced Plasticity (TRIP) steels, 304 austenitic stainless steel (ASS) has a unique combination of high strength and high ductility. Its beneficial mechanical properties come from Strain-Induced Martensitic Transformation (SIMT), which means that upon plastic deformation the initial austenite phase (γ) transforms into stable martensite phase (α'); thus, both improved work hardening rate and significantly enhanced ductility can be achieved.

304 ASS is widely used in many engineering areas such as chemical, transportation, nuclear and aerospace industries. During working and manufacturing process, it may undergo deformation over a wide range of strain rates and temperatures; therefore, much work has been done to investigate the effects of these two parameters on the deformation behavior. The main conclusions are listed:

- Compared to the conventional metallic alloys whose deformation is dominated by dislocation slip, the temperature sensitivity of 304 ASS is strongly affected by the SIMT effect. At temperatures below M_d , the temperature below which martensitic transformation occurs automatically or can be triggered by plastic deformation, the stress-strain curves of 304 ASS exhibit an S-shape and a second hardening phenomenon is often observed. With decreasing temperature, the flow stress increases continuously and the second hardening phenomenon becomes more obvious. At temperatures above M_d , the deformation mechanism of 304 ASS changes into dislocation glide. Therefore, with increasing temperature, the strength of 304 ASS decreases without the second hardening phenomenon.

- The strain rate sensitivity of 304 stainless steel is also different from the commonly used metallic alloys. On the one hand, the transformation process is inhibited by adiabatic heating effect at high strain rates and the corresponding strain hardening rate decreases. On the other hand, due to the viscous drag effect under dynamic strain rates, a pronounced strain rate sensitivity is often observed.

Combining effects of strain rate on both dislocation slip and martensitic transformation, either positive or negative strain rate sensitivity is often observed.

Although the deformation behavior of 304 ASS has been studied massively, several scientific and engineering issues remain unclear:

- Previous studies mainly focused on quasi-static deformation at various temperatures or dynamic tests at room temperature. While the combined effects of temperature and dynamic loading on mechanical properties of 304 ASS are frequently encountered, the corresponding deformation behavior is not clearly understood.

- Due to the unique combination of elevated strength and high ductility, 304 ASS is widely used in energy absorption and crashworthiness areas. It may also be subjected to high strain rates ($\geq 10^4 \text{ s}^{-1}$) during processes such as high speed machining and ballistic impact especially under various temperatures. Few works for ballistic impact can be found in literature: the corresponding deformation behavior and the failure mechanisms remain imprecise.

This thesis aims to study the deformation behavior of 304 ASS under different strain rates and temperatures, with special focuses on the two issues mentioned above. The objective is divided into several parts. The first goal is to obtain the thermo-viscoplastic behavior of 304 ASS under various strain rates and temperatures both experimentally and by constitutive modelling. The second is to study the deformation behavior of 304 ASS under extreme high strain rates with a newly developed shear specimen. Finally, the perforation behavior of 304 ASS under various velocities and temperatures is investigated experimentally and numerical simulations are conducted and compared to the experimental results.

Chapter 1 is based on a literature review on the deformation behavior of 304 ASS under different strain rates and temperatures. The focus is made on four parts:

first, martensitic transformation and deformation behavior of 304 ASS under different strain rates and temperatures; second, constitutive behavior and martensitic transformation modelling of 304 ASS; third, several testing techniques for shear behavior study under extremely high strain rates; fourth, impact behavior of metallic alloys under various deformation conditions.

Chapter 2 presents the thermo-viscoplastic behavior study of 304 ASS. First, a home-designed heating furnace/cooling device is coupled to the conventional SHPB apparatus and the equipment reliability is verified. Compression tests of 304 ASS are conducted: the influence of temperature and strain rate on the deformation behavior of 304 ASS is presented and discussed. Then, an extension of the Rusinek-Klepaczko (RK) constitutive model considering martensitic transformation is chosen to describe the temperature and strain rate dependent deformation behavior of 304 ASS.

In chapter 3, a new shear specimen is designed and validated for dynamic shear testing of bulk materials using the conventional Split Hopkinson Pressure Bar (SHPB) system. First, the newly designed shear specimen and the corresponding shear testing technique are introduced. Then, this method is used to test the shear behavior of 304 ASS: the experimental results are presented and discussed. In the third section, the experimental stress-strain curves are compared to finite element analysis (FEA) and the stress distribution inside the shear zones are analyzed.

Chapter 4 is dedicated to the perforation behavior of 304 ASS at various velocities and temperatures. An original cooling device is developed to test the material behavior at low temperatures, and its reliability is verified. Then, ballistic impact tests are carried out under different temperatures and the experimental results are discussed, including the measurement of the volume fraction of induced martensite in perforated specimens (X-ray diffraction measurements), to explain the improved energy absorption capacity at low temperatures. In addition, numerical

simulations of perforation tests are carried out with the extended RK model introduced in chapter 2 and compared to the experimental results.

The main conclusions are summarized in the last part of the manuscript: the original scientific contribution is highlighted and some perspectives for future work are proposed.

Chapter 1 Literature review on deformation behavior of 304 ASS

1. Introduction

304 ASS is the most widely stainless steel in the world due to its unique combination of moderate strength and high ductility, Fig. 1.1. The improved mechanical properties come from the SIMT effect, Fig. 1.2. During the working and manufacturing processes, 304 ASS is frequently subjected to various deformation conditions such as strain rate, temperature and stress state. Therefore, it is interesting and necessary to study the effects of those parameters on the deformation behavior of 304 ASS.

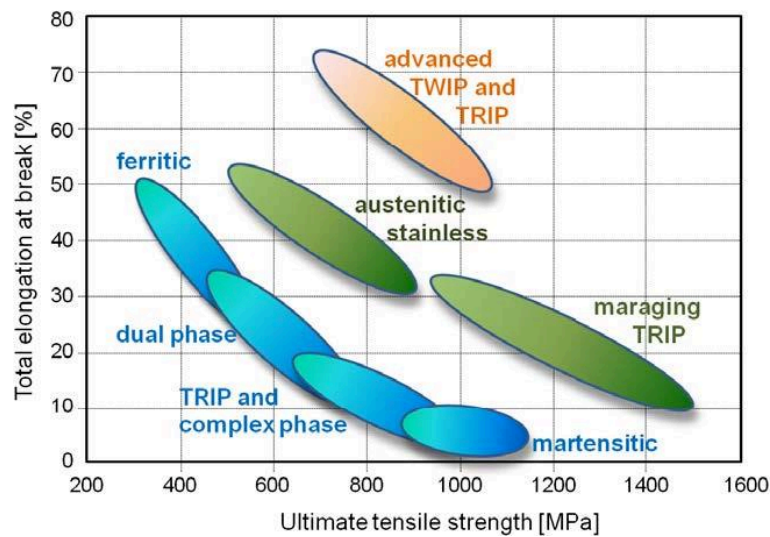


Fig. 1.1. Overview of typical strength-ductility profiles of different types of steels [1].

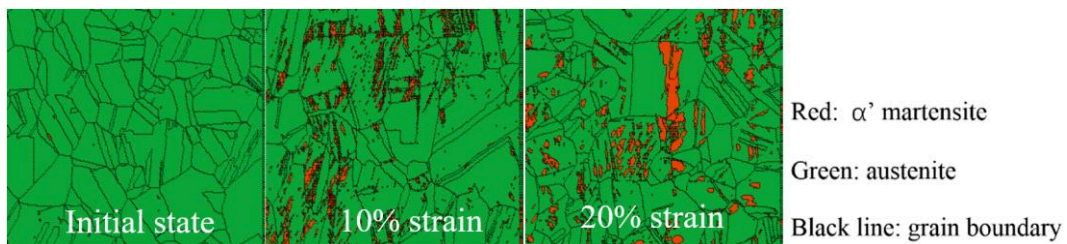


Fig. 1.2. Microstructure evolution of 304 ASS during quasi-static tension test [2].

In the past few decades, much work has been done to study the deformation and martensitic transformation behavior of 304 ASS. Many progressive conclusions

mainly about the deformation mechanism, microstructure evolution and thermo-viscoplastic behavior modelling, have been drawn. However, as is presented in the introduction part, several questions remain unclear and further researches are needed. In order to start research in this area, deformation behavior of 304 ASS under different strain rates and temperatures is reviewed in this chapter.

The literature review consists of four parts introducing the effects of temperature and strain rate on the martensitic transformation and deformation behavior of 304 ASS; constitutive behavior and martensitic transformation modelling; techniques for shear testing under extreme high strain rates and ballistic impact behavior of metallic alloys under different deformation conditions.

2. Martensitic transformation and deformation behavior of 304 ASS

2.1 Martensitic transformation in 304 ASS

Martensitic transformation is affected by several parameters including temperature [3], chemical composition [4], stress state [5], grain size [6] and strain rate [7]. Especially, much work has been done to investigate the temperature and strain rate's effects.

The effect of temperature on the martensitic transformation is shown in Fig. 1.3. M_s is the temperature below which the Gibbs free energy between the austenite phase (γ) and the martensite phase (α'), $\Delta G_{T < M_s}^{\gamma \rightarrow \alpha'}$, is high enough for martensitic transformation to occur spontaneously. At temperatures $M_s < T < M_d$, the $\Delta G_{M_s < T < M_d}^{\gamma \rightarrow \alpha'}$ is too small to trigger the martensitic transformation and an additional mechanical driving force U' is needed:

$$\Delta G_{M_s < T < M_d}^{\gamma \rightarrow \alpha'} + U' = \Delta G_{M_s}^{\gamma \rightarrow \alpha'} \quad \text{Eq. 1.1}$$

At temperatures $M_s < T < M_s^\sigma$, the mechanical driving force needed is smaller than the yield stress of the austenite phase and martensitic transformation takes place during the elastic deformation process of the austenite phase. With increasing temperature $M_s^\sigma < T < T_0$, the driving force to induce martensitic transformation exceeds the yield stress of the austenite phase and plastic deformation of austenite phase is required to supply the mechanical driving force. At temperatures $T_0 < T < M_d$, the Gibbs free energy of the two phases reverses and martensitic transformation takes place with an external mechanical driving force by $U' > \Delta G_{T_0 < T < M_d}^{\gamma \rightarrow \alpha'}$. With further increase of temperature, the mechanical driving force needed exceeds the flow stress of austenite phase and martensitic transformation does not occur anymore. The corresponding deformation mechanism changes into twinning or dislocation slip [1]. Therefore, with increasing temperature, martensitic transformation in 304 ASS is gradually suppressed, both the transformation rate and the final martensite volume fraction decrease, Fig. 1.4 [2].

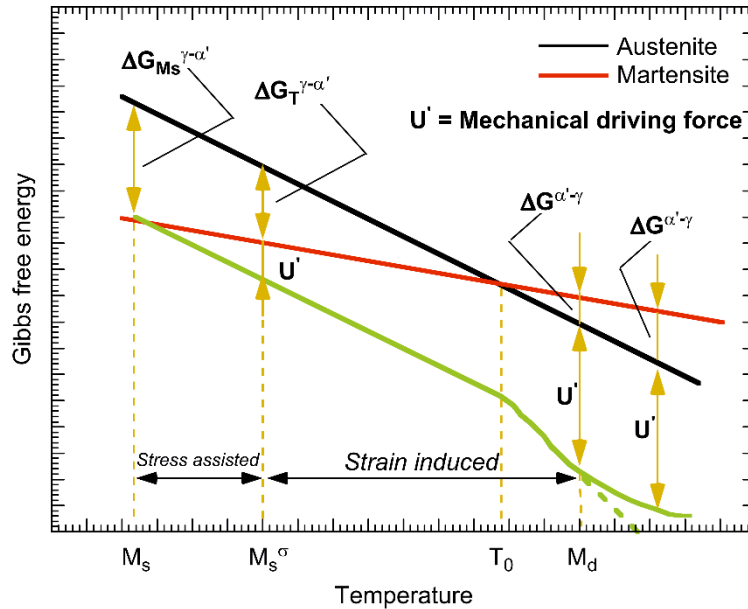


Fig. 1.3. Effect of temperature on the Gibbs free energy of both martensite and austenite phases [10,11].

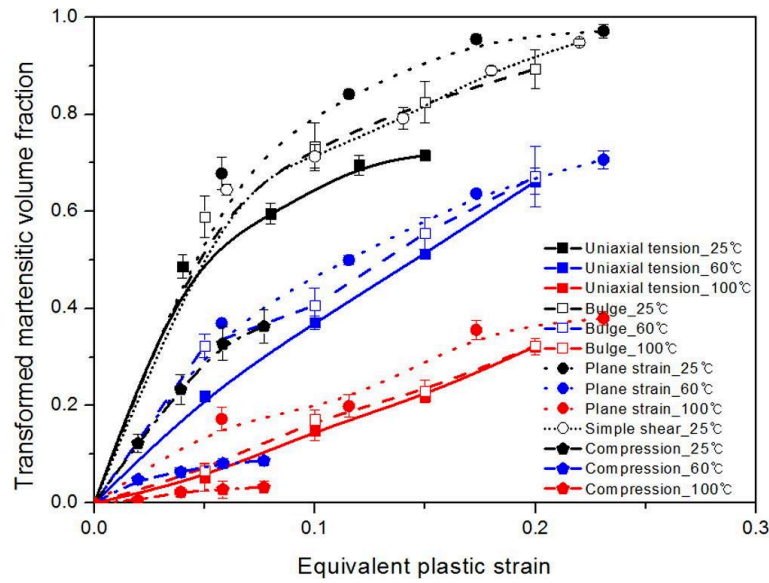


Fig. 1.4. Martensitic volume fraction as a function of equivalent plastic strain under various temperatures [9].

Strain rate is another parameter that affects SIMT. It is both beneficial and harmful to the martensitic transformation: on one hand, martensite nucleates at shear band intersections and the number of intersections increases with increasing strain rate. Hence, more martensite forms at high strain rates and small strains. On the other hand, at dynamic strain rates and large strains, the adiabatic heating effect becomes obvious and martensitic transformation is strongly inhibited.

Hecker et al. [12] and Murr et al. [13] performed tension tests at both low (10^{-3} s^{-1}) and high (10^3 s^{-1}) strain rates to study martensitic transformation behavior in 304 ASS. They found that martensite volume fraction at 10^3 s^{-1} is obviously lower than that at 10^{-3} s^{-1} at large strains, Fig. 1.5. A similar phenomenon was observed by several other authors in various types of ASS [7,14].

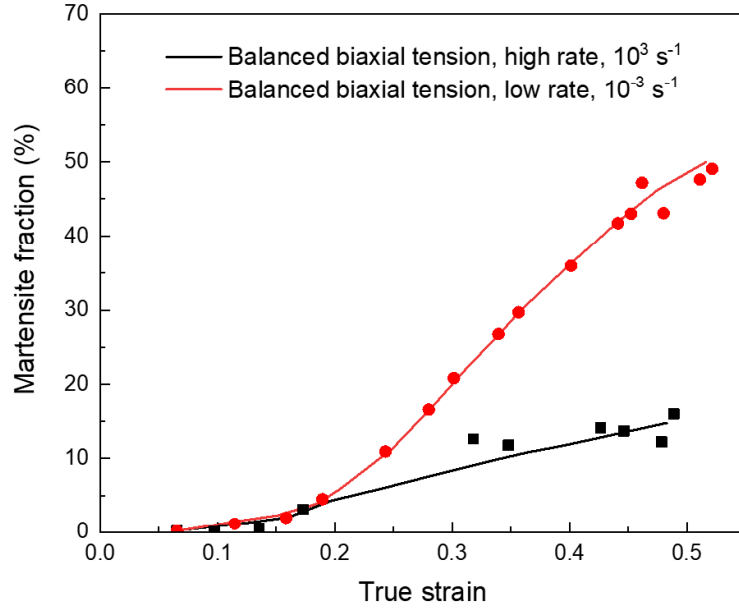


Fig. 1.5. Martensite fraction during tests at room temperature in balanced biaxial tension at high (10^3 s^{-1}) and low (10^{-3} s^{-1}) strain rates [12].

2.2 Deformation behavior of 304 ASS

Deformation mechanism of 304 ASS is a combination of martensitic transformation and dislocation slip or even twins [15]. But the contribution of each aspect varies significantly at different strain rates and temperatures. Therefore, the evolution of flow stress with strain rates and temperatures is different from the commonly used metallic alloys.

Concerning the effect of temperature on the deformation behavior of 304 ASS, it can be divided into two regions: $T < M_d$ and $T \geq M_d$. At temperatures below M_d , the stress-strain curves exhibit an S-shape and a second hardening phenomenon. This is caused by SIMT. With decreasing temperature, the flow stress increases continuously, and the nonlinearity phenomenon becomes more obvious. At temperatures above M_d , dislocation slip becomes the main deformation mechanism. According to thermally activated dislocation theory, the slip obstacles can be overcome by gliding dislocations more easily at higher temperatures due to the

assistance of thermal energy [3]. Therefore, with increasing temperature, the strength of 304 ASS decreases without the second hardening behavior.

Byun et al. [4] studied quasi-static tension behavior of 3 kinds of ASS including the type 304 at temperatures ranging from -150°C to 450°C . As shown in Fig. 1.6, both the yield stress and the ultimate tensile strength decrease with increasing temperature, and the best ductility peaked at 20°C . At temperatures below 20°C , the typical second hardening phenomenon accompanied by martensitic transformation was observed. Hamada et al. [1] investigated deformation behavior of 201 and 201L austenite stainless steel at temperatures ranging from -80°C to 200°C and obtained similar results: increasing flow stress with decreasing temperature. The maximum elongation value was obtained at 50°C , a temperature around which martensitic transformation was suppressed but intense mechanical twins formed.

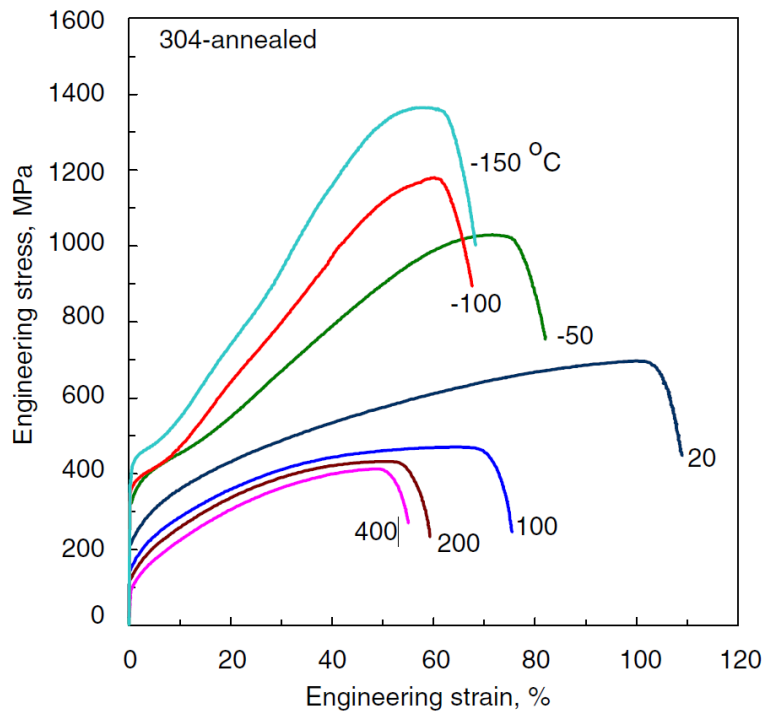


Fig. 1.6. Temperature dependence of engineering stress-strain curves for 304 stainless steel [3].

Zheng and Yu [17] studied the tensile behavior of 304 ASS between -253°C and

20°C and found both the flow stress and the strain hardening rate increased with decreasing temperature. In addition, because of the thermally induced martensitic transformation before tensile testing, the yield stress at -253°C and -196°C was significantly higher than the other temperatures.

Affected by SIMT, strain rate sensitivity of 304 stainless steel is also different from the commonly used steels whose deformation is dominated by dislocation slip.

At the initial stage of deformation, flow stress of 304 stainless steel increases with increasing strain rate as the time available for a dislocation to wait in front of an obstacle for the additional thermal energy is reduced. Also, the positive strain rate sensitivity at small strains was reported to be partly caused by higher martensite fraction at higher strain rates by Hecker et al. [12] and Murr et al. [13].

However, when it comes to large strains strengthening effect originated from martensitic transformation is inhabited by adiabatic heating at high strain rates and the corresponding strain hardening rate decreases. Combining strain rate's effect on both dislocation slip and martensitic transformation, either positive [14,18] or negative [19,20] strain rate sensitivity of 304 ASS was observed.

Lichtenfeld et al. [7] investigated the tension behavior of 304L stainless steel at room temperature. With the strain rates increasing from 10^{-4} s^{-1} to 400 s^{-1} , the flow stress declined first (from 10^{-4} s^{-1} to 10^{-2} s^{-1}) and then began to increase (from 10^{-1} s^{-1} to 400 s^{-1}). In addition, Ishikawa and Tanimura [21] found 304N stainless steel showed a positive strain rate sensitivity at room temperature but it changed into negative when tested at -83°C, Fig. 1.7.

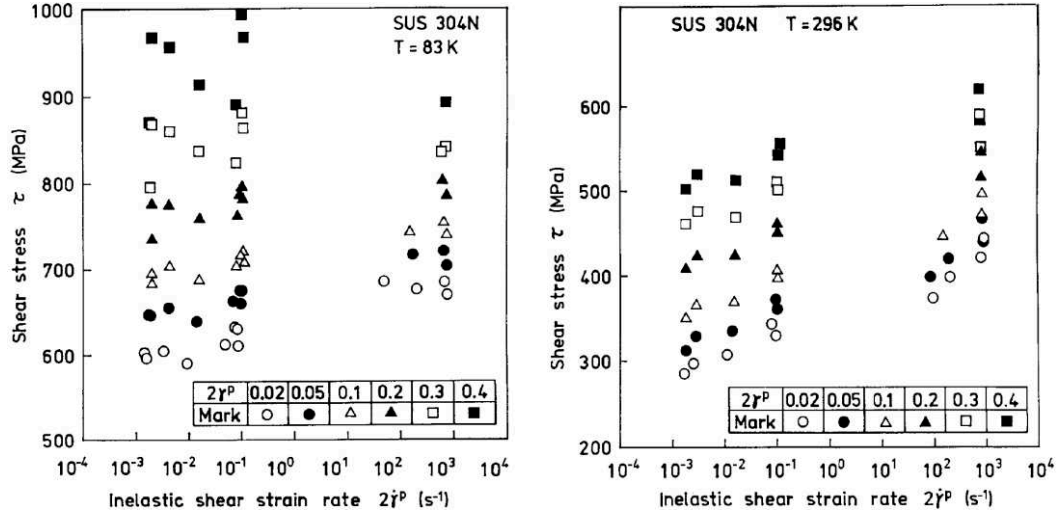


Fig. 1.7. The flow stress of 304N at constant strain vs strain rate at (a) 83 K and (b) 296 K [21].

3. Constitutive behavior and martensitic transformation modelling in 304 ASS

3.1 Constitutive behavior modelling of metallic alloys

The constitutive models are divided into two categories:

- Phenomenological models. They provide a description of flow stress based on empirical observations and are commonly made up of some mathematical functions [22]. They are simple and have a limited number of material parameters. However, they do not have any physical basis and are usually used in limited deformation conditions (for example limited range of strain rates and temperatures).

- Physical models. They are built according to physical theories such as thermally activated dislocation. Compared to phenomenological models, they can give an accurate deformation behavior description over a wide range of deformation conditions. But the models are usually complicated and a large number of tests are needed to define material constants.

Phenomenological models

Phenomenological models, including Johnson-Cook (JC) model [23], Khan-Huang (KH) model [24], Khan-Huang-Liang (KHL) model [25–27], and Arrhenius equation [28,29], are widely used in numerical simulations. The common feature of these models is that they can be expressed as functions of several deformation parameters' effects on the flow stress:

$$\sigma = \sigma(\varepsilon, \dot{\varepsilon}, T, \eta, \bar{\theta}) \quad \text{Eq. 1.2}$$

● Johnson-Cook (J-C) model

Johnson-Cook (J-C) model is commonly used for many kinds of materials over a wide range of strain rates and temperatures. It is expressed as:

$$\sigma = (A + B\varepsilon^n)(1 + C\ln\dot{\varepsilon}^*)(a - T^{*m}) \quad \text{Eq. 1.3}$$

where σ is the flow stress, ε is the equivalent plastic strain, A is the yield stress at reference strain rate and temperature, B is the strain hardening coefficient, n is the strain hardening exponent, $\dot{\varepsilon}^* = \frac{\dot{\varepsilon}}{\dot{\varepsilon}_{ref}}$ is the dimensionless strain rate and $T^* = \frac{(T-T_r)}{(T_m-T_r)}$ is the homologous temperature. T is the absolute temperature, T_m is the melting temperature and T_r is the reference temperature.

The three items in the equation describe the strain hardening effect, strain rate sensitivity and thermal softening effect, respectively. In addition, the three effects are assumed to be independent of each other.

J-C model is widely used because it is simple to implement and the parameters are easy to be obtained with a limited number of tests. However, it regards the mechanical properties of materials as a simple multiplication of strain, strain rate and temperature and ignores the coupling effects between them. Therefore, some researchers made modifications to the original J-C model and gave a more accurate

deformation behavior description [5-8].

● **Khan-Huang (K-H) model and Khan-Huang-Liang (K-H-L) model**

Khan-Huang (K-H) model was developed by Khan and Huang [9] in 1992 to model deformation behavior of Al 1100 alloys. It is given as:

$$\sigma = g_1(\varepsilon)g_2(\dot{\varepsilon}) \quad \text{Eq. 1.4}$$

$$g_1(\varepsilon) = \sigma_0 + E_\infty \varepsilon - ae^{-\alpha\varepsilon} \quad \text{Eq. 1.5}$$

$$g_1(\varepsilon)g_2(\dot{\varepsilon}) = \left[1 - \frac{\ln(\dot{\varepsilon})}{\ln(D_{max}^p)}\right]^n \quad \text{Eq. 1.6}$$

where $g_1(\varepsilon)$ characterizes the flow stress versus strain at reference strain rate, and $g_2(\dot{\varepsilon})$ describes the strain rate hardening effect. σ , ε , $\dot{\varepsilon}$ and D_{max}^p are the flow stress, the equivalent plastic strain, the strain rate and the maximum strain rate the material experienced during the testing process, respectively. n , E_∞ , σ_0 , a and α are material constants need to be determined.

It is obvious that K-H model does not take temperature's effect into consideration. In order to give a better prediction of strain hardening behavior of materials, Khan, Huang and Liang added the coupling thermal effect of strain and strain rate to the original K-H model and developed the Khan-Huang-Liang (K-H-L) model:

$$\sigma = \left[A + B \left(1 - \frac{\ln \dot{\varepsilon}}{\ln D_0^p}\right)^n \varepsilon^k\right] (1 - T^{*m}) \exp(c \ln \dot{\varepsilon}) \quad \text{Eq. 1.7}$$

where A , B , n , k , c , and m are material constants; $T^* = \frac{(T-T_r)}{(T_m-T_r)}$ is the homologous temperature (T is the testing temperature, T_m is the melting temperature and T_r is the reference temperature). It is obvious that the coupling

effect between strain and strain rate on strain hardening behavior of materials is included in the model.

For Ti-6Al-4V alloy, a comparison between experiments and the predicted results by J-C model and K-H-L model is shown in Fig. 1.8. The K-H-L model gives a slightly better agreement with experimental data than the J-C model.

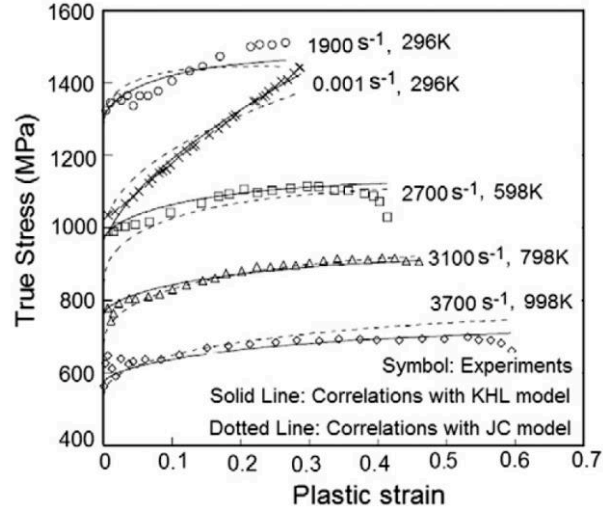


Fig. 1.8. True stress-true strain curves of Ti-6Al-4V alloy with correlations using J-C and K-H-L models [10].

● Arrhenius equation

Arrhenius equation is widely used to describe flow stress's dependence on strain rate at elevated temperatures [11]. The effects of strain rate and temperature on the deformation behavior of materials can be described by the Zener-Hollomon parameter in an exponent-type equation [12,13].

$$\dot{\epsilon} = AF(\sigma)\exp\left(-\frac{Q}{RT}\right) \quad \text{Eq. 1.8}$$

$$Z = \dot{\epsilon}\exp\left(\frac{QR}{T}\right) \quad \text{Eq. 1.9}$$

$$F(\sigma) = [\sinh(\alpha\sigma)]^n \quad \text{Eq. 1.10}$$

where $\dot{\varepsilon}$ is the strain rate, R is the universal gas constant, T is the absolute temperature, Q is the activation energy for deformation behavior, σ is the flow stress, A , α and n are material constants.

According to the three equations above, the flow stress can be written as,

$$\sigma = \frac{1}{\alpha} \ln \left[\left(\frac{Z}{A} \right)^{\frac{1}{n}} + \sqrt{\left(\frac{Z}{A} \right)^{\frac{2}{n}} + 1} \right] \quad \text{Eq. 1.11}$$

It is clear that the effect of strain on the deformation behavior of materials is not included in the Arrhenius equation. Therefore, Lin et al. [14] modified the model by considering strain rate and strain, then used it to describe flow stress of 42CrMo steel over a wide range of strain rates and temperatures. They expressed Q , n , A and α as polynomial functions of strain:

$$Q = B_0 + B_1 \varepsilon + B_2 \varepsilon^2 + B_3 \varepsilon^3 + B_4 \varepsilon^4 + B_5 \varepsilon^5 \quad \text{Eq. 1.12}$$

$$n = C_0 + C_1 \varepsilon + C_2 \varepsilon^2 + C_3 \varepsilon^3 + C_4 \varepsilon^4 + C_5 \varepsilon^5 \quad \text{Eq. 1.13}$$

$$A = \exp (D_0 + D_1 \varepsilon + D_2 \varepsilon^2 + D_3 \varepsilon^3 + D_4 \varepsilon^4 + D_5 \varepsilon^5) \quad \text{Eq. 1.14}$$

$$\alpha = E_0 + E_1 \varepsilon + E_2 \varepsilon^2 + E_3 \varepsilon^3 + E_4 \varepsilon^4 + E_5 \varepsilon^5 \quad \text{Eq. 1.15}$$

Two comparisons between experiments and modeling results are shown in Fig. 1.9. It is clear that experiments and simulations are highly consistent with each other.

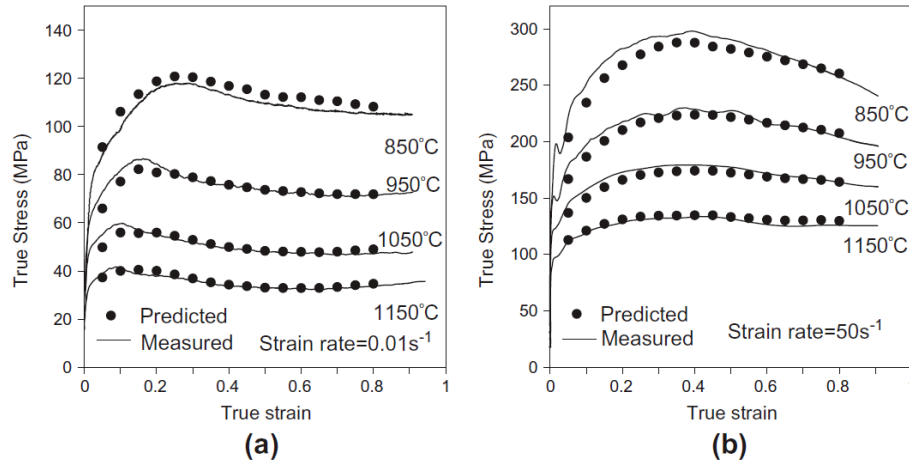


Fig. 1.9. Comparisons between experiments and modelling results of 42CrMo steel at strain rates (a) 0.01 s^{-1} and (b) 50 s^{-1} [14].

Physical models

An obvious drawback of phenomenological models is that they are obtained by fitting experimental data and do not include any deformation mechanism. They may work well under common conditions, but when it comes to the extreme conditions (such as extreme high strain rates and temperatures), they are not able to give an accurate description anymore. Therefore, physical models based on deformation mechanisms such as dislocation dynamics and thermal activation seem to be more reliable. Until now, many physical models such as Zerilli-Armstrong (Z-A) model [36], Bonder-Partom (B-P) model [37] and Rusinek-Klepaczko (R-K) model [38] have been developed.

● Zerilli-Armstrong (Z-A) model

Zerilli-Armstrong (Z-A) model is developed based on dislocation mechanism and often gives a good description of deformation behavior under different loading conditions. It considers the effects of strain hardening, strain rate hardening and thermal softening on deformation behavior of materials, and is made up of two parts, thermal component and athermal component,

$$\sigma = \sigma_{\alpha} + \sigma_{th} \quad \text{Eq. 1.16}$$

where σ_{α} is the athermal flow stress, σ_{th} is the thermal flow stress.

$$\sigma_{th} = \frac{M\Delta G_0 e^{-\beta T}}{Ab} \quad \text{Eq. 1.17}$$

$$\beta = -C_3 + C_4 \ln \dot{\epsilon} \quad \text{Eq. 1.18}$$

where M is the direction factor, ΔG_0 is the free energy of thermal activation at 0 K, b is the burger vector, β is a parameter related to strain and strain rate.

For BCC metal, A is a material constant. But for FCC metal, A is regarded as $\sqrt{\epsilon}$. Therefore, the thermal flow stresses for BCC and FCC metal are written separately as

$$\sigma_{th} = C_1 \exp(-C_3 T + C_4 T \ln \dot{\epsilon}) \quad \text{Eq. 1.19}$$

$$\sigma_{th} = C_2 \epsilon^{\frac{1}{2}} \exp(-C_3 T + C_4 T \ln \dot{\epsilon}) \quad \text{Eq. 1.20}$$

Combining the athermal and thermal parts, the equations for FCC and BCC metals are

$$\sigma = C_0 + C_1 \exp(-C_3 T + C_4 T \ln \dot{\epsilon}) + C_5 \epsilon^n \quad \text{Eq. 1.21}$$

$$\sigma = C_0 + C_2 \epsilon^{\frac{1}{2}} \exp(-C_3 T + C_4 T \ln \dot{\epsilon}) \quad \text{Eq. 1.22}$$

where C_0 , C_1 , C_2 , C_3 , C_4 , C_5 and n are material constants.

It can be seen from the two equations that the strain hardening rate of BCC materials is not affected by strain rate or temperature; while for FCC materials, the strain hardening rate is strongly affected by the two parameters. In fact, the coupling effects between strain, strain rate and temperature should be considered in a more effective constitutive way. Therefore, some researchers made several modifications to the Z-A model [15-19].

● Bodner-Parton (B-P) model

In 1975, Bodner and Parton [20] proposed a model to describe the deformation behavior of materials under large deformation and arbitrary loading histories. The model divides the total deformation into elastic and plastic components, which are functions of strain state variables at all deformation stages. The model is given as

$$\varepsilon^p = \frac{2\sigma}{\sqrt{3}|\sigma|} D_0 \exp \left[- \left(\frac{n+1}{2n} \right) \left(\frac{Z}{\sigma} \right)^{2n} \right] \quad \text{Eq. 1.23}$$

$$Z = Z_1 + (Z_0 - Z_1) \exp \left(- \frac{m \int \sigma d\varepsilon^p}{Z_0} \right) \quad \text{Eq. 1.24}$$

where Z_0 , Z_1 , m and n are material constants needed to be determined. D_0 is the maximum strain rate during tests.

● Rusinek-Klepaczko (R-K) model

Inspired by thermally activated dislocation motion theory [21], the RK model is given as a sum of two components, the internal stress $\sigma_\mu(\bar{\varepsilon}^p, \dot{\varepsilon}^p, T)$ and the effective stress $\sigma^*(\dot{\varepsilon}^p, T)$, defining the strain hardening effect and the thermal activation process, respectively.

$$\bar{\sigma}(\bar{\varepsilon}^p, \dot{\varepsilon}^p, T) = \frac{E(T)}{E_0} [\sigma_\mu(\bar{\varepsilon}^p, \dot{\varepsilon}^p, T) + \sigma^*(\dot{\varepsilon}^p, T)] \quad \text{Eq. 1.25}$$

The two components are multiplied by a parameter $E(T)/E_0$ to represent the temperature dependent Young's modulus,

$$E(T) = E_0 \left\{ 1 - \frac{T}{T_m} \exp \left[\theta^* \left(1 - \frac{T_m}{T} \right) \right] \right\} \quad \text{Eq. 1.26}$$

where E_0 , T_m , θ^* are Young's modulus at 0 K, the melting temperature and the characteristic homologous temperature of the tested material, respectively.

A strain hardening equation similar to the Swift law is used to describe the internal stress $\sigma_\mu(\bar{\epsilon}^p, \dot{\epsilon}^p, T)$. The plasticity modulus $B(\dot{\epsilon}^p, T)$ and the strain hardening parameter $n(\dot{\epsilon}^p, T)$ are both strain rate and temperature dependent,

$$\sigma_\mu(\bar{\epsilon}^p, \dot{\epsilon}^p, T) = B(\dot{\epsilon}^p, T)(\epsilon_0 + \bar{\epsilon}^p)^{n(\dot{\epsilon}^p, T)} \quad \text{Eq. 1.27}$$

$$B(\dot{\epsilon}^p, T) = B_0 \left[\left(\frac{T}{T_m} \right) \log \left(\frac{\dot{\epsilon}_{max}}{\dot{\epsilon}^p} \right) \right]^{-v} \quad \text{Eq. 1.28}$$

$$n(\dot{\epsilon}^p, T) = n_0 \left\langle 1 - D_2 \left(\frac{T}{T_m} \right) \log \left(\frac{\dot{\epsilon}^p}{\dot{\epsilon}_{min}} \right) \right\rangle \quad \text{Eq. 1.29}$$

where ϵ_0 refers to the value corresponding to the yield point during quasi-static tests; $\dot{\epsilon}_{max}$ and $\dot{\epsilon}_{min}$ are the maximum and minimum strain rate experienced by the tested material, respectively; B_0 and D_2 are material constants; v is the temperature sensitivity parameter and n_0 is the strain hardening parameter at 0 K. The operator $\langle x \rangle = x$ if $x > 0$ otherwise $\langle x \rangle = 0$ if $x \leq 0$.

The effective stress $\sigma^*(\dot{\epsilon}^p, T)$ defines the flow stress induced by thermal activation process using an Arrhenius equation:

$$\sigma^*(\dot{\epsilon}^p, T) = \sigma_0^* \left\langle 1 - D_1 \left(\frac{T}{T_m} \right) \log \left(\frac{\dot{\epsilon}_{max}}{\dot{\epsilon}^p} \right) \right\rangle^{m^*} \quad \text{Eq. 1.30}$$

where σ_0^* is the effective stress at 0 K, D_1 and m^* are material constants.

In order to describe the thermo-viscoplastic behavior of aluminium alloy more accurately, Rusinek et al. [22] developed two extensions of the R-K model. They define the negative strain rate sensitivity and the viscous drag phenomenon of aluminium alloys respectively.

The first extension is expressed as

$$\bar{\sigma}(\bar{\epsilon}^P, \dot{\bar{\epsilon}}^P, T) = \frac{E(T)}{E_0} [\sigma_\mu + \sigma^* + \sigma_{ns}(\dot{\bar{\epsilon}}^P, T)] \quad \text{Eq. 1.31}$$

where $\sigma_{ns}(\dot{\bar{\epsilon}}^P, T)$ is the term defining the negative strain rate sensitivity. It is related to strain rate and temperature and is expressed as

$$\sigma_{ns}(\dot{\bar{\epsilon}}^P, T) = \sigma_0^{ns} \log\left(\frac{\dot{\epsilon}_{trans}}{\dot{\bar{\epsilon}}^P}\right) \left(1 - D_3 \left(\frac{T}{T_m}\right) \log\left(\frac{\dot{\bar{\epsilon}}^P}{\dot{\epsilon}_{max}}\right)\right) \quad \text{Eq. 1.32}$$

where σ_0^{ns} defines the stress decrease due to dynamic strain aging, D_3 is the material constant describing the reciprocity between strain-rate and temperature and $\dot{\epsilon}_{trans}$ is the transition strain rate between positive and negative strain rate sensitivity.

The second extension of the R-K model is developed to describe viscous drag effect in FCC metal during high strain rate deformation. It is given as

$$\bar{\sigma}(\bar{\epsilon}^P, \dot{\bar{\epsilon}}^P, T) = \frac{E(T)}{E_0} [\sigma_\mu + \sigma^* + \sigma_{ath}(\dot{\bar{\epsilon}}^P)] \quad \text{Eq. 1.33}$$

where $\sigma_{ath}(\dot{\bar{\epsilon}}^P)$ is the term accounting for the viscous drag effect. It depends on strain rate,

$$\sigma_{ath} = \sigma_{ath} \left(\left(\frac{M^2 B}{\rho_m b^2} \right), \dot{\bar{\epsilon}}^P \right) \propto \dot{\bar{\epsilon}}^P \quad \text{Eq. 1.34}$$

$$\sigma_{ath}(\dot{\bar{\epsilon}}^P) = \chi [1 - \exp(-\alpha \dot{\bar{\epsilon}}^P)] \propto \dot{\bar{\epsilon}}^P \quad \text{Eq. 1.35}$$

$$\alpha = \frac{M^2 B}{\rho_m b^2 \tau_y} \quad \text{Eq. 1.36}$$

where M , B , ρ_m and b are the Taylor factor, the drag coefficient, the mobile dislocation density and the magnitude of the burger vector, respectively. χ , α and τ_y are the material constant, an effective damping coefficient and the high temperature yield stress, respectively.

The comparison between experiments, the original R-K model and the extended R-K model at two high strain rates is shown in Fig. 1.10. It is obvious that the viscous-drag term in the extended R-K model can compensate the underestimation of flow stress obtained by Arrhenius equation and correct deformation behavior of materials at high strain rates, especially at elevated temperatures.

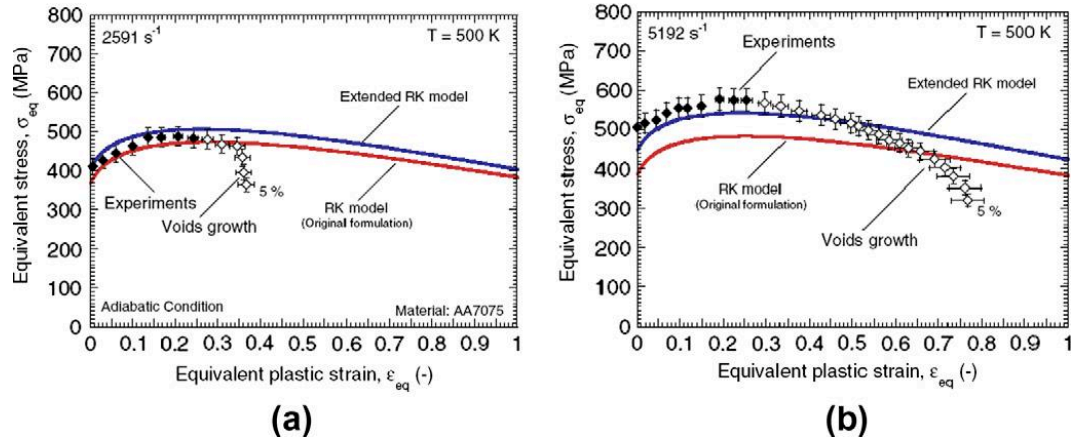


Fig. 1.10. Comparison between experiments, the original R-K model and the extended R-K model at different strain rates: (a) 2591 s^{-1} ; (b) 5192 s^{-1} [22].

3.2 Constitutive modelling of martensitic transformation

Mechanical properties of 304 ASS, such as strength, ductility and strain hardening rate, are all affected by SIMT. Therefore, lots of work focuses on the modelling of martensitic transformation kinetics under strain rate, temperature and other deformation parameters. The three classical models that are most widely used are Olson-Cohen (O-C) model [46], Stringfellow (S) model [47] and Tomita-Iwanamoto (T-I) model [48]. All the three models are developed based on shear band theory: shear band intersections are the dominant nucleation sites for martensitic transformation [46]. With the increase of plastic strain, both the volume fraction of shear bands and the number of shear band intersections increase. Therefore, the Gibbs free energy between austenite and martensite increases. As a result,

martensitic transformation takes place with the help of the mechanical driving force.

● Olson-Cohen (O-C) model

In 1975, Olson and Cohen [23] proposed a model to describe martensitic transformation nucleation. They assumed the volume fraction of shear bands is a function of the untransformed austenite,

$$\dot{f}_{sb} = \alpha(1 - f_{sb})\dot{\epsilon} \quad \text{Eq. 1.37}$$

where f_{sb} is the volume fraction of shear bands, α is a material constant depends on stacking fault energy and strain rate.

The number of shear band intersections is related to the number of shear bands by a simple equation

$$N_v^I = K(N_v^{sb})^n \quad \text{Eq. 1.38}$$

where N_v^I is the number of intersections, N_v^{sb} is the number of shear bands, K and n are material constants.

The incremental increase of martensite embryos, dN_v^α , is related to the increase of shear band intersections by

$$dN_v^\alpha = p dN_v^I \quad \text{Eq. 1.39}$$

where p is the probability that a shear band intersection forms a martensite embryo.

They assume further that the unit volume of martensite is a constant, being restricted to the region of shear band intersection. Therefore, the total volume fraction of martensite depends on the number of embryos and is related to plastic strain by

$$f^{\alpha'} = 1 - \exp\{-\beta[1 - \exp(-\alpha\epsilon)]^n\} \quad \text{Eq. 1.40}$$

where $\beta = \left(\frac{\bar{v}^{\alpha'}}{\bar{v}^{sb}}\right)^n Kp$, $\bar{v}^{\alpha'}$ is the volume of a α' unit and \bar{v}^{sb} is the volume of a shear band.

● Stringfellow (S) model

In 1992, Stringfellow [24] modified the O-C model and included the effects of temperature and stress state in the model. The incremental increase of martensite volume fraction, \dot{f}_m is proportional to the rate of martensite embryos per unit volume \dot{N}_m ,

$$\dot{f}_m = (1 - f_m)\bar{v}_m\dot{N}_m \quad \text{Eq. 1.41}$$

where \bar{v}_m is the average unit volume of martensite and is defined as a constant.

\dot{N}_m is given by the rate of product $N_{sb}^I P$

$$\dot{N}_m = P\dot{N}_{sb}^I + N_{sb}^I \dot{P}U(\dot{P}) \quad \text{Eq. 1.42}$$

where N_{sb}^I is the number of shear band intersections per unit volume and P is the probability that a shear band intersection acts as a nucleation site. $U(\dot{P})$ is the Heaviside unit step function and is used to represent the irreversible martensitic transformation. P is calculated by Gaussian cumulative probability distribution function,

$$P(g) = \frac{1}{\sqrt{2\pi}s_g} \int_{-\infty}^g \exp\left[-\frac{1}{2}\left(\frac{\tilde{g} - \bar{g}}{s_g}\right)^2\right] d\tilde{g} \quad \text{Eq. 1.43}$$

where \tilde{g} and s_g are the mean and standard deviation of the normal distribution function, respectively. In addition, g is a normalized thermodynamic driving force for martensitic transformation, it is related to temperature and stress triaxiality by the equation

$$g = g_0 - g_1\theta + g_2\Sigma \quad \text{Eq. 1.44}$$

where g_0 , g_1 and g_2 are dimensionless material constants. θ is a normalized temperature related to the absolute temperature θ by the following equation

$$\theta = \frac{\theta - M_S^\sigma}{M_d - M_S^\sigma} \quad \text{Eq. 1.45}$$

where M_d is the upper temperature limit for martensitic transformation and M_S^σ the limit temperature for strain induced martensitic nucleation. Σ is the stress triaxiality defined as the ratio between hydrostatic stress and Mises equivalent stress.

The rate of P , under isothermal condition, is thus given by

$$\dot{P} = \frac{g_2}{\sqrt{2\pi}s_g} \exp \left[-\frac{1}{2} \left(\frac{g - \bar{g}}{s_g} \right)^2 \right] \dot{\Sigma} \quad \text{Eq. 1.46}$$

Then an evolution equation for the volume fraction of martensite

$$\dot{f}_m = (1 - f_m)(A_f \dot{\epsilon}_a^P + B_f \dot{\Sigma}) \quad \text{Eq. 1.47}$$

where the factor associated with plastic deformation in austenite is given by

$$B_f = \beta_0 (f_{sb})^n \frac{g_2}{\sqrt{2\pi}s_g} \exp \left[-\frac{1}{2} \left(\frac{g - \bar{g}}{s_g} \right)^2 \right] U(\dot{P}) \quad \text{Eq. 1.48}$$

● Tomita-Iwanamoto (T-I) model

O-C model considers only temperature and plastic strain' effects on martensitic transformation; while for the S model, it includes the effects of temperature and stress state into the model. Based on O-C model and S model, Tomita and Iwanamoto [25] studied effect of strain rate on martensitic transformation and developed T-I model. The volume fraction increase of martensite \dot{f}_m is expressed as:

$$\dot{f}_m = (1 - f_m) A P \dot{\epsilon}_a^{Pslip} \quad \text{Eq. 1.49}$$

$$A = \alpha \eta n (1 - f_{sb}) (f_{sb})^{n-1} \quad \text{Eq. 1.50}$$

where $\dot{\epsilon}_a^{Pslip}$ is the deformation strain rate of the austenite phase, f_{sb} is the volume fraction of shear band, P is used to describe transformation probability, η and n are geometric parameters.

According to experimental observation, the strain rate will influence shear band intersection, and the number of shear band intersection increases with the increase of strain rate. So α is expressed as:

$$\alpha = \alpha_0 \left(\frac{\dot{\epsilon}_a^{Pslip}}{\dot{\epsilon}_y} \right)^M \quad \text{Eq. 1.51}$$

$$\alpha_0 = \alpha_1 T^2 + \alpha_2 T + \alpha_3 \quad \text{Eq. 1.52}$$

where M is the strain rate sensitivity coefficient, $\dot{\epsilon}_y$ is the reference strain rate, α_0 is related to the test temperature and T is the ambient temperature.

4. Dynamic shear testing techniques of metallic alloys

Dynamic shear deformation and failure are present in many engineering areas such as metal forming and machining, car crashworthiness and ballistic impact. Therefore, over the last decades, mechanical properties of materials have been investigated intensively by shear testing.

As a complement to the ordinary mechanical testing methods such as uniaxial tension and compression, shear testing has several advantages. First, without necking instability phenomenon in tension or barreling effect in compression, deformation mode in shear testing remains unchanged until large strains. Therefore, the stress-strain relationship of materials can be extracted from the macro obtained force-displacement curves accurately [38,49].

Second, unlike tension or compression specimens, dimensions of shear

specimens, especially the shear zone, can be designed to be so small that a pretty high strain rate in the order of 10^4 s^{-1} or even 10^5 s^{-1} can be reached experimentally [50–52].

In addition, stress state, represented by stress triaxiality η and Lode angle parameter μ , has been shown to influence deformation and failure behavior of materials significantly [53–55]. By changing stress state inside shear dominated specimens, the effects of the two parameters on deformation and failure mechanisms of materials can be investigated thoroughly [56–58].

4.1 Dynamic shear specimens

Various specimen geometries have been developed for measuring shear properties of materials under dynamic loading. Among them, the most commonly used methods include torsion test [59], hat shape test [60] and double shear test [61].

● Torsion specimen

Dynamic torsion test, as shown in Fig. 1.11, by a modified Split Hopkinson Bar (SHB) was first introduced by Duffy and Campbell [59] to study strain rate sensitivity of aluminium alloys. The torque was applied on the specimen through a flying wheel and by this way a maximum strain rate of 800 s^{-1} can be obtained. During torsion tests, the specimen gauge geometry remains unchanged, shear stress-shear strain curves can be measured directly. However, restricted by the maximum torque that can be stored in the incident bar, the maximum strain rate during torsion testing is limited, even for specimens with small shear zones [38].

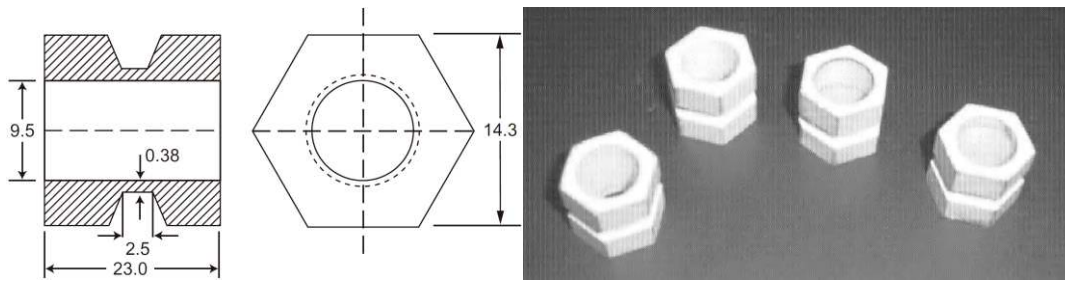


Fig. 1.11. Torsion specimen according to Duffy and Chi [62].

● Hat shape specimen

Another attractive shear specimen design is called hat shape specimen, originally invented by Meyer et al. [60] in 1986. It is an axisymmetric specimen made of an upper hat part and a lower brim part. When a compressive force is applied on its surface, the shear zone between the two parts is deformed. Mostly, the diameter of the hat part is larger than the brim part and by modifying the relative diameters of the two parts, a shear-compression stress state in the shear zone is generated.

Hat shape specimens are commonly used to study shear band formation in metallic materials [63–65]. By loading the specimens on a conventional Split Hopkinson Pressure Bar (SHPB) and making use of a stop ring [65], Fig. 1.12, the evolution of shear localization over a wide range of strain rates and temperatures can be studied. Additionally, the width of the shear zone in hat shape specimens can be designed to be very small, less than 1 mm. Therefore, very high strains and strain rates can be achieved.

Although hat shape specimens are widely used for shear band characterization, stress and strain distribution inside the shear zone is proved to be inhomogeneous and the measured shear stress-shear strain curves are not reliable. Hence, hat shape specimens should be used with great care when quantitative stress-strain data of materials is wanted.

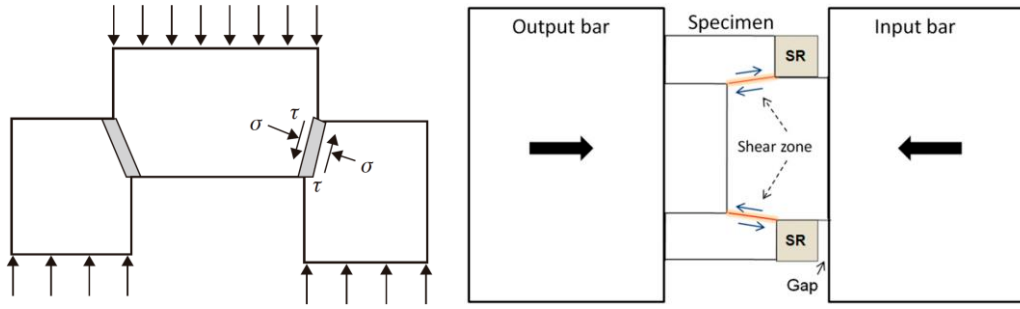


Fig. 1.12. Hat-shaped specimen according to Xue [66] and (b) the stop ring (SR) technique used by Peirs [65].

● Double shear specimen

Double shear specimen, as shown in Fig. 1.13, was initially utilized by Campbell and Ferguson [61] to study strain rate and temperature sensitivity of mild steel. The central portion of the specimens is in contact with the input bar while the two edge supports are fixed on an output tube. With the relative displacement between the central portion and two edge supports, the area between the two parts goes through shearing.

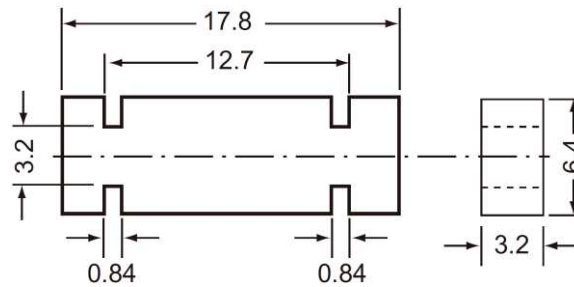


Fig. 1.13. Dimensions of the double-shear specimen according to Campbell and Ferguson [61].

During testing by double shear specimens, the edge supports of specimens rotate significantly. As a result, strain uniformity in shear zones is found to be quite low and the corresponding stress state also deviates obviously from pure shear. In order to solve this problem, much work has been done concerning specimen geometry optimization [49,51,52,67–70]. Among them, Shi and Merle [67] designed

a modified double shear specimen and a clamping device to constrain lateral movement of the specimen, Fig. 1.14. Therefore, a much more uniform stress state in shear zones is obtained.

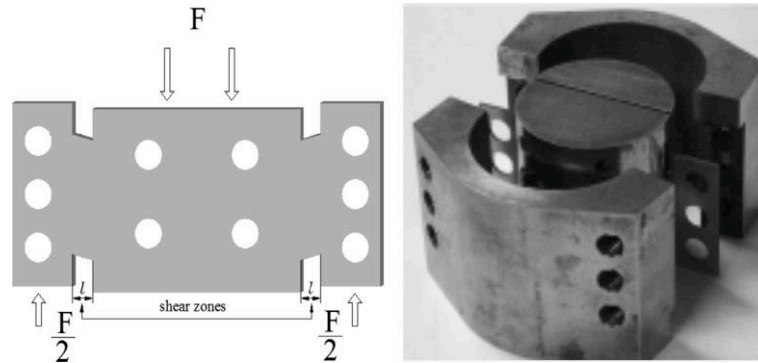


Fig. 1.14. Modified double-shear specimen and the clamping system according to Shi and Merle [67].

Double shear specimens can be utilized for shear behavior characterization, and the visible shear zone makes in situ strain and temperature observation possible. A drawback of the specimen is that failure initiation is caused by stress concentration at gauge corners instead of the material itself [71].

4.2 Dynamic shear testing devices

Besides the wide variety of specimen geometries, the techniques used for dynamic shear testing also vary a lot. Split Hopkinson Bar system may be the most popular method for dynamic shear characterization. For example, the hat shape specimen was used in many studies [60,63–65] to investigate shear band formation using the conventional Split Hopkinson Pressure Bar (SHPB). By modifying the width of specimen shear zones, strain rates with an order of 10^4 s^{-1} can be achieved.

● The conventional SHPB system

A schematic view of the SHPB system is shown in Fig. 1.15. Basically, it consists of a projectile, incident and transmitter bars and the shear specimen

sandwiched between them. When the projectile, usually launched by a gas gun, impacts the incident bar, an elastic compressive wave is generated and propagates along the incident bar. Upon reaching the incident bar/specimen interface, part of the wave is reflected back while the rest is transmitted to the specimen. After a few reflections between the two end faces of the shear specimen, stress uniformity inside the shear zone is achieved. According to Davies and Hunter [26] that at least three reverberations along the specimen were needed to achieve force equilibrium. After that, the wave propagates forward into the transmitter bar and is finally absorbed by a buffer. Two strain gauges are mounted on the incident bar and transmitter bars to measure the time dependent incident, reflected and transmitted waves ($\epsilon_I(t)$, $\epsilon_R(t)$ and $\epsilon_T(t)$, respectively). The typical wave signals from an SHPB test are shown in Fig. 1.16.

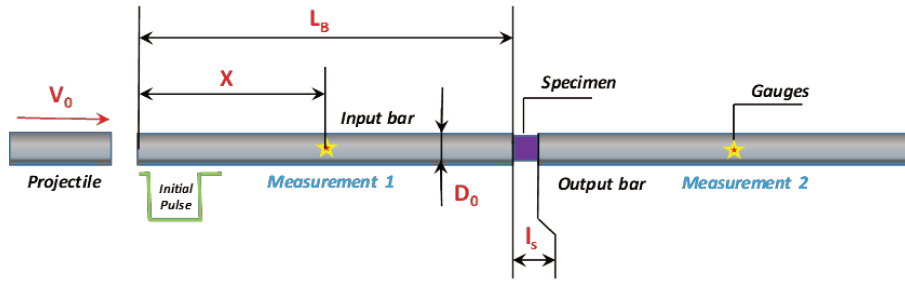


Fig. 1.15. Schematic diagram of the conventional SHPB system.

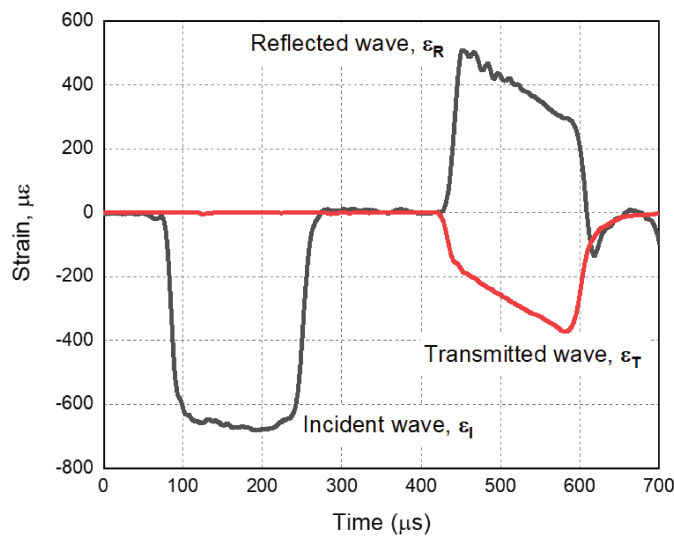


Fig. 1.16. The typical wave signals using the conventional SHPB system.

In order to obtain an accurate measurement of the deformation behavior of materials using the SHPB system, force equilibrium within the specimen is necessary. To evaluate the force equilibrium on the two end faces of the specimen, Ravichandran and Subhash [27] invented a parameter, $R(t)$, as below:

$$R(t) = \left| \frac{\Delta F(t)}{F_{avg}(t)} \right| = 2 \left| \frac{F_1(t) - F_2(t)}{F_1(t) + F_2(t)} \right| \quad \text{Eq. 1.53}$$

where $F_1(t)$ and $F_2(t)$ are the two forces acting on the end faces of the specimen, respectively. They can be calculated as $F_1(t) = EA(\varepsilon_l(t) + \varepsilon_R(t))$ and $F_2(t) = EA\varepsilon_T(t)$, and E and A are Young's modulus and the cross-sectional area of the bars, respectively. $\Delta F(t)$ and $F_{avg}(t)$ are the difference and the average of the two forces, respectively. Force equilibrium is achieved when $R(t)$ is very close to 0.

Having achieved dynamic force equilibrium within the specimen and based on the theory of one-dimensional wave propagation [28], the nominal shear stress $\sigma_{nominal}(t)$, nominal shear strain rate $\dot{\varepsilon}_{nominal}(t)$ and nominal strain $\varepsilon_{nominal}(t)$ of the specimen can be calculated as follows:

$$\sigma_{nominal}(t) = \frac{EA\varepsilon_T(t)}{A_s} \quad \text{Eq. 1.54}$$

$$\dot{\varepsilon}_{nominal}(t) = \frac{2C\varepsilon_R(t)}{L_s} \quad \text{Eq. 1.55}$$

$$\varepsilon_{nominal}(t) = \frac{2C}{L_s} \int_0^t \varepsilon_R(t) dt \quad \text{Eq. 1.56}$$

where C ($= \sqrt{E/\rho}$, ρ is the density of the SHPB bars) is the longitudinal wave speed of the bars. A_s and L_s are the cross-sectional area and the length of the specimen shear zone, respectively.

● Other dynamic shear testing methods

Because of the unique dimensions of the shear specimens, mostly they cannot be tested directly on the conventional SHPB system. Therefore, variants of the traditional SHPB system were invented by several researchers to conduct dynamic shear tests using various kinds of shear specimens.

Split Hopkinson Tension Bars (SHTB) was adopted by Dorogoy et al. [57] to study large strain deformation behavior of materials using the specially designed STS specimens. To fix the specimen, screws were machined in both the SHTB bars and the STS specimens. Duffy et al. [59,75] studied adiabatic shear band phenomenon in several alloys using a modified Split Hopkinson Torsion Bar and torsion specimens, Fig. 1.17.

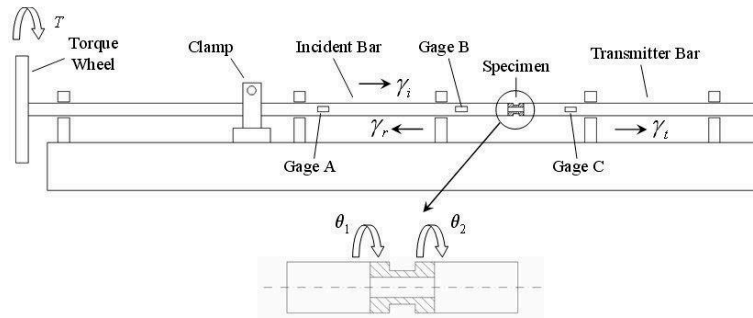


Fig. 1.17. Sketch of a torsion split Hopkinson bar apparatus [76].

In addition to Split Hopkinson Bar system and its variants introduced above, a fast hydraulic machine was utilized by Rusinek and Klepaczko [38] to determine shear stress-shear strain relations of sheet steel under intermediate strain rates between 1 s^{-1} and 10^2 s^{-1} . Drop weight tower [77,78] is another set-up for dynamic testing. Compared to the two methods above mentioned, drop weight tower can provide a larger amount of kinetic energy and therefore is suitable for high strength materials testing. Specially, Klepaczko [52] developed a direct impact technique for tests at extreme high strain rates. Different from the conventional SHPB system, the shear specimen here is impacted by a projectile directly. The projectile velocity varies from 10 m/s to 200 m/s , corresponding to a nominal strain rate between 10^2 s^{-1} and 10^5 s^{-1} .

5. Perforation behavior of metallic alloys

During the working and manufacturing process, materials may be subjected to impact loading over a wide range of strain rates and temperatures, Fig. 1.18. Therefore, a considerable amount of work has been done over the last decades to study the impact behavior of materials [29,30].

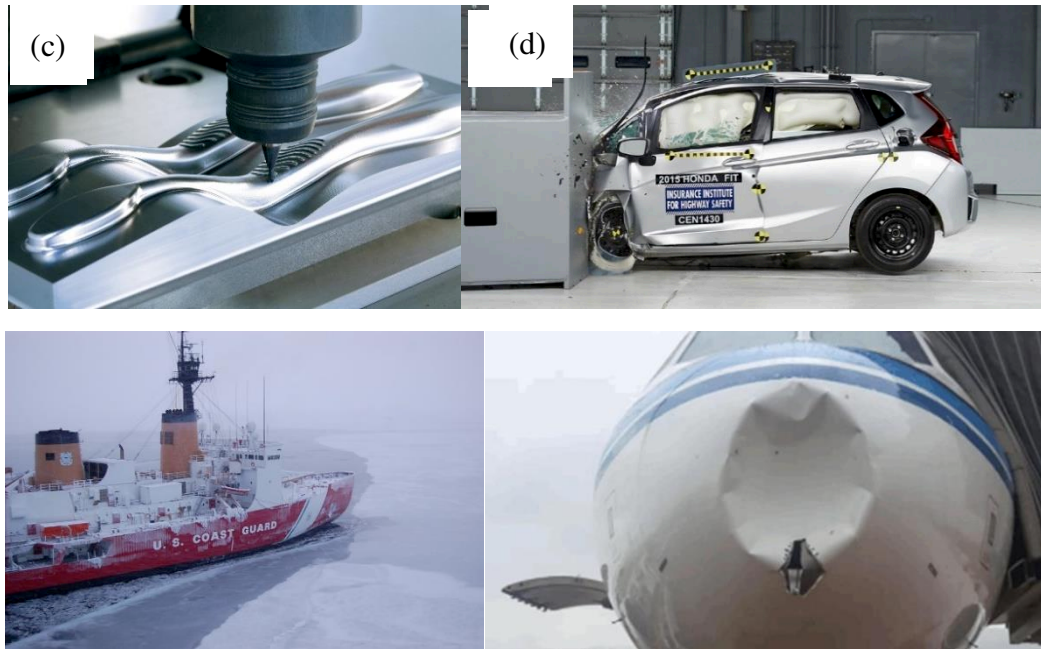


Fig. 1.18. Engineering applications where metallic alloys may be subjected to impact loading over various strain rates and temperatures. (a) high speed machining, (b) automotive industry, (c) naval industry and (d) aviation industry.

According to the impact velocity, investigation on the impact behavior of materials can be divided into 3 categories. The first category refers to low velocity impact (<50 m/s), where thin plates are commonly perforated by a drop weight tower [31]. The second covers sub-ordnance and ordnance velocity range between 50 and 1300 m/s, where projectiles are usually accelerated by a compressed air gas gun to perforate or penetrate plates [30]. The last category refers to hypervelocity impact (>1300 m/s), a velocity range often encountered in outer space impact such as debris hitting spacecraft [32].

The second velocity regime, sub-ordnance and ordnance velocity, aims at investigating the dynamic impact behavior of shell structures in many engineering areas and therefore has received the most attention. Mostly, sub-ordnance impact tests were performed with thin plates and non-deformable projectiles at room temperature to study its ballistic resistance performance, energy absorption capacity and failure mode. Those studies mainly focus on the effects of target thickness [33], impact obliquity [34], multilayer plates combination [35] and projectile nose shape [36-38] on perforation behavior of materials.

5.1 Effect of several parameters on perforation behavior of thin plates

The first parameter affecting perforation behavior of thin plates is the target thickness. Børvik et al. [33] investigated the perforation and penetration behavior of Weldox 460E steel plates with target thickness varying between 6 and 30 mm. The results are shown in Fig. 1.19. The slope of the initial-residual velocity curves decrease with increasing target thickness and the target deformation mode changes from global deflection to shear localization.

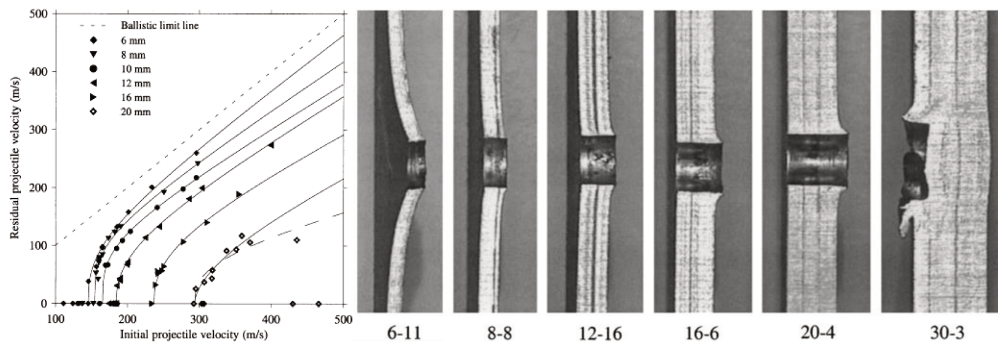


Fig. 1.19. (a) The residual-initial velocity curves and (b) the cross-section patterns of impacted targets with different thicknesses [33].

Rodríguez-Martínez et al. [39] studied the effect of target thickness on perforation behavior of 304 ASS thin plates using two kinds of projectiles, Fig. 1.20.

The results are shown in Fig. 1.21. The ballistic limit velocity was affected by a combination of target thickness and projectile shape: the ballistic limit velocity increased from 38 m/s to 75 m/s, a doubled increase, when conical projectile was adopted; while the corresponding ballistic limit velocity changed only from 95 m/s to 130 m/s with a hemispherical projectile.

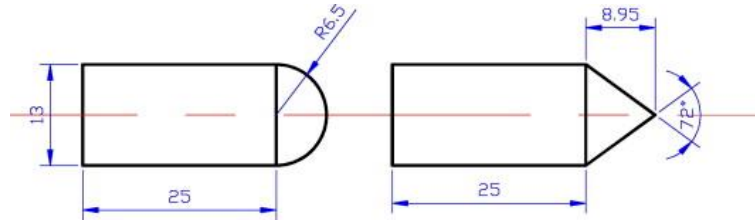


Fig. 1.20. Geometry and dimensions (mm) of the projectiles used in the experiments [39].

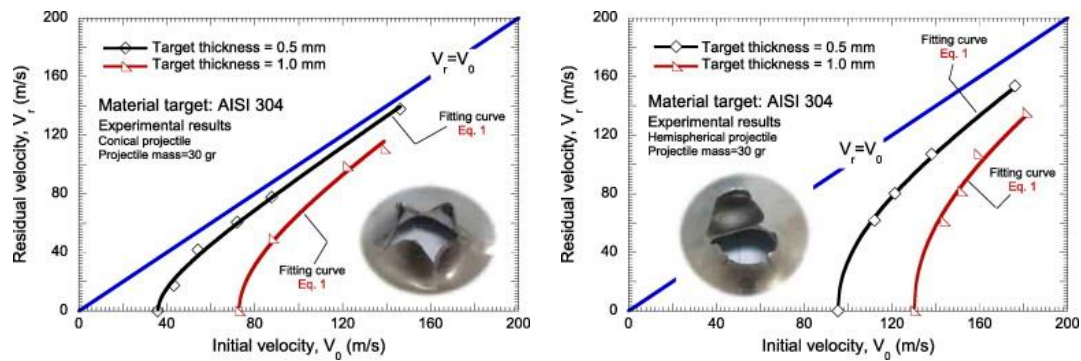


Fig. 1.21. The residual-initial velocity curves: (a) conical projectile configuration and (b) hemispherical projectile configuration [39].

Another parameter that has an influence on the ballistic impact behavior of thin plates is multiple-layered plates combination. Alavi Nia and Hoseini [85] compared ballistic resistance performance of monolithic, in-contact layered and spaced layered aluminium plates. They found that under the same total target thickness, the monolithic target behaves the best, followed by in-contact layered target and the spaced layered target behaves the worst. This is mainly because a bounding force between molecules inside the monolithic target exists, the energy needed to perforate

the plate is high. In case of in-contact layered target, deflection of the first layer is inhibited by the second and the third layers, so it behaves better than the spaced layered target.

Moreover, Børvik et al. [36,38] investigated the effects of projectile shape on perforation behavior of metallic materials. They conducted perforation tests of Weldox 460E steel plates using blunt, conical and hemispherical projectiles. The experimental results are shown in Fig. 1.22 and Fig. 1.23. It was found that both the energy absorption capacity and the failure mode of the material were affected by the projectile nose shape. The ballistic limit velocities are 185 m/s, 300 m/s and 300 m/s for blunt, conical and hemispherical projectiles, respectively. The failure mode for the blunt projectile was shear banding while conical and hemispherical projectiles perforated the target by pushing the material aside, corresponding to a failure by ductile hole enlargement.

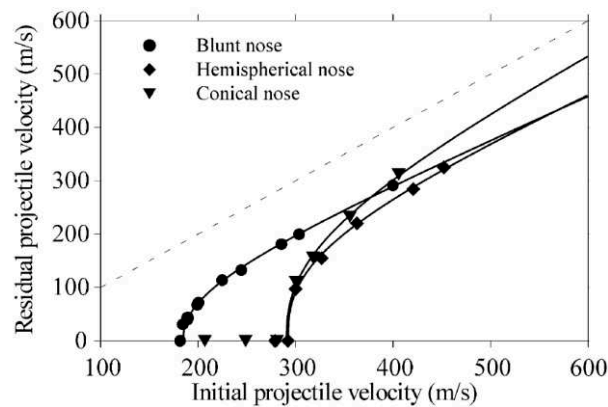
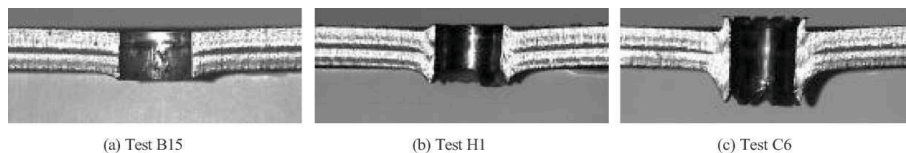


Fig. 1.22. The residual-initial velocity curves for different projectile nose shapes [36,38].



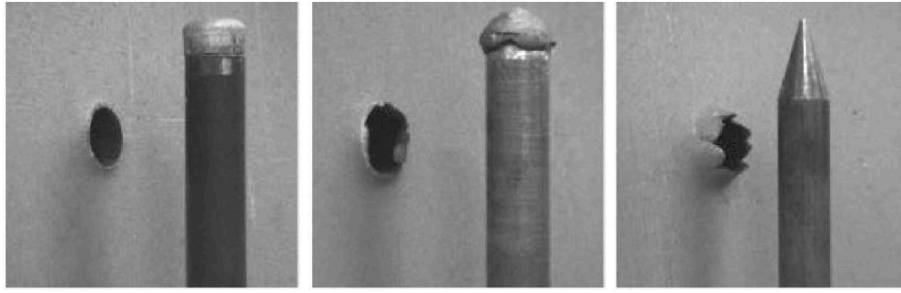


Fig. 1.23. (a) Cross-section surface and (b) fracture pattern and the plugs after tests [36,38].

5.2 Perforation behavior of thin plates under various temperatures

Concerning the perforation behavior of materials under various temperatures, quite a limited number of studies can be found. Mostly, the low temperature impact studies focus on hypervelocity impact of lightweight alloys and composites at around -173°C [40-43].

In addition, with a specially designed drop weight tower, the low velocity impact behavior of AA 2024-T3 aluminium and TRIP 1000 steel at -60°C was investigated by Martínez et al. [44,45]. The initial-residual velocity curves under different temperatures are shown in Fig. 1.24. It was found that the target absorbs larger impact energy with decreasing temperature, and the improved protection performance at low temperature comes from temperature sensitivity of materials. Under the same testing condition, he studied perforation behavior of TRIP 1000 steel and came to a similar conclusion. One should be noticed that no martensitic transformation was measured during perforation tests of TRIP steel, even at -60°C . Therefore, the improved protection performance of TRIP 1000 steel at low temperature comes from temperature sensitivity of the material instead of the originally assumed martensitic transformation.

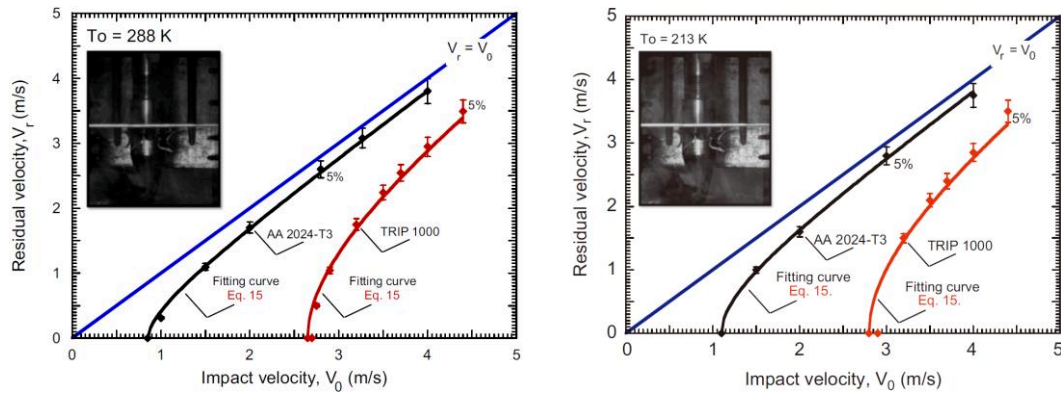


Fig. 1.24. The initial-residual velocity curves at (a) 213 K and (b) 288 K for AA 2024-T3 and TRIP 1000 sheets [45].

Concerning the impact behavior of materials under sub-ordnance or ordnance velocity at different temperatures, high temperature perforation by several authors were found [46-48]. Rusinek et al. [46] developed a heating chamber coupled to the ballistic impact device to investigate perforation behavior of Poly (Methyl methacrylate) (PMMA). With the thermal chamber, Klosak et al. [48] studied perforation behavior of brass alloy plates under temperatures ranging from 20°C to 260°C. The results are shown in Fig. 1.25 and Fig. 1.26. It can be seen that the energy absorption capacity decreased with increasing temperature. There were also some changes in the petalling failure mode: the number of petals increased from 3 to 6 within the testing temperature regime.

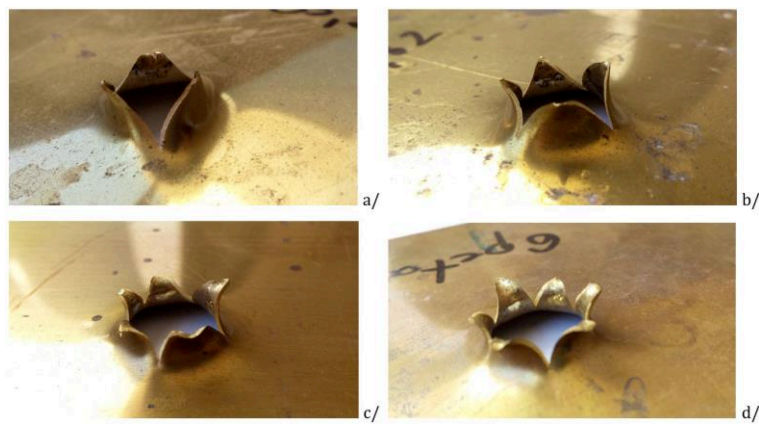


Fig. 1.25. Effect of initial temperature on failure patterns of standard brass alloy:

(a) 20°C, (b) 100°C, (c) 200°C and (d) 260°C [48].

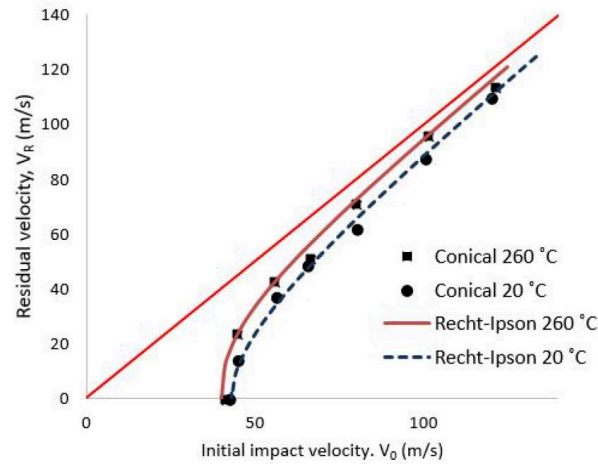


Fig. 1.26. The initial-residual velocity curves for 20°C and 260°C [48].

Liu et al. [47] investigated the ballistic performance of GH4169 alloy at temperatures ranging from 25°C to 600°C. A similar conclusion was obtained: larger plastic deformation of specimens and lower ballistic limit velocities at higher temperatures.

Conclusion

In this chapter, the current researches of 304 ASS under strain rates and temperatures have been reviewed.

First, martensitic transformation is commonly observed in 304 ASS and it affects the deformation behavior obviously. Therefore, the effects of strain rate and temperature on martensitic transformation have been reviewed. After that, effects of temperature and strain rate on constitutive behavior of 304 ASS was studied. The deformation mechanism is explained by taking martensitic transformation and dislocation slip into consideration. In addition, several commonly used models describing the constitutive behavior of metallic alloys and martensitic transformation in 304 ASS were introduced.

Second, to study deformation and failure behavior of 304 ASS under extreme high strain rates, several representative shear specimens and the corresponding testing techniques were introduced. The advantages and disadvantages of each design were discussed.

Finally, the perforation behavior of metallic alloys under various conditions has been studied. The study mainly focused on influence of target thickness, multiple-layered plates combination, projectile shape and testing temperature on perforation behavior such as the failure patterns and the initial-residual velocity curves.

Depending on the facilities available in the LCFC (Laboratoire de Conception Fabrication Commande) and LEM3 (Laboratoire d'Étude des Microstructures et de Mécanique des Matériaux) in Metz Campus of ENSAM (École Nationale Supérieure et d'Arts et Métiers), the deformation behavior of 304 ASS under different strain rates and temperatures will be studied. First, compression tests of 304 ASS under a wide range of strain rates and temperatures will be performed and the constitutive behavior will be modeled by an extension of the R-K model considering martensitic transformation phenomenon. Second, a new shear specimen for extreme high strain rate study will be designed. It works together with the conventional SHPB system without any clamping system or screws. In addition, a cooling device for low temperature perforation tests will be designed. With the cooling system, the effect of temperature on the perforation behavior of 304 ASS will be investigated.

References

- [1] Hickel T, Grabowski B, Körmann F, Neugebauer J. Advancing density functional theory to finite temperatures: methods and applications in steel design. *J Phys: Condens Matter* 2011;24:053202. doi:10.1088/0953-8984/24/5/053202.
- [2] Ishimaru E, Hamasaki H, Yoshida F. Deformation-induced martensitic transformation behavior of type 304 stainless steel sheet in draw-bending process.

Journal of Materials Processing Technology 2015;223:34–8.
doi:10.1016/j.jmatprotec.2015.03.048.

[3] Byun TS, Hashimoto N, Farrell K. Temperature dependence of strain hardening and plastic instability behaviors in austenitic stainless steels. *Acta Materialia* 2004;52:3889–99. doi:10.1016/j.actamat.2004.05.003.

[4] Masumura T, Nakada N, Tsuchiyama T, Takaki S, Koyano T, Adachi K. The difference in thermal and mechanical stabilities of austenite between carbon- and nitrogen-added metastable austenitic stainless steels. *Acta Materialia* 2015;84:330–8. doi:10.1016/j.actamat.2014.10.041.

[5] Beese AM, Mohr D. Effect of stress triaxiality and Lode angle on the kinetics of strain-induced austenite-to-martensite transformation. *Acta Materialia* 2011;59:2589–600. doi:10.1016/j.actamat.2010.12.040.

[6] Takaki S, Fukunaga K, Syarif J, Tsuchiyama T. Effect of Grain Refinement on Thermal Stability of Metastable Austenitic Steel. *Mater Trans* 2004;45:2245–51. doi:10.2320/matertrans.45.2245.

[7] Lichtenfeld JA, Van Tyne CJ, Mataya MC. Effect of strain rate on stress-strain behavior of alloy 309 and 304L austenitic stainless steel. *Metall and Mat Trans A* 2006;37:147–61. doi:10.1007/s11661-006-0160-5.

[8] Hamada AS, Karjalainen LP, Misra RDK, Talonen J. Contribution of deformation mechanisms to strength and ductility in two Cr–Mn grade austenitic stainless steels. *Materials Science and Engineering: A* 2013;559:336–44. doi:10.1016/j.msea.2012.08.108.

[9] Kim H, Lee J, Barlat F, Kim D, Lee M-G. Experiment and modeling to investigate the effect of stress state, strain and temperature on martensitic phase transformation in TRIP-assisted steel. *Acta Materialia* 2015;97:435–44.

doi:10.1016/j.actamat.2015.06.023.

[10] Curtze S, Kuokkala V-T, Hokka M, Peura P. Deformation behavior of TRIP and DP steels in tension at different temperatures over a wide range of strain rates. *Materials Science and Engineering: A* 2009;507:124–31. doi:10.1016/j.msea.2008.11.050.

[11] Rodríguez-Martínez JA, Rusinek A, Pesci R. Experimental survey on the behaviour of AISI 304 steel sheets subjected to perforation. *Thin-Walled Structures* 2010;48:966–78. doi:10.1016/j.tws.2010.07.005.

[12] Hecker SS, Stout MG, Staudhammer KP, Smith JL. Effects of Strain State and Strain Rate on Deformation-Induced Transformation in 304 Stainless Steel: Part I. Magnetic Measurements and Mechanical Behavior. *MTA* 1982;13:619–26. doi:10.1007/BF02644427.

[13] Murr LE, Staudhammer KP, Hecker SS. Effects of Strain State and Strain Rate on Deformation-Induced Transformation in 304 Stainless Steel: Part II. Microstructural Study. *MTA* 1982;13:627–35. doi:10.1007/BF02644428.

[14] Talonen J, Hänninen H, Nenonen P, Pape G. Effect of strain rate on the strain-induced $\gamma \rightarrow \alpha'$ -martensite transformation and mechanical properties of austenitic stainless steels. *Metall and Mat Trans A* 2005;36:421–32. doi:10.1007/s11661-005-0313-y.

[15] Chen AY, Ruan HH, Wang J, Chan HL, Wang Q, Li Q, et al. The influence of strain rate on the microstructure transition of 304 stainless steel. *Acta Materialia* 2011;59:3697–709. doi:10.1016/j.actamat.2011.03.005.

[16] Meyers MA. *Dynamic Behavior of Materials*. John Wiley & Sons; 1994.

[17] Zheng C, Yu W. Effect of low-temperature on mechanical behavior for an AISI 304 austenitic stainless steel. *Materials Science and Engineering: A* 2018;710:359–

65. doi:10.1016/j.msea.2017.11.003.

[18] Lee W-S, Lin C-F. Impact properties and microstructure evolution of 304L stainless steel. *Materials Science and Engineering: A* 2001;308:124–35. doi:10.1016/S0921-5093(00)02024-4.

[19] Park WS, Yoo SW, Kim MH, Lee JM. Strain-rate effects on the mechanical behavior of the AISI 300 series of austenitic stainless steel under cryogenic environments. *Materials & Design* 2010;31:3630–40. doi:10.1016/j.matdes.2010.02.041.

[20] Park WS, Chun MS, Han MS, Kim MH, Lee JM. Comparative study on mechanical behavior of low temperature application materials for ships and offshore structures: Part I—Experimental investigations. *Materials Science and Engineering: A* 2011;528:5790–803. doi:10.1016/j.msea.2011.04.032.

[21] Ishikawa K, Tanimura S. Strain rate sensitivity of flow stress at low temperatures in 304n stainless steel. *International Journal of Plasticity* 1992;8:947–58. doi:10.1016/0749-6419(92)90044-D.

[22] Lin YC, Chen X-M. A critical review of experimental results and constitutive descriptions for metals and alloys in hot working. *Materials & Design* 2011;32:1733–59. doi:10.1016/j.matdes.2010.11.048.

[23] Johnson GR, Cook WH, Johnson G, Cook W. A constitutive model and data for metals subjected to large strains, high strain rates and high temperatures n.d.

[24] Khan AS, Huang S. Experimental and theoretical study of mechanical behavior of 1100 aluminum in the strain rate range 10^{-5} – 10^4 s⁻¹. *International Journal of Plasticity* 1992;8:397–424. doi:10.1016/0749-6419(92)90057-J.

[25] Khan AS, Zhang H, Takacs L. Mechanical response and modeling of fully compacted nanocrystalline iron and copper. *International Journal of Plasticity*

2000;16:1459–76. doi:10.1016/S0749-6419(00)00023-1.

[26] Khan AS, Sung Suh Y, Kazmi R. Quasi-static and dynamic loading responses and constitutive modeling of titanium alloys. *International Journal of Plasticity* 2004;20:2233–48. doi:10.1016/j.ijplas.2003.06.005.

[27] Khan AS, Suh YS, Chen X, Takacs L, Zhang H. Nanocrystalline aluminum and iron: Mechanical behavior at quasi-static and high strain rates, and constitutive modeling. *International Journal of Plasticity* 2006;22:195–209. doi:10.1016/j.ijplas.2004.07.008.

[28] Zener C, Hollomon JH. Effect of Strain Rate Upon Plastic Flow of Steel. *Journal of Applied Physics* 1944;15:22–32. doi:10.1063/1.1707363.

[29] Shi H, McLaren AJ, Sellars CM, Shahani R, Bolingbroke R. Constitutive equations for high temperature flow stress of aluminium alloys. *Materials Science and Technology* 1997;13:210–6. doi:10.1179/mst.1997.13.3.210.

[30] Shin H, Kim J-B. A Phenomenological Constitutive Equation to Describe Various Flow Stress Behaviors of Materials in Wide Strain Rate and Temperature Regimes. *J Eng Mater Technol* 2010;132:021009-021009–6. doi:10.1115/1.4000225.

[31] Zhang H, Wen W, Cui H. Behaviors of IC10 alloy over a wide range of strain rates and temperatures: Experiments and modeling. *Materials Science and Engineering: A* 2009;504:99–103. doi:10.1016/j.msea.2008.10.056.

[32] Vural M, Caro J. Experimental analysis and constitutive modeling for the newly developed 2139-T8 alloy. *Materials Science and Engineering: A* 2009;520:56–65. doi:10.1016/j.msea.2009.05.026.

[33] Lin YC, Chen X-M. A combined Johnson–Cook and Zerilli–Armstrong model for hot compressed typical high-strength alloy steel. *Computational Materials*

Science 2010;49:628–33. doi:10.1016/j.commatsci.2010.06.004.

[34] Laidler KJ. The development of the Arrhenius equation. J Chem Educ 1984;61:494. doi:10.1021/ed061p494.

[35] Lin YC, Chen M-S, Zhong J. Constitutive modeling for elevated temperature flow behavior of 42CrMo steel. Computational Materials Science 2008;42:470–7. doi:10.1016/j.commatsci.2007.08.011.

[36] Zerilli FJ, Armstrong RW. Dislocation-mechanics-based constitutive relations for material dynamics calculations. Journal of Applied Physics 1987;61:1816–25. doi:10.1063/1.338024.

[37] Bodner SR, Partom Y. Constitutive Equations for Elastic-Viscoplastic Strain-Hardening Materials. J Appl Mech 1975;42:385–9. doi:10.1115/1.3423586.

[38] Rusinek A, Klepaczko JR. Shear testing of a sheet steel at wide range of strain rates and a constitutive relation with strain-rate and temperature dependence of the flow stress. International Journal of Plasticity 2001;17:87–115. doi:10.1016/S0749-6419(00)00020-6.

[39] Zhang H, Wen W, Cui H, Xu Y. A modified Zerilli–Armstrong model for alloy IC10 over a wide range of temperatures and strain rates. Materials Science and Engineering: A 2009;527:328–33. doi:10.1016/j.msea.2009.08.008.

[40] Samantaray D, Mandal S, Bhaduri AK. A comparative study on Johnson Cook, modified Zerilli–Armstrong and Arrhenius-type constitutive models to predict elevated temperature flow behaviour in modified 9Cr–1Mo steel. Computational Materials Science 2009;47:568–76. doi:10.1016/j.commatsci.2009.09.025.

[41] Gao CY, Zhang LC. A constitutive model for dynamic plasticity of FCC metals. Materials Science and Engineering: A 2010;527:3138–43.

doi:10.1016/j.msea.2010.01.083.

[42] Abed FH, Voyiadjis GZ. A consistent modified Zerilli-Armstrong flow stress model for BCC and FCC metals for elevated temperatures. *Acta Mechanica* 2005;175:1–18. doi:10.1007/s00707-004-0203-1.

[43] Noble JP, Harding J. An evaluation of constitutive relations for high-rate material behaviour using the tensile Hopkinson-bar. *J Phys IV France* 1994;04:C8-477-C8-482. doi:10.1051/jp4:1994874.

[44] Kocks UF, Argon AS, Ashby MF. *Thermodynamics and Kinetics of Slip*. Argonne National Laboratory; 1973.

[45] Rusinek A, Rodríguez-Martínez JA. Thermo-viscoplastic constitutive relation for aluminium alloys, modeling of negative strain rate sensitivity and viscous drag effects. *Materials & Design* 2009;30:4377–90. doi:10.1016/j.matdes.2009.04.011.

[46] Olson GB, Cohen M. Kinetics of strain-induced martensitic nucleation. *MTA* 1975;6:791. doi:10.1007/BF02672301.

[47] Stringfellow RG, Parks DM, Olson GB. A constitutive model for transformation plasticity accompanying strain-induced martensitic transformations in metastable austenitic steels. *Acta Metallurgica et Materialia* 1992;40:1703–16. doi:10.1016/0956-7151(92)90114-T.

[48] Tomita Y, Iwamoto T. Constitutive modeling of trip steel and its application to the improvement of mechanical properties. *International Journal of Mechanical Sciences* 1995;37:1295–305. doi:10.1016/0020-7403(95)00039-Z.

[49] Xu Z, Ding X, Zhang W, Huang F. A novel method in dynamic shear testing of bulk materials using the traditional SHPB technique. *International Journal of Impact Engineering* 2017;101:90–104. doi:10.1016/j.ijimpeng.2016.11.012.

[50] Xu Z, Liu Y, Sun Z, Hu H, Huang F. On shear failure behaviors of an armor

steel over a large range of strain rates. *International Journal of Impact Engineering* 2018;118:24–38. doi:10.1016/j.ijimpeng.2018.04.003.

[51] Klepaczko JR, Nguyen HV, Nowacki WK. Quasi-static and dynamic shearing of sheet metals. *European Journal of Mechanics - A/Solids* 1999;18:271–89. doi:10.1016/S0997-7538(99)80016-3.

[52] Klepaczko JR. An experimental technique for shear testing at high and very high strain rates. The case of a mild steel. *International Journal of Impact Engineering* 1994;15:25–39. doi:10.1016/S0734-743X(05)80005-3.

[53] Bai Y, Wierzbicki T. A new model of metal plasticity and fracture with pressure and Lode dependence. *International Journal of Plasticity* 2008;24:1071–96. doi:10.1016/j.ijplas.2007.09.004.

[54] Dunand M, Mohr D. Predicting the rate-dependent loading paths to fracture in advanced high strength steels using an extended mechanical threshold model. *International Journal of Impact Engineering* 2017;108:272–85. doi:10.1016/j.ijimpeng.2017.02.020.

[55] Fras T, Roth CC, Mohr D. Fracture of high-strength armor steel under impact loading. *International Journal of Impact Engineering* 2018;111:147–64. doi:10.1016/j.ijimpeng.2017.09.009.

[56] Dorogoy A, Rittel D, Godinger A. Modification of the Shear-Compression Specimen for Large Strain Testing. *Exp Mech* 2015;55:1627–39. doi:10.1007/s11340-015-0057-6.

[57] Dorogoy A, Rittel D, Godinger A. A Shear-Tension Specimen for Large Strain Testing. *Exp Mech* 2016;56:437–49. doi:10.1007/s11340-015-0106-1.

[58] Francart C, Demarty Y, Bahlouli N, Ahzi S. Dynamic Characterization and Modeling of Ductile Failure of Sintered Aluminum Alloy through Shear-

compression Tests. *Procedia Engineering* 2017;197:69–78.
doi:10.1016/j.proeng.2017.08.083.

[59] Duffy J, Campbell JD, Hawley RH. On the Use of a Torsional Split Hopkinson Bar to Study Rate Effects in 1100-0 Aluminum. *J Appl Mech* 1971;38:83–91.
doi:10.1115/1.3408771.

[60] Meyers MA, Staudhammer KP, Murr LE. Metallurgical applications of shock-wave and high-strain-rate phenomena. Dekker; 1986.

[61] Campbell JD, Ferguson WG. The temperature and strain-rate dependence of the shear strength of mild steel. *The Philosophical Magazine: A Journal of Theoretical Experimental and Applied Physics* 1970;21:63–82.
doi:10.1080/14786437008238397.

[62] Duffy J, Chi YC. On the measurement of local strain and temperature during the formation of adiabatic shear bands. *Materials Science and Engineering: A* 1992;157:195–210. doi:10.1016/0921-5093(92)90026-W.

[63] Meyers MA, Xu YB, Xue Q, Pérez-Prado MT, McNelley TR. Microstructural evolution in adiabatic shear localization in stainless steel. *Acta Materialia* 2003;51:1307–25. doi:10.1016/S1359-6454(02)00526-8.

[64] Bronkhorst CA, Cerreta EK, Xue Q, Maudlin PJ, Mason TA, Gray GT. An experimental and numerical study of the localization behavior of tantalum and stainless steel. *International Journal of Plasticity* 2006;22:1304–35.
doi:10.1016/j.ijplas.2005.10.002.

[65] Peirs J, Verleysen P, Degrieck J, Coghe F. The use of hat-shaped specimens to study the high strain rate shear behaviour of Ti–6Al–4V. *International Journal of Impact Engineering* 2010;37:703–14. doi:10.1016/j.ijimpeng.2009.08.002.

[66] Spatial evolution of adiabatic shear localization in stainless steel, titanium, and

titanium-aluminum-vanadium alloy. 2002.

[67] Shi FF, Merle R, Hou B, Liu JG, Li YL, Zhao H. A critical analysis of plane shear tests under quasi-static and impact loading. *International Journal of Impact Engineering* 2014;74:107–19. doi:10.1016/j.ijimpeng.2014.06.012.

[68] Harding J, Huddart J. The use of the double-notch shear test in determining the mechanical properties of uranium at very high rates of strain. *Mechanical Properties at High Rates of Strain*, 1979 1980.

[69] Guo Y, Li Y. A Novel Approach to Testing the Dynamic Shear Response of Ti-6Al-4V. *Acta Mech Solida Sin* 2012;25:299–311. doi:10.1016/S0894-9166(12)60027-5.

[70] Bonnet-Lebouvier AS, Klepaczko JR. Numerical study of shear deformation in Ti-6Al-4V at medium and high strain rates, critical impact velocity in shear. *International Journal of Impact Engineering* 2002;27:755–69. doi:10.1016/S0734-743X(02)00010-6.

[71] Gray GT, Vecchio KS, Livescu V. Compact forced simple-shear sample for studying shear localization in materials. *Acta Materialia* 2016;103:12–22. doi:10.1016/j.actamat.2015.09.051.

[72] Chen G, Hao Y, Chen X, Hao H. Compressive behaviour of tungsten fibre reinforced Zr-based metallic glass at different strain rates and temperatures. *International Journal of Impact Engineering* 2017;106:110–9. doi:10.1016/j.ijimpeng.2017.03.017.

[73] Critical Appraisal of Limiting Strain Rates for Compression Testing of Ceramics in a Split Hopkinson Pressure Bar - Ravichandran - 1994 - *Journal of the American Ceramic Society* - Wiley Online Library n.d. <https://ceramics.onlinelibrary.wiley.com/doi/abs/10.1111/j.1151-2916.1994.tb06987.x> (accessed March 20, 2019).

- [74] Lindholm US. Some experiments with the split hopkinson pressure bar*. *Journal of the Mechanics and Physics of Solids* 1964;12:317–35. doi:10.1016/0022-5096(64)90028-6.
- [75] Marchand A, Duffy J. An experimental study of the formation process of adiabatic shear bands in a structural steel. *Journal of the Mechanics and Physics of Solids* 1988;36:251–83. doi:10.1016/0022-5096(88)90012-9.
- [76] Dodd B, Bai Y. *Adiabatic Shear Localization: Frontiers and Advances*. Elsevier; 2012.
- [77] Meyer LW, Krüger L. Drop-weight compression shear testing. *ASM Handbook* 2000;8:452–454.
- [78] Krüger L, Meyer LW, Razorenov SV, Kanel GI. Investigation of dynamic flow and strength properties of Ti-6-22-22S at normal and elevated temperatures. *International Journal of Impact Engineering* 2003;28:877–90. doi:10.1016/S0734-743X(02)00151-3.
- [79] Rusinek A, Rodríguez-Martínez JA, Zaera R, Klepaczko JR, Arias A, Sauvelet C. Experimental and numerical study on the perforation process of mild steel sheets subjected to perpendicular impact by hemispherical projectiles. *International Journal of Impact Engineering* 2009;36:565–87. doi:10.1016/j.ijimpeng.2008.09.004.
- [80] Børvik T, Langseth M, Hopperstad OS, Malo KA. Ballistic penetration of steel plates. *International Journal of Impact Engineering* 1999;22:855–86. doi:10.1016/S0734-743X(99)00011-1.
- [81] Antoinat L, Kubler R, Barou J-L, Viot P, Barrallier L. Perforation of aluminium alloy thin plates. *International Journal of Impact Engineering* 2015;75:255–67. doi:10.1016/j.ijimpeng.2014.07.017.
- [82] Numata D, Ohtani K, Anyoji M, Takayama K, Togami K, Sun M. HVI tests on

CFRP laminates at low temperature. *International Journal of Impact Engineering* 2008;35:1695–701. doi:10.1016/j.ijimpeng.2008.07.055.

[83] Børvik T, Hopperstad OS, Langseth M, Malo KA. Effect of target thickness in blunt projectile penetration of Weldox 460 E steel plates. *International Journal of Impact Engineering* 2003;28:413–64. doi:10.1016/S0734-743X(02)00072-6.

[84] Goldsmith W, Finnegan SA. Normal and oblique impact of cylindro-conical and cylindrical projectiles on metallic plates. *International Journal of Impact Engineering* 1986;4:83–105. doi:10.1016/0734-743X(86)90010-2.

[85] Alavi Nia A, Hoseini GR. Experimental study of perforation of multi-layered targets by hemispherical-nosed projectiles. *Materials & Design* 2011;32:1057–65. doi:10.1016/j.matdes.2010.07.001.

[86] Børvik T, Hopperstad OS, Berstad T, Langseth M. Perforation of 12mm thick steel plates by 20mm diameter projectiles with flat, hemispherical and conical noses: Part II: numerical simulations. *International Journal of Impact Engineering* 2002;27:37–64. doi:10.1016/S0734-743X(01)00035-5.

[87] Arias A, Rodríguez-Martínez JA, Rusinek A. Numerical simulations of impact behaviour of thin steel plates subjected to cylindrical, conical and hemispherical non-deformable projectiles. *Engineering Fracture Mechanics* 2008;75:1635–56. doi:10.1016/j.engfracmech.2007.06.005.

[88] Børvik T, Langseth M, Hopperstad OS, Malo KA. Perforation of 12mm thick steel plates by 20mm diameter projectiles with flat, hemispherical and conical noses: Part I: Experimental study. *International Journal of Impact Engineering* 2002;27:19–35. doi:10.1016/S0734-743X(01)00034-3.

[89] Rodríguez-Martínez JA, Rusinek A, Pesci R, Zaera R. Experimental and numerical analysis of the martensitic transformation in AISI 304 steel sheets subjected to perforation by conical and hemispherical projectiles. *International*

Journal of Solids and Structures 2013;50:339–51. doi:10.1016/j.ijsolstr.2012.09.019.

[90] Ohtani K, Numata D, Kikuchi T, Sun M, Takayama K, Togami K. A study of hypervelocity impact on cryogenic materials. International Journal of Impact Engineering 2006;33:555–65. doi:10.1016/j.ijimpeng.2006.09.025.

[91] Tanaka K, Nishida M, Takada N. High-speed penetration of a projectile into aluminum alloys at low temperatures. International Journal of Impact Engineering 2006;33:788–98. doi:10.1016/j.ijimpeng.2006.09.089.

[92] Numata D, Ohtani K, Anyoji M, Takayama K, Sun M. Experimental study of hypervelocity impacts at low temperatures. Shock Waves 2008;18:169–83. doi:10.1007/s00193-008-0156-8.

[93] Tanaka K, Nishida M, Ogawa H, Akahori M, Aikawa F. Hypervelocity crater formation in aluminum alloys at low temperatures. International Journal of Impact Engineering 2008;35:1821–6. doi:10.1016/j.ijimpeng.2008.07.043.

[94] Rodríguez-Martínez JA, Rusinek A, Arias A. Thermo-viscoplastic behaviour of 2024-T3 aluminium sheets subjected to low velocity perforation at different temperatures. Thin-Walled Structures 2011;49:819–32. doi:10.1016/j.tws.2011.02.007.

[95] Rodríguez-Martínez JA, Pesci R, Rusinek A, Arias A, Zaera R, Pedroche DA. Thermo-mechanical behaviour of TRIP 1000 steel sheets subjected to low velocity perforation by conical projectiles at different temperatures. International Journal of Solids and Structures 2010;47:1268–84. doi:10.1016/j.ijsolstr.2010.01.013.

[96] Rusinek A, Bernier R, Boumbimba RM, Klosak M, Jankowiak T, Voyiadjis GZ. New devices to capture the temperature effect under dynamic compression and impact perforation of polymers, application to PMMA. Polymer Testing 2018;65:1–9. doi:10.1016/j.polymertesting.2017.10.015.

- [97] Liu J, Zheng B, Zhang K, Yang B, Yu X. Ballistic performance and energy absorption characteristics of thin nickel-based alloy plates at elevated temperatures. *International Journal of Impact Engineering* 2019;126:160–71. doi:10.1016/j.ijimpeng.2018.12.012.
- [98] Klosak M, Rusinek A, Bendarma A, Jankowiak T, Lodygowski T, Klosak M, et al. Experimental study of brass properties through perforation tests using a thermal chamber for elevated temperatures. *Latin American Journal of Solids and Structures* 2018;15. doi:10.1590/1679-78254346.

Chapter 2 Thermo-viscoplastic behavior of 304 ASS

1. Introduction

The deformation behavior of 304 ASS has been massively studied. However, previous studies mainly focused on quasi-static behavior at various temperatures or dynamic behavior at room temperature, while the combined effects of temperature and dynamic loading on mechanical properties of 304 ASS are frequently encountered: LNG storage (-163°C) and sheet metal forming (20°C to 300°C), for which the corresponding deformation behavior is not clearly understood. In addition, at temperature above M_d , the deformation behavior of 304 ASS is similar to that of the commonly used steels. However, at temperature lower than M_d , the deformation behavior of 304 ASS becomes complex due to the SIMT effect. Hence, a deformation behavior study of 304 ASS especially focusing on temperatures below M_d (140°C for the studied material) can be interesting.

In this chapter, the compression behavior of 304 ASS at strain rates from 10^{-3} s^{-1} to 3270 s^{-1} and temperatures from -163°C to 172°C has been investigated. First, a self-designed heating furnace/cooling device is coupled to the conventional SHPB device for dynamic compression tests not only at low but also at elevated temperatures. The set-up reliability is verified by both experiments and thermal simulations. Then, compression tests of 304 ASS have been conducted, and then influence of temperature and strain rate on the deformation behavior of 304 ASS are discussed in details. An extension of the Rusinek–Klepaczko (RK) constitutive model [1,2] considering martensitic transformation phenomenon is chosen to describe the temperature and strain rate dependent constitutive behavior of 304 ASS. By comparing the experimental and numerical results, the extended RK model is proven to be able to describe the deformation behavior of 304 ASS including its martensitic transformation behavior correctly.

2. Material behavior and set-up description

2.1 Material and specimen

The material considered herein is a commercial 304 stainless steel produced by Thyssenkrupp Materials, available in annealed plates (dimensions: 1000*100*12 mm³). According to the manufacturer's specification, the chemical composition of the steel is given in Table. 2.1.

The specimens used for compression tests are cylinders 3 mm high ($L=3$ mm) and 6 mm in diameter ($\phi=6$ mm): a height to diameter ratio of $s_0=0.5$ is chosen to reduce friction and inertia effects as reported in [3]. They were machined from the as-received plate along the rolling direction using wire electrical discharge machining (WEDM) to avoid causing martensitic transformation. To avoid bulking effect and to ensure a uniform stress state inside the specimens, the end faces of the specimens were coated with lubricant. To ensure the reliability of the experimental results, three tests were performed for each temperature and strain rate combination, and the average curve for each condition is depicted as reference in this work.

Table. 2.1. Chemical composition of the 304 ASS obtained from the producer (wt%).

Material	C	Cr	Mn	N	Ni	Co	Cu	Fe
304 ASS	0.018	17.60	1.64	0.72	8.04	0.20	0.33	Bal

2.2 Quasi-static and dynamic compression tests

Quasi-static compression tests at room temperature were conducted using a

Zwick/Roell 200kN universal testing machine. Four strain rates were considered: 10^{-3} s^{-1} , 10^{-2} s^{-1} , 10^{-1} s^{-1} and 1 s^{-1} . For tests at low and elevated temperatures, -163°C , -60°C , -20°C , 88°C and 172°C , a cooling chamber or a heating furnace were used.

To study dynamic compression behavior of 304 ASS, compression tests with average strain rates around 10^3 s^{-1} and initial temperatures varying from -163°C to 172°C were carried out using an SHPB set-up. According to the one-dimensional wave propagation theory, the engineering strain rate $\dot{\gamma}_e(t)$, the engineering strain $\gamma_e(t)$ and the engineering stress $\tau_e(t)$ in the compression specimen can be calculated. Then, the true stress-true strain curves of the tested materials are calculated by Eq. 2.1.

$$\begin{cases} \sigma_{true} = \sigma_{engineering}(1 + \varepsilon_{engineering}) \\ \varepsilon_{true} = \ln(1 + \varepsilon_{engineering}) \end{cases} \quad \text{Eq. 2.1}$$

In addition, the compression behavior of the tested material is commonly disturbed by the friction effect between the specimen and the SHPB bars. This phenomenon is closely related to several parameters such as the friction coefficient μ , the diameter (ϕ) and length (L) of the compression specimen. To avoid the friction effect on the experimentally obtained stress-strain relationships, data correction is needed, Eq. 2.2 [4-6].

$$\begin{cases} \sigma_{real}(\varepsilon) = \sigma_{true}(\varepsilon) - \Delta\sigma_{friction} \\ \Delta\sigma_{friction} = \sigma_{true} \left(1 - \frac{\mu \phi}{3 L}\right) \end{cases} \quad \text{Eq. 2.2}$$

After several calculations above, the constitutive behavior of 304 ASS can be determined from the compression tests accurately. It should be noticed that all the several procedures are carried out using the lab developed software waves analysis and study program (WASP).

Concerning dynamic tests at elevated temperatures, a heating furnace coupled to the conventional SHPB set-up is adopted. An illustration of the temperature-

controlling heating furnace is shown in Fig. 2.1. During the heating process, the specimen, together with part of the incident and transmitter bars, are heated. Two thermocouples are used to monitor the temperature in the specimen and the environmental temperature inside the furnace that can provide feedback to the temperature controller to adjust the heating rate. The maximum testing temperature by the heating furnace is close to 250°C.

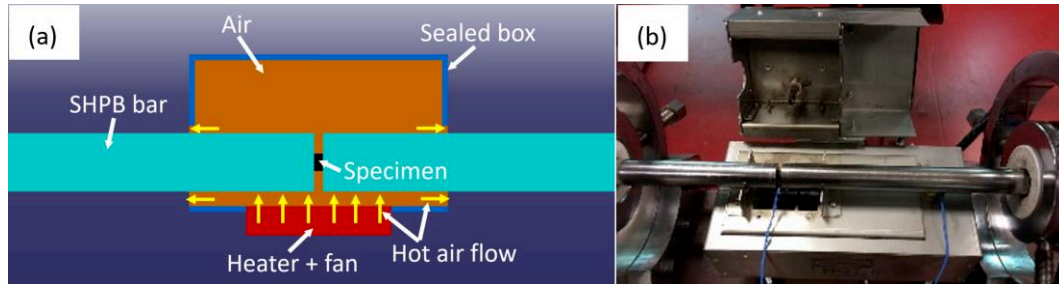


Fig. 2.1. Heating furnace in the SHPB system for dynamic tests at elevated temperatures: (a) schematic illustration and (b) complete device.

Concerning dynamic compression tests at low temperatures, a specific cooling device based on pulsed cryogenic gas has been developed, Fig. 2.2 (a). The cold nitrogen gas flows from a liquid nitrogen tank through an aluminium pipe into the cooling box. The temperature inside the cooling box is monitored by a thermocouple connected to a temperature controller. Once the environmental temperature inside the box reaches the set value, the temperature controller cuts off the power of the pump to stop the nitrogen gas flow. By this method, the temperature varies precisely from -90°C to -20°C. In addition, to decrease strongly the initial temperature, the chamber is filled with liquid nitrogen directly. Therefore, the minimum temperature reached is close to -163°C.

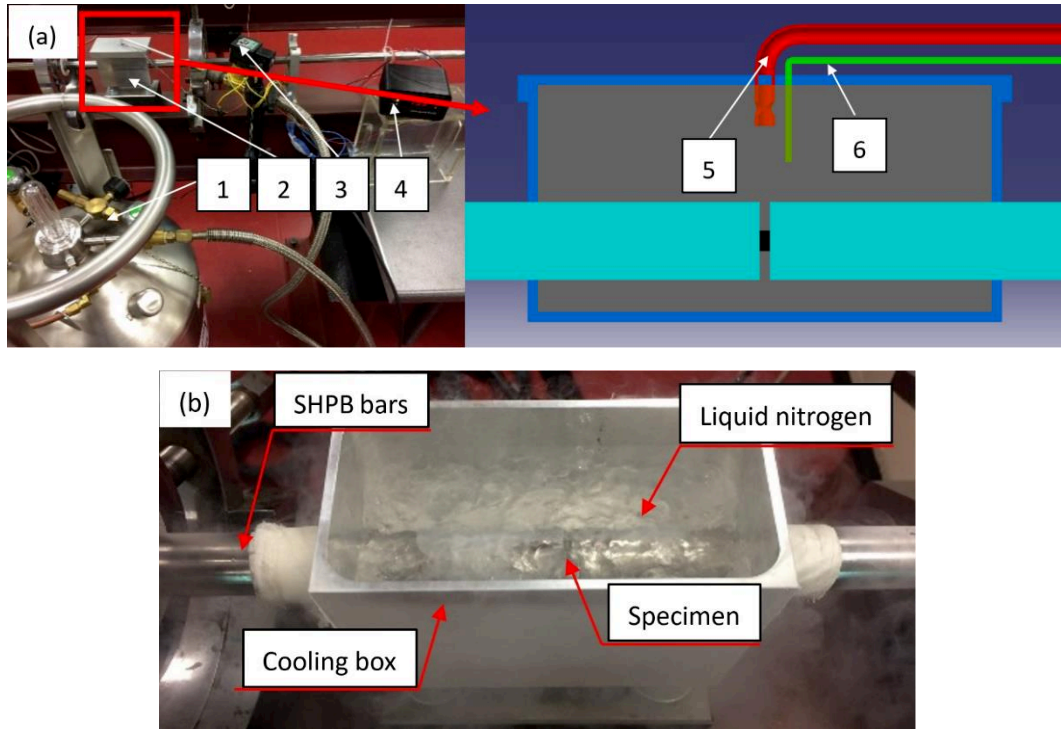


Fig. 2.2. Cooling device to reach low temperatures (a) between -90°C and -20°C and (b) -163°C : 1) liquid nitrogen tank, 2) cooling box, 3) pump for nitrogen gas flow, 4) temperature controller, 5) pipe for the nitrogen gas flow, 6) thermocouple.

Since the heating furnace/cooling devices for high/low temperature tests are originally developed, their reliability should be checked before testing. Hence, the temperature evolution of the heating furnace/cooling device has been measured experimentally and is presented in the next section. In addition, the temperature distribution inside the specimens was further estimated by a FEM model based on thermal heat transfer approach.

3. Calibration and heat transfer modelling of the heating furnace/cooling device

The temperature evolution in the compression specimen and the environment is measured experimentally, and the results are shown in Fig. 2.3. By setting the environmental temperatures of the heating furnace/cooling box to be 200°C , 100°C ,

-25°C, -68°C and -163°C, the corresponding temperatures of the specimens are 172°C, 88°C, -20°C, -60°C and -163°C, respectively. The waiting time T_w for the specimen temperature to be stable changes depending on the initial temperature T_0 . It increases from $T_w = 270$ s at -163°C continuously to $T_w = 1820$ s at 172°C. This is because with increasing testing temperature, the specific heat of 304 ASS increases more significantly than the heating transfer coefficient between 304 ASS and the environment. Therefore, it takes a longer time to obtain a uniform temperature distribution in the specimen. Values of T_0 are comparatively smaller for lower testing temperatures as the By changing the environmental temperatures between -163°C and 200°C, dynamic compression behavior of materials under temperatures between -163°C and 172°C can be studied.

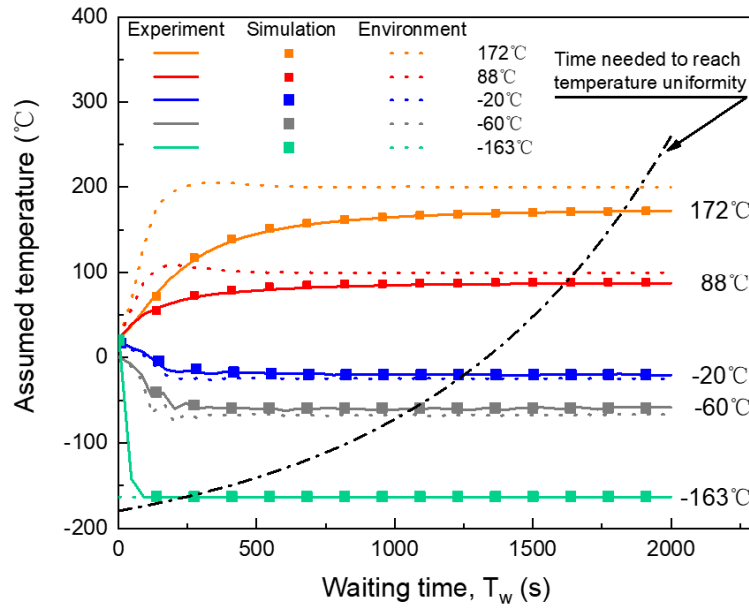


Fig. 2.3. Temperature evolution in the compression specimens with the environmental temperatures set between -163°C and 200°C.

To analyze the temperature distribution of the heating furnace/cooling box more precisely, numerical simulations using COMSOL Multiphysics have been conducted. The thermal transfer is described by the generalized transient heat equation, Eq. 2.3.

$$\rho \cdot C_p(T) \cdot \frac{\partial T}{\partial t} - \nabla \cdot (k(T) \cdot \nabla T) = 0 \quad \text{Eq. 2.3}$$

The thermal conductivity $k(T)$ and the specific heat $C_p(T)$ of the materials used in the numerical simulation may be found in [7]. The boundary conditions are defined as follows:

- Natural convective heat flux q_c on the free surface of the heating furnace/cooling device and the SHPB bars.
- Forced convective heat flux q_f through the free surface of the specimen and the SHPB bars, due to the flow of the hot air, nitrogen gas or liquid nitrogen.
- Thermal contact heat q_{int} between different interfaces of the specimen and the SHPB bars.
- Hot air inflow and outflow with certain temperatures and velocities.

$$\begin{cases} q_c = -h_c(T - T_0) & \text{in } \partial\Omega_c \\ q_f = -h_f(T - T_0) & \text{in } \partial\Omega_f \\ q_{int} = h_{int}(T - T_0) & \text{in } \partial\Omega_{int} \end{cases} \quad \text{Eq. 2.4}$$

where $h_c = 10 \text{ W}/(\text{m}^2 \cdot \text{K})$ and $h_{int} = 10^5 \text{ W}/(\text{m}^2 \cdot \text{K})$ are the natural heat convection and the layer conductance coefficients, respectively. Values of h_c and h_{int} may be found in [8]. The forced heat convection coefficient h_f is equal to $818 \text{ W}/(\text{m}^2 \cdot \text{K})$ when cooling down the specimen by liquid nitrogen and $109 \text{ W}/(\text{m}^2 \cdot \text{K})$ when nitrogen gas or hot air is used. Values of h_f were obtained by fitting numerical data to the experimental results.

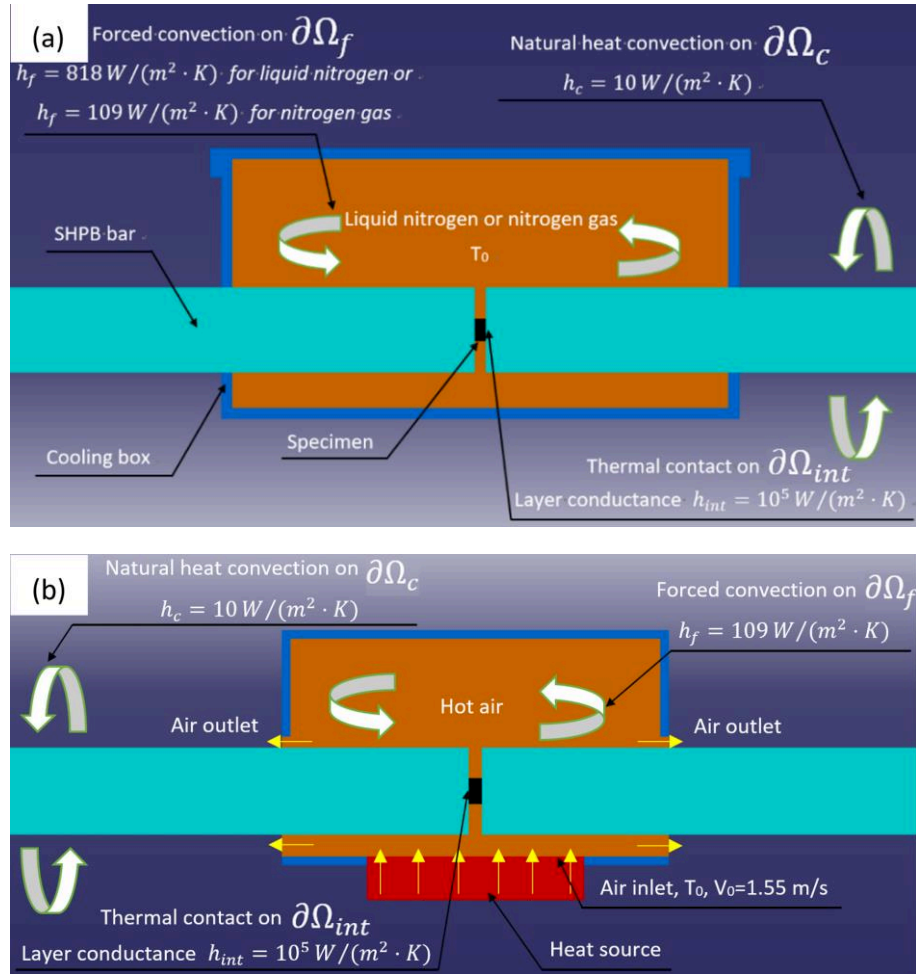


Fig. 2.4. Boundary conditions for temperature distribution analysis using COMSOL Multiphysics: (a) low temperature and (b) elevated temperature.

The numerical results are shown in Fig. 2.3. It is observed that the numerical predictions agree well with the experiments. Therefore, the numerical simulations may predict the temperature evolution and distribution of the heating furnace/cooling device correctly.

Based on the numerical simulations, the temperature evolution of four positions shown in Fig. 2.5 (a) was recorded; the results are given in Fig. 2.5 (b). Temperatures in points A and B are always the same: it means that a uniform temperature distribution is obtained within the compression specimen. In comparison, temperatures in points C and D are lower because of the heat exchange between the

SHPB bars and the air environment. The temperature difference between the four points increases when the testing temperature deviates obviously from room temperature, and a strong temperature gradient along the SHPB bars is observed for $T_0 = -163^\circ\text{C}$ and 200°C .

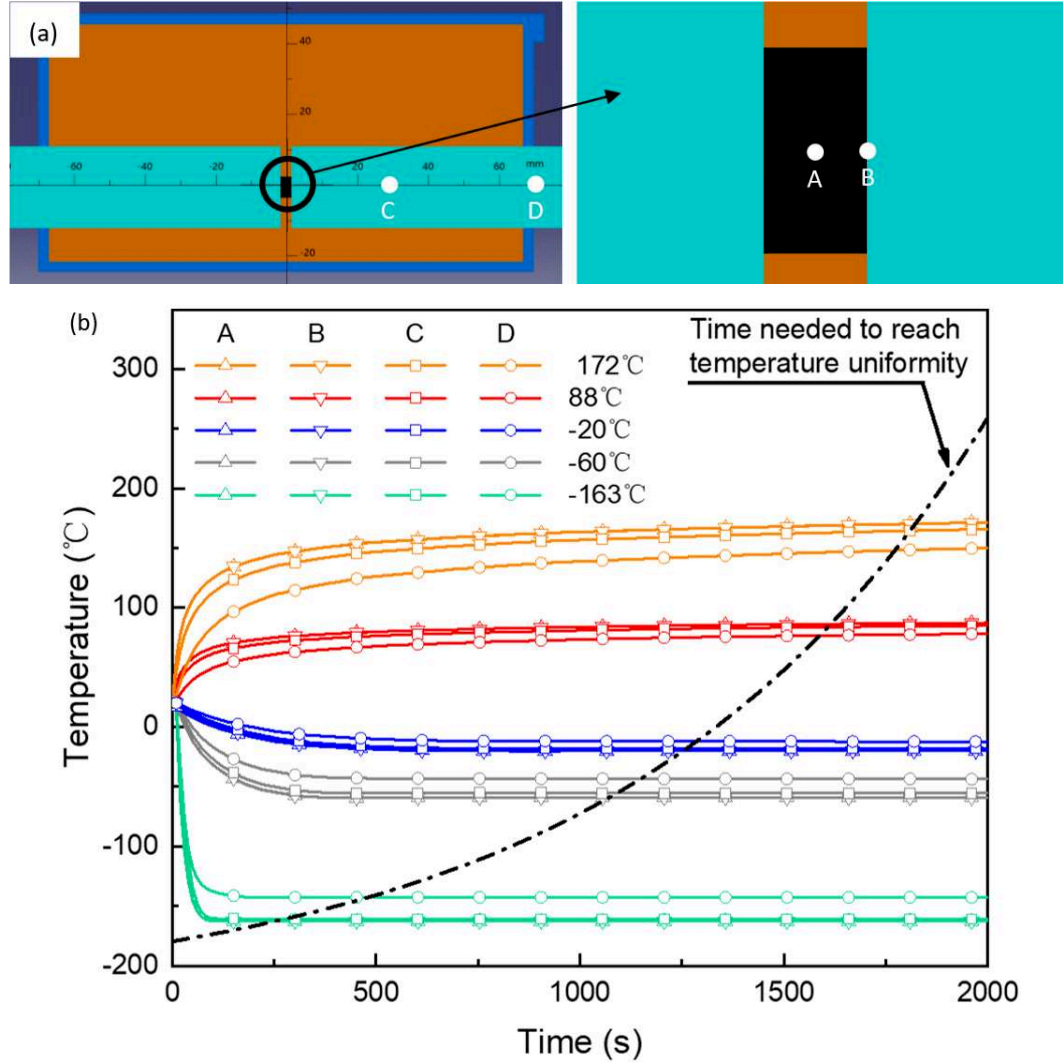
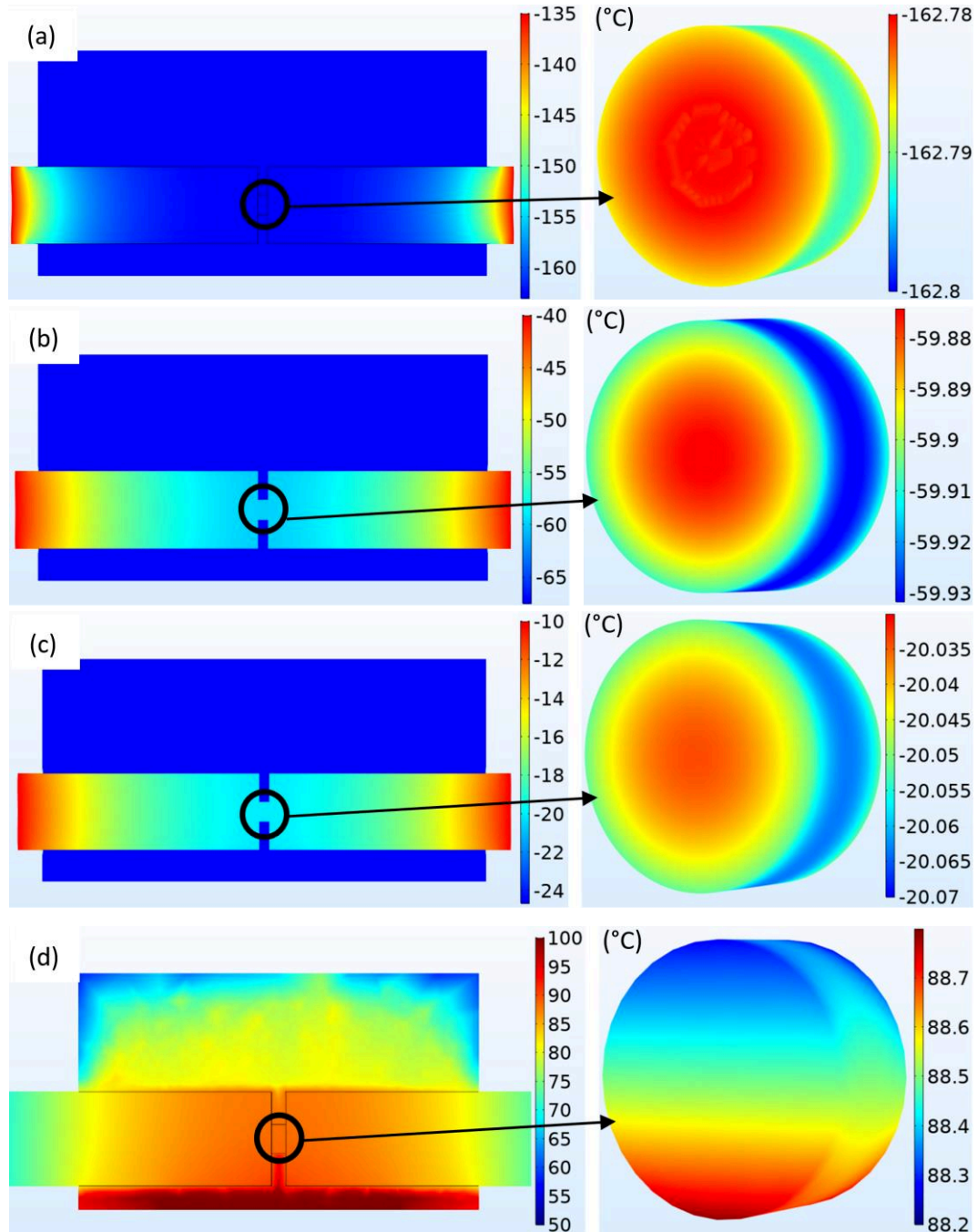


Fig. 2.5. Temperature measurement positions (a) and temperature evolution of the four positions.

According to Fig. 2.5, the temperature along the four positions in the heating furnace/cooling device is stable after a waiting time of 2000 s. The temperature distribution inside the heating furnace/cooling device at 2000 s is shown in Fig. 2.6: as shown in Fig. 2.6 (a), (b) and (c), although a strong temperature gradient forms

along the SHPB bars and at the interface between the cooling device and the air environment, the temperature distribution within the compression specimen is uniform with a maximum temperature difference of 0.05°C . For testing at elevated temperatures, as shown in Fig 2.6 (d) and (e), a temperature gradient is observed from the bottom to the top of the heating furnace, but temperature distribution inside the compression specimen is pretty uniform with a maximum fluctuation of 1.2°C .



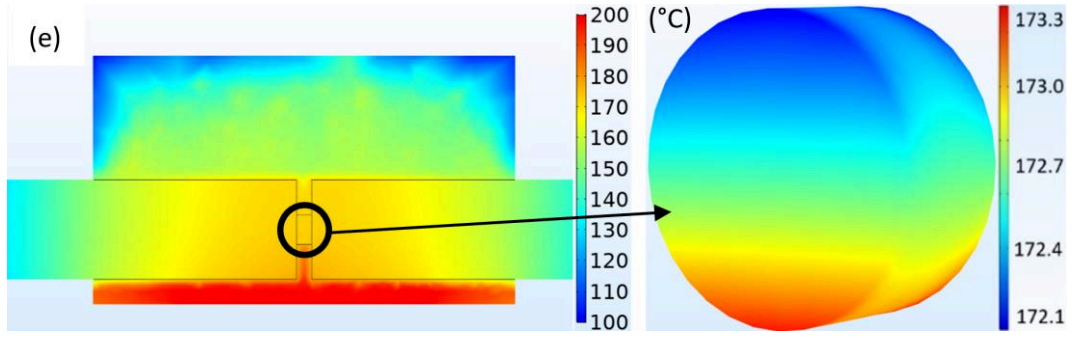


Fig. 2.6. Temperature distribution inside the heating furnace/cooling device with the specimen temperature stable at: (a) -163°C, (b) -60°C, (c) -20°C, (d) 88°C, (e) 172°C.

According to the temperature distribution analysis, the new heating furnace/cooling device works well for temperatures ranging from -163°C to 172°C. Temperature uniformity is achieved within the compression specimen with a maximum fluctuation of 1.2°C. In the next section, compression tests of 304 ASS at different strain rates and temperatures are conducted and the results are presented.

4. Experimental results and discussion

4.1 True stress-true strain relations of 304 ASS

The typical wave signals from a dynamic compression test at a strain rate of 1564 s^{-1} and an initial temperature of 172°C are shown in Fig. 2.7 (a). In order to obtain an accurate measurement of the deformation behavior of materials using the SHPB system, force equilibrium state within the specimen is necessary. To evaluate the force equilibrium state on the two end faces of the specimen, Ravichandran and Subhash proposed a parameter, $R(t)$, as below:

$$R(t) = \left| \frac{\Delta F(t)}{F_{avg}(t)} \right| = 2 \left| \frac{F_1(t) - F_2(t)}{F_1(t) + F_2(t)} \right| \quad \text{Eq. 2.5}$$

where $F_1(t)$ and $F_2(t)$ are the two forces acting on the end faces of the

compression specimen, respectively. They are calculated as $F_1(t) = EA(\varepsilon_I(t) + \varepsilon_R(t))$ and $F_2(t) = EA\varepsilon_T(t)$, where E and A are Young's modulus and the cross-sectional area of the bars, respectively. $\Delta F(t)$ and $F_{avg}(t)$ are the difference and the average of the two forces, respectively. A force equilibrium state is achieved when $R(t)$ is close to 0.

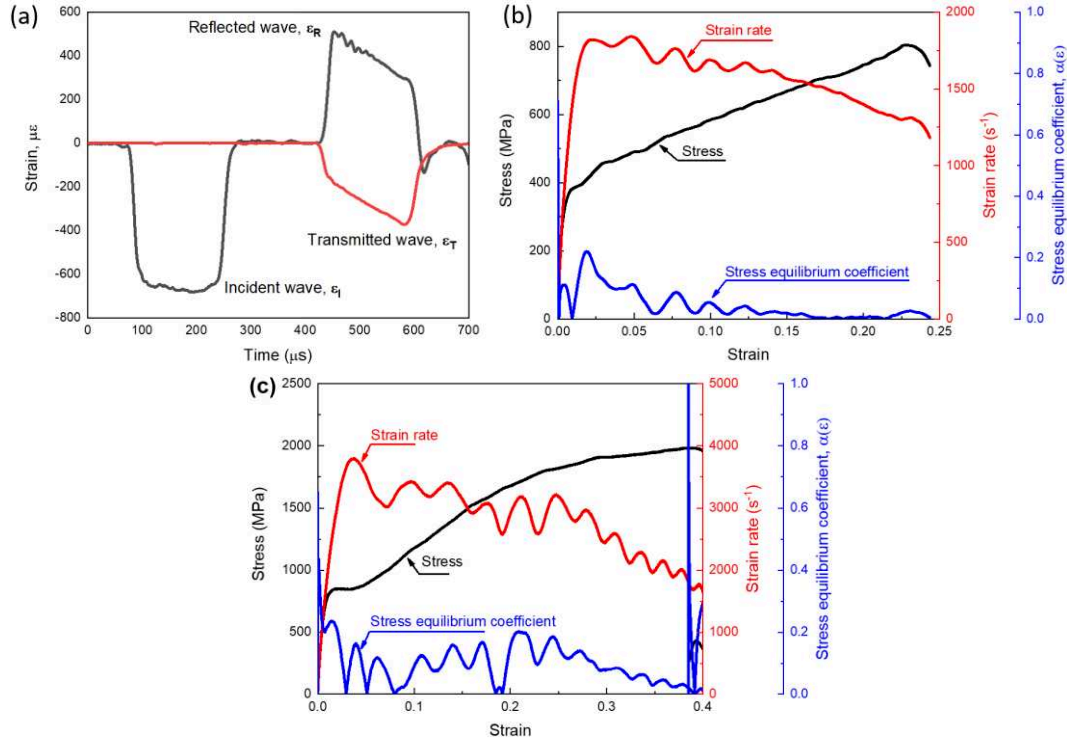


Fig. 2.7. (a) The typical strain wave signals of a dynamic compression test at strain rate of 1564 s^{-1} and temperature of 172°C . The true stress, strain rate and stress equilibrium coefficient vs true strain curves at (b) 172°C and (c) -163°C .

Based on experimental results in Fig. 2.7 (a), the variation of true stress, strain rate and force equilibrium coefficient with true strain is calculated and shown in Fig. 2.7 (b). It can be seen that $R(t)$ is always lower than 0.1 except a fluctuation at a true strain of 0.02. Concerning force equilibrium state at low temperatures, it is shown in Fig. 2.7 (c). It is seen that the condition is similar to that at 172°C . Therefore, force equilibrium is achieved inside the specimen from the very beginning of the test and maintains up to the maximum strain. The verified dynamic

force equilibrium condition ensures that the measured stress-strain curves give an accurate deformation behavior description of 304 ASS.

The true stress-true strain curves of 304 ASS for temperatures between -163°C and 172°C and strain rates between 10^{-3} s^{-1} and 3950 s^{-1} are shown in Fig. 2.8. It can be seen that for all the tested strain rates and temperatures, the flow stresses increase continuously with increasing strain but the strain hardening rates differ. In quasi-static tests (10^{-3} s^{-1} - 1 s^{-1}) conducted at 172°C , the strain hardening rate decreases slowly with increasing strain; as the testing temperature decreases to 88°C , the stress increases almost linearly with a constant strain hardening rate; with further decrease of the initial temperature, the stress-strain curves exhibit an S-shape and a second hardening phenomenon becomes obvious. This phenomenon is also observed by several other authors [9-12] in TRIP steel and is attributed to the SIMT effect. In temperature regime below M_d , which is 140°C for the tested material, martensitic transformation is triggered by plastic deformation. A mixture of martensite and austenite phases is much harder than that of pure austenite phase. Therefore, the corresponding strain hardening rate is enhanced. At 172°C , a temperature above M_d , the deformation mechanism of 304 ASS changes into dislocation glide: the strain hardening rate is controlled by a competition between dislocation generation and annihilation. Therefore, similar to many kinds of alloys, small strain hardening rate at large strains is observed. Concerning dynamic tests (1262 s^{-1} - 3950 s^{-1}) at various initial temperatures, the results are shown in Fig. 2.8 (e), (f) and (g). It is seen that the second hardening phenomenon is not obvious anymore as martensitic transformation is strongly inhibited by the adiabatic heating effect.

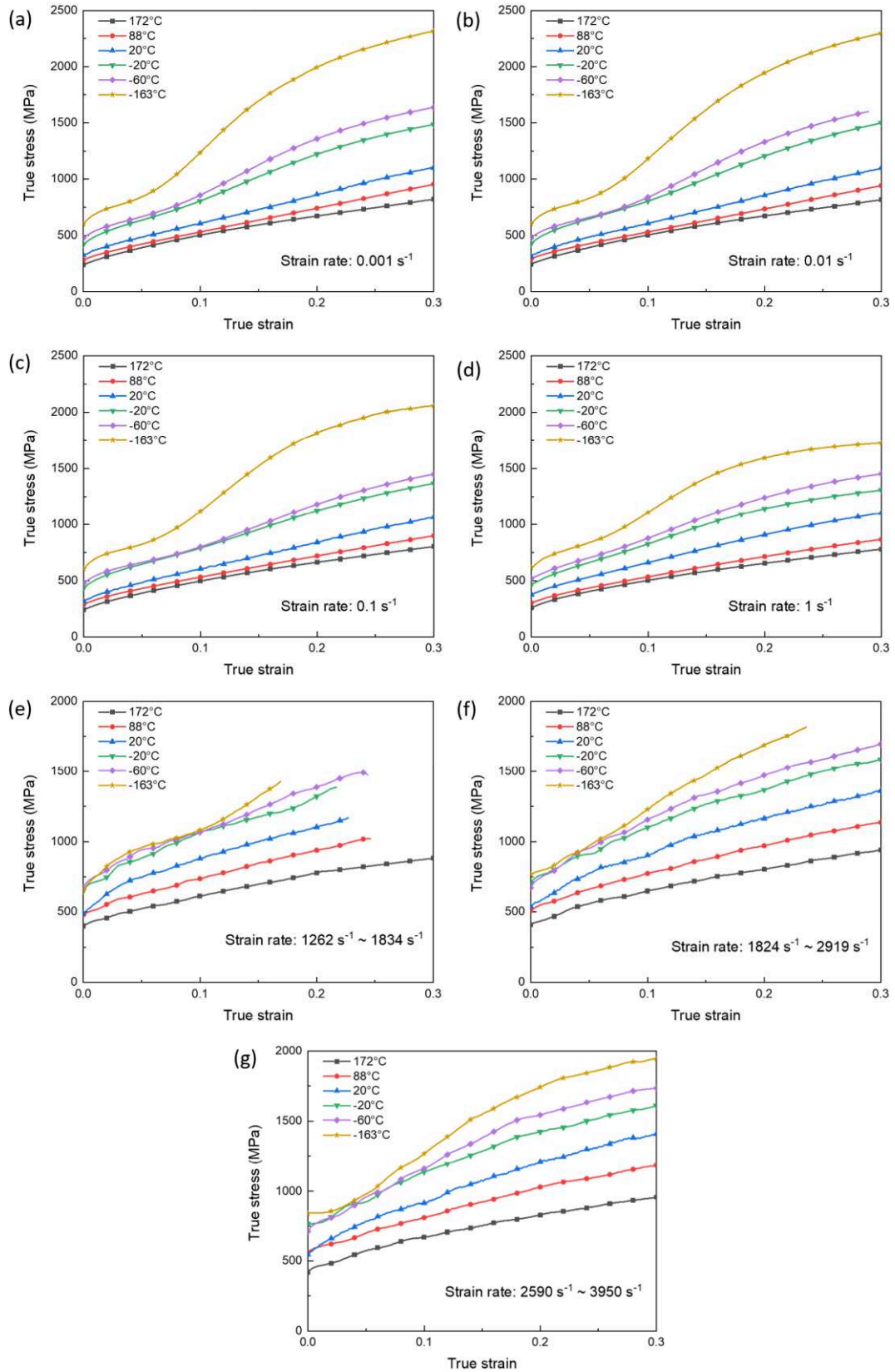


Fig. 2.8. True stress-true strain relations of 304 ASS as a function of temperature at strain rates of: (a) 10^{-3} s^{-1} , (b) 10^{-2} s^{-1} , (c) 10^{-1} s^{-1} , (d) 1 s^{-1} , (e) $1262 \text{ s}^{-1} - 1834 \text{ s}^{-1}$,

(f) 1824 s^{-1} - 2919 s^{-1} and (g) 2590 s^{-1} - 3950 s^{-1} .

The true stress-true strain curves in Fig. 2.8 show that the material is strongly influenced by both the strain rate and the temperature. To further study the effects of strain, strain rate and temperature on the deformation behavior of 304 ASS, strain rate and temperature sensitivity of the 304 ASS will be analyzed in the next section.

4.2 Strain rate and temperature sensitivity of 304 ASS

The variation of flow stress with strain rate as a function of temperature at true strains of 0.05 and 0.2, representing respectively the composite deformation behavior of pure austenite phase and a mixture of austenite and martensite phase, is plotted in Fig. 2.9. As shown in Fig. 2.9 (a), the variation of flow stress of 304 ASS with strain rate at true strain of 0.05 is consistent with metallic materials deformed by dislocation glide: the flow stress first remains constant in the quasi-static strain rates (10^{-3} s^{-1} - 1 s^{-1}) and then increases continuously with increasing strain rates in the dynamic strain rates regime (1262 s^{-1} - 3950 s^{-1}). A phenomenon should be noticed: in dynamic strain rate regime, the strain rate sensitivity is coupled with temperature. Although the flow stress is higher at lower temperatures, it increases more slowly than that at high temperatures. For thermo-viscoplastic behavior modelling, an item describing the coupled relationship between strain rate and temperature such as the Arrhenius equation is needed.

The evolution of flow stress of 304 ASS with strain rate at a true strain of 0.2 is shown in Fig. 2.9 (b). In the quasi-static strain rates range, the situation is different from that at true strain of 0.05. For temperatures below -20°C , the flow stress decreases with increasing strain rate: a negative strain rate sensitivity is observed. In particular, at -163°C , the flow stress at true strain of 0.2 is even higher than that under dynamic strain rates. The negative strain rate sensitivity is caused by the strong martensitic transformation at quasi-static strain rates while this effect is suppressed

by the adiabatic heating effect at elevated strain rates. For temperatures above 20°C, the flow stress does not change much with increasing strain rate. In the dynamic strain rate regime, a positive strain rate sensitivity similar to that at true strain of 0.05 is observed. But the strain rate sensitivity is more pronounced at low temperatures instead of previously observed high temperatures.

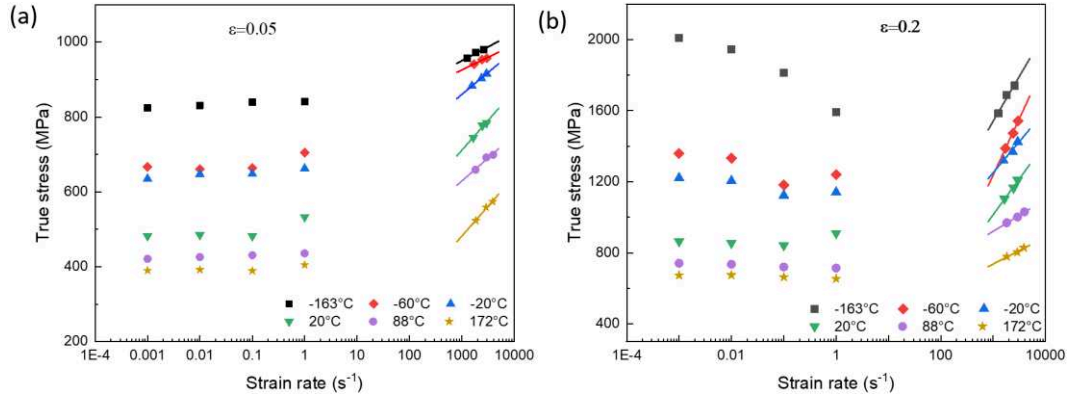


Fig. 2.9. Variation of flow stress with strain rate as a function of temperature at true strains of: (a) 0.05 and (b) 0.2.

Fig. 2.10 shows the evolution of flow stress with temperature at different strain rates and two strains. As shown in Fig. 2.10 (a), the flow stress decreases with increasing temperatures: the decreasing tendency is around 1.40 MPa/°C and 1.74 MPa/°C for static and dynamic strain rates, respectively. However, from -60°C to -163°C, the dynamic flow stress increases merely 20 MPa, the strong temperatures sensitivity disappeared. A similar phenomenon has been observed in HSLA-65 steel by Nemat-Nasser and Guo [13] when the compression behavior was studied under a wide range of strain rates and temperatures. According to the thermally activated dislocation motion theory [14], the total flow stress can be divided into two terms called the internal stress σ_μ and the effective stress σ^* , describing respectively the strain hardening effect and the thermal activation process, Fig. 2.11. The internal stress σ_μ is independent of strain rate and keeps almost constant at different temperatures, while the effective stress σ^* is strongly affected by the coupling effects of strain rate and temperature. During quasi-static (10^{-3} s^{-1} to 1 s^{-1}) tests at

various temperatures, σ^* first remains null and then increases significantly at temperatures lower than around $0.1 T_m$ (T_m refers to the melting temperature of alloys and is 1300°C for 304 ASS). For this reason, a flow stress increase is observed during tests from -60°C ($0.13 T_m$) to -163°C ($0.06 T_m$). When the strain rate changes from quasi-static to dynamic (1550 s^{-1} to 3270 s^{-1}), the effective stress σ^* increases continuously but the stress difference between different temperatures becomes smaller. Therefore, the previous observed strong temperature sensitivity almost vanished in dynamic tests.

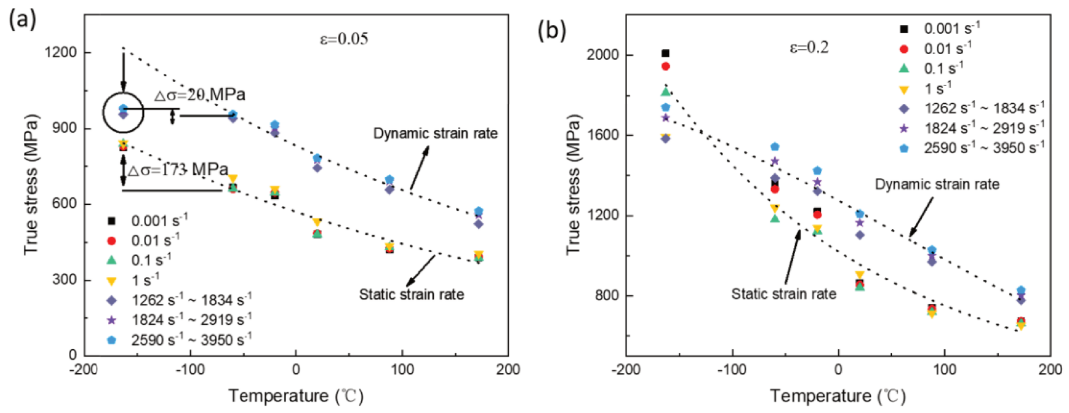


Fig. 2.10. Variation of flow stress with temperature as a function of strain rate at true strains of: (a) 0.05 and (b) 0.2.

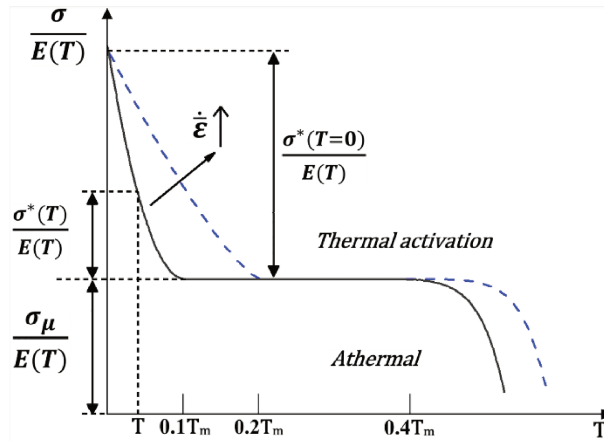


Fig. 2.11. Decomposition of the total flow stress into the internal stress σ_μ and the effective stress σ^* using the process of thermal activation [15].

Fig. 2.10 (b) shows the evolution of flow stress with temperatures at true strain of 0.2. Under the combined effect of strain rate on the transformation process and dislocation motion, the decreasing tendency of flow stress with temperature is different in static and dynamic strain rates: the flow stress decreases more slowly at dynamic strain rates than at static strain rates.

5. Thermo-viscoplastic behavior modelling of 304 ASS

Concerning constitutive behavior modeling of TRIP steels, two kinds of models are commonly used: the phenomenological and the physical based models.

The phenomenological models, such as the Johnson-Cook model, the Khan-Huang model and the Arrhenius equation, are simple to implement and have a limited number of material parameters. Hence, they are widely used for many kinds of materials under various deformation conditions. However, they have some limitations. First, the models do not have a physical basis and are commonly used for various materials with different deformation mechanism. Thus, the prediction capacities are comparatively low. Taken the Johnson-Cook model as an example, it is a simple phenomenological model made up of three items describing the strain hardening, strain rate sensitivity and temperature sensitivity of the tested material, respectively. In the model, a simple Swift type equation is used to describe the strain hardening behavior of materials. Thus, it can not be used to materials with specific deformation mechanism such as Transformation-Induced Plasticity (TRIP) steel and Twinning-Induced Plasticity (TWIP) steel, Fig. 2.12.

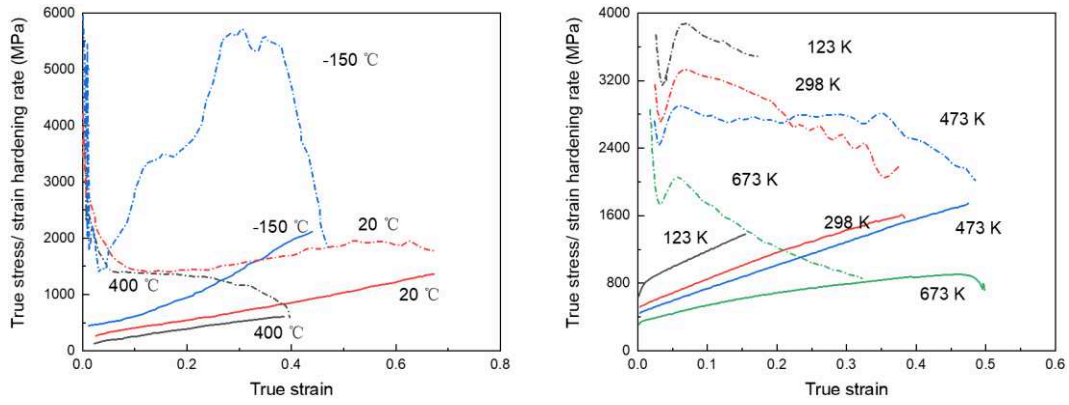


Fig. 2.12 Stress/strain hardening rate vs strain at different temperatures for (a) TRIP steel and (b) TWIP steel [16,17].

In addition, due to the simplified items to express the effects of strain rate and temperature on the strain hardening rate (by one constant), strain rate (by one constant) and temperature sensitivity (by one constant) of the tested material. The coupled influence of strain rate and temperature on the strain hardening rate, Fig. 2.13, as well as the viscous drag effect commonly encountered in extreme high strain rates, Fig. 2.14, cannot be described accurately. Concerning deformation behavior at even higher strain rates, modifications of the original JC model are normally needed [18-21].

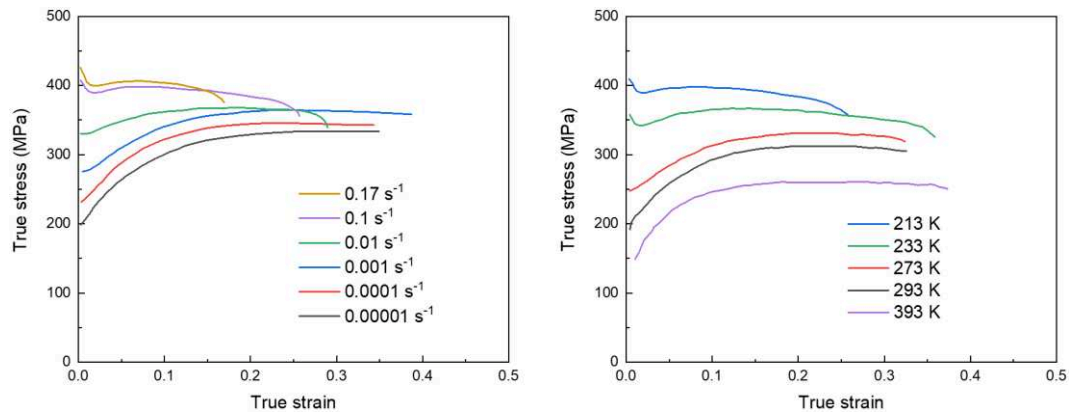


Fig. 2.13. Effects of strain rate and temperature on the strain hardening rate of mild steel [22].

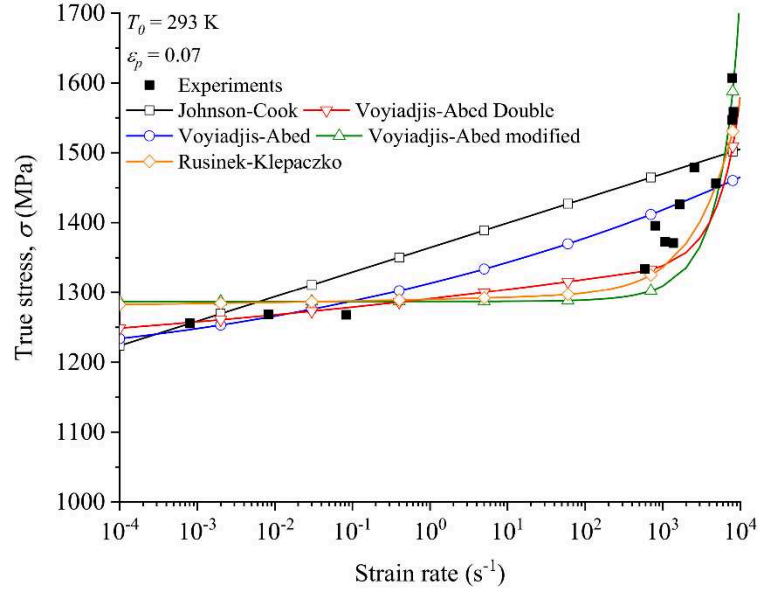


Fig. 2.14. Flow stress vs strain rate for a high strength steel at room temperature [23].

Compared to the phenomenological models, physical based models are more commonly used for constitutive behavior modelling of TRIP steel [24-26]. Mostly, a martensitic transformation model such as the O-C model and the S model is used to characterize the evolution of phase fractions; and the overall deformation behavior is described by a mixture rule using the constitutive relations of each phase. For example, the Tomita-Iwanmoto (T-I) model can be used to predict not only the deformation behavior of TRIP steel but also the evolution of phase fraction. However, an accurate phase fraction measurement is needed. In addition, the simple mixture rule cannot describe the overall constitutive relation of the tested material accurately unless the individual deformation behavior of each phase is determined effectively with respect to strain rate and temperature.

In this section, an extension of the original RK model considering phase transformation phenomenon [27] is used to describe the deformation behavior of 304 ASS. The extended RK model is a combination of the physical based RK model and a phenomenological item describing the unique martensitic transformation effect.

A typical stress-strain curve of 304 ASS at -20°C and 10^{-3} s^{-1} is shown in Fig. 2.15. The curve is divided into two parts: within a true strain of 0.08, no martensitic transformation occurs during the deformation process; at larger strains, the deformation mechanism changes into a competition between dislocation slip and martensitic transformation. The stress-strain curve without phase transformation can be extended with the same strain hardening rate. The extended curve is assumed as the flow stress of 304 ASS without martensitic transformation and can be described by the original RK model. The difference between the real and extended stress-strain curve is supposed to be caused by martensitic transformation. The corresponding flow stress can be described by an extended item coupled to the original RK model. In both steps, all the stress-strain curves under various strain rates and temperatures are fitted using the method described in Farrokh and Khan' work [29]: first, the initial values are determined following a procedure step by step; then, using a least square method, the model parameters are implemented in an optimization program to further minimize the difference between experiments and model predictions.

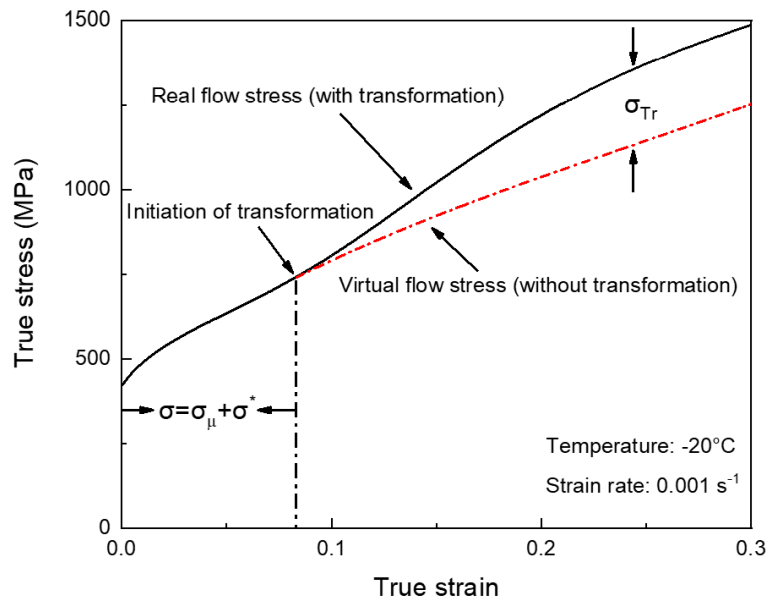


Fig. 2.15. The stress-strain curve of 304 ASS at -20°C and 10^{-3} s^{-1} .

Compared to the phenomenological models and physical based model

introduced above, the extended RK model has several advantages: first, the original RK model is a physical based constitutive model with eight material constants to be determined. It can predict the deformation behavior of materials by thermally activated dislocation motion theory accurately. Several phenomena such as the coupled strain rate and temperature's effects on the strain hardening rate and the increased strain rate sensitivity under dynamic strain rates are all captured by the model. Second, the extended item is a new stress component based on evolution of martensite phase, which takes effects of strain, strain rate and temperature into consideration. The extension is chosen to be a phenomenological equation with merely four material constants, which can be fitted easily. Moreover, the implementation of this kind of phenomenological equation into a finite element (FE) code is simple.

In addition, no phase fraction measurement is needed to define the model parameters. Various martensite fraction measurement techniques can be used but each of them has its limitations and it is pretty difficult to obtain accurate proportions of each phase:

- Metallographic observation is convenient but the results are strongly affected by sample surface preparation techniques.
- For EBSD, the severe plastic deformation makes the indexing rate decrease a lot, so the measurement results are representative only under small strains.
- The detection area of XRD is limited to the sample surface. Moreover, the diffraction results may be biased by the crystallographic texture.
- Magnetic permeability measurement is also used to calculate martensite fraction but the inverse magnetostriction cannot be avoided.

Without martensite fraction measurement, the error caused by inaccurate measurement methods can be largely avoided.

5.1 The extended R-K constitutive equation

Inspired by the thermally-activated dislocation motion theory [14], the original form of the RK model is given as a sum of two components, the internal stress $\sigma_\mu(\bar{\epsilon}^p, \dot{\epsilon}^p, T)$ and the effective stress $\sigma^*(\dot{\epsilon}^p, T)$, defining the strain hardening effect and the thermal activation process, respectively, Fig. 2.11.

$$\bar{\sigma}(\bar{\epsilon}^p, \dot{\epsilon}^p, T) = \frac{E(T)}{E_0} [\sigma_\mu(\bar{\epsilon}^p, \dot{\epsilon}^p, T) + \sigma^*(\dot{\epsilon}^p, T)] \quad \text{Eq. 2.6}$$

The two components are multiplied by a parameter $E(T)/E_0$ to represent the temperature dependence of Young's modulus,

$$\frac{E(T)}{E_0} = 1 - \frac{T}{T_m} \exp \left[\theta^* \left(1 - \frac{T_m}{T} \right) \right] \quad \text{Eq. 2.7}$$

where E_0 , T_m , θ^* are Young's modulus at 0 K, the melting temperature and the characteristic homologous temperature of the tested material, respectively.

A strain hardening equation similar to the Swift law is used to describe the internal stress $\sigma_\mu(\bar{\epsilon}^p, \dot{\epsilon}^p, T)$. Since it is commonly observed that the strain hardening of metallic materials under various strain rates and temperatures is not a constant, the plasticity modulus $B(\dot{\epsilon}^p, T)$ and the strain hardening parameter $n(\dot{\epsilon}^p, T)$ are defined to be strain rate and temperature dependent,

$$\sigma_\mu(\bar{\epsilon}^p, \dot{\epsilon}^p, T) = B(\dot{\epsilon}^p, T)(\epsilon_0 + \bar{\epsilon}^p)^{n(\dot{\epsilon}^p, T)} \quad \text{Eq. 2.8}$$

$$B(\dot{\epsilon}^p, T) = B_0 \left[\left(\frac{T}{T_m} \right) \log \left(\frac{\dot{\epsilon}_{max}}{\dot{\epsilon}^p} \right) \right]^{-v} \quad \text{Eq. 2.9}$$

$$n(\dot{\epsilon}^p, T) = \left\langle 1 - D_2 \left(\frac{T}{T_m} \right) \log \left(\frac{\dot{\epsilon}^p}{\dot{\epsilon}_{min}} \right) \right\rangle \quad \text{Eq. 2.10}$$

where ϵ_0 refers to the value corresponding to the yield point during quasi-static tests, $\dot{\epsilon}_{max}$ and $\dot{\epsilon}_{min}$ are the maximum and minimum strain rate experienced by the tested

material, respectively, B_0 and D_2 are material constants, v is the temperature sensitivity parameter and n_0 is the strain hardening parameter at 0 K. The operator $\langle x \rangle = x$ if $x > 0$; otherwise $\langle x \rangle = 0$ if $x \leq 0$.

The effective stress $\sigma^*(\dot{\epsilon}^p, T)$ defines the flow stress induced by thermal activation process using an Arrhenius equation:

$$\sigma^*(\dot{\epsilon}^p, T) = \sigma_0^* \left\langle 1 - D_1 \left(\frac{T}{T_m} \right) \log \log \left(\frac{\dot{\epsilon}_{max}}{\dot{\epsilon}^p} \right) \right\rangle^{m^*} \quad \text{Eq. 2.11}$$

where σ_0^* is the effective stress at 0 K, D_1 and m^* are material constants.

To define the stress component caused by martensitic transformation, a third term $\sigma_{Tr}(\bar{\epsilon}^p, \dot{\epsilon}^p, T)$ is coupled to the original R-K model.

$$\begin{aligned} \bar{\sigma}(\bar{\epsilon}^p, \dot{\epsilon}^p, T) &= \frac{E(T)}{E_0} [\sigma_\mu(\bar{\epsilon}^p, \dot{\epsilon}^p, T) + \sigma^*(\dot{\epsilon}^p, T)] \\ &+ \sigma_{Tr}(\bar{\epsilon}^p, \dot{\epsilon}^p, T) \end{aligned} \quad \text{Eq. 2.12}$$

$$\sigma_{Tr}(\bar{\epsilon}^p, \dot{\epsilon}^p, T) = \sigma_0^\alpha f(\bar{\epsilon}^p, \dot{\epsilon}^p) g(T) \quad \text{Eq. 2.13}$$

where σ_0^α refers to the maximum stress increase caused by martensitic transformation. The value should be obtained by mechanical tests at the lowest temperature of interest.

$f(\bar{\epsilon}^p, \dot{\epsilon}^p)$ is a phenomenological function to describe the effects of strain rate and strain on the probability of martensitic transformation. It is given as,

$$f(\bar{\epsilon}^p, \dot{\epsilon}^p) = [1 - \exp(-h(\dot{\epsilon}^p)\bar{\epsilon}^p)]^\xi \quad \text{Eq. 2.14}$$

$$h(\dot{\epsilon}^p) = \lambda_0 \exp(-\lambda \dot{\epsilon}^p) \quad \text{Eq. 2.15}$$

where ξ is a constant that defines the strain value where austenite phase starts to transform into martensite. It can be inferred from the experimentally obtained stress-strain curves, where an interrupt increase of strain hardening means the beginning of martensitic transformation. $h(\dot{\epsilon}^p)$ is a function that describes strain rate

dependent martensitic transformation; λ_0 and λ are two shape fitting parameters. A detailed description concerning the fitting results of phase transformation using $h(\dot{\varepsilon}^p)$ can be found in [2].

To define the effect of initial temperature on the transformation process, a temperature function $g(T)$ is proposed:

$$g(T) = 1 - \left(\frac{T - M_S}{M_D - M_S} \right)^n \quad \text{Eq. 2.16}$$

where M_S refers to the temperature below which the Gibbs free energy between the austenite phase and martensite phase is high enough for martensitic transformation to occur spontaneously, M_D is the temperature above which martensitic transformation does not occur anymore and the deformation mechanism changes into twinning or dislocation slip, n represents the strain rate sensitivity of the transformation process.

The determination of the constitutive parameters in the extended RK model is divided into two steps: first of all, the extended curves of 304 ASS under different strain rates and temperatures are regarded as the stress-strain curves without martensitic transformation and are then defined by the original RK model. A detailed description of the fitting procedures of the RK model can be found in [2]. After that, the stress component caused by martensitic transformation is defined by the third item σ_{Tr} of the extended RK model. In both steps, a least square method is used to minimize the error between calculated data and experimental results.

For dynamic shear tests ($\dot{\varepsilon} \geq 10 \text{ s}^{-1}$), the deformation process is regarded as 100% adiabatic and the corresponding temperature rise is estimated by Equation 2.17:

$$\Delta T(\varepsilon) = \frac{\beta}{\rho C_p} \int \sigma d\varepsilon \quad \text{Eq. 2.17}$$

where ρ is the density of the material with a value of 7.8 g/cm^3 ; β ($=0.9$) is the

Taylor-Quinney coefficient characterizing the fraction of plastic work converted into heat; C_p is the heat capacity of 304 ASS. Due to the low testing temperature encountered (77 K) in this work, C_p is not taken as a constant but is given as a function of the testing temperature instead, Fig. 2.16.

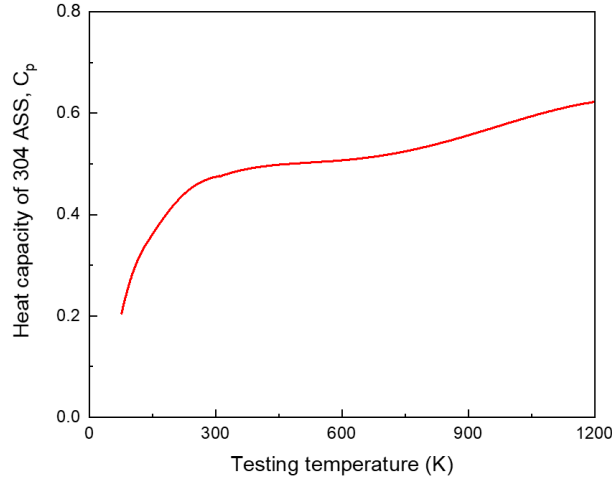


Fig. 2.16. Evolution of the specific heat of 304 ASS with the testing temperature [8].

The total number of material constants of the generalized constitutive model is 12 including 4 parameters to define the martensitic transformation effect. The fitted material parameters of the original R-K model and the extended item are shown in Table 2.2 and Table 2.3, respectively.

Table. 2.2. The fitted parameters of the original RK model for 304 ASS without martensitic transformation.

E_0 (GPa)	T_m (K)	θ^* (-)	σ_0^* (MPa)	D_1 (-)	m^* (-)
210	1700	0.9	658	0.58	1.84
B_0 (MPa)	ν (-)	n_0 (-)	D_2 (-)	ε_0 (-)	
1693	0.41	0.39	-0.19	0.023	

Table. 2.3. The fitted parameters of the extended item describing the martensitic transformation phenomenon.

σ_0 (MPa)	M_D (K)	M_S (K)	λ (-)	λ_0 (-)	ξ (-)	η (-)
1026	413	20	0.60	21.17	10.76	0.82

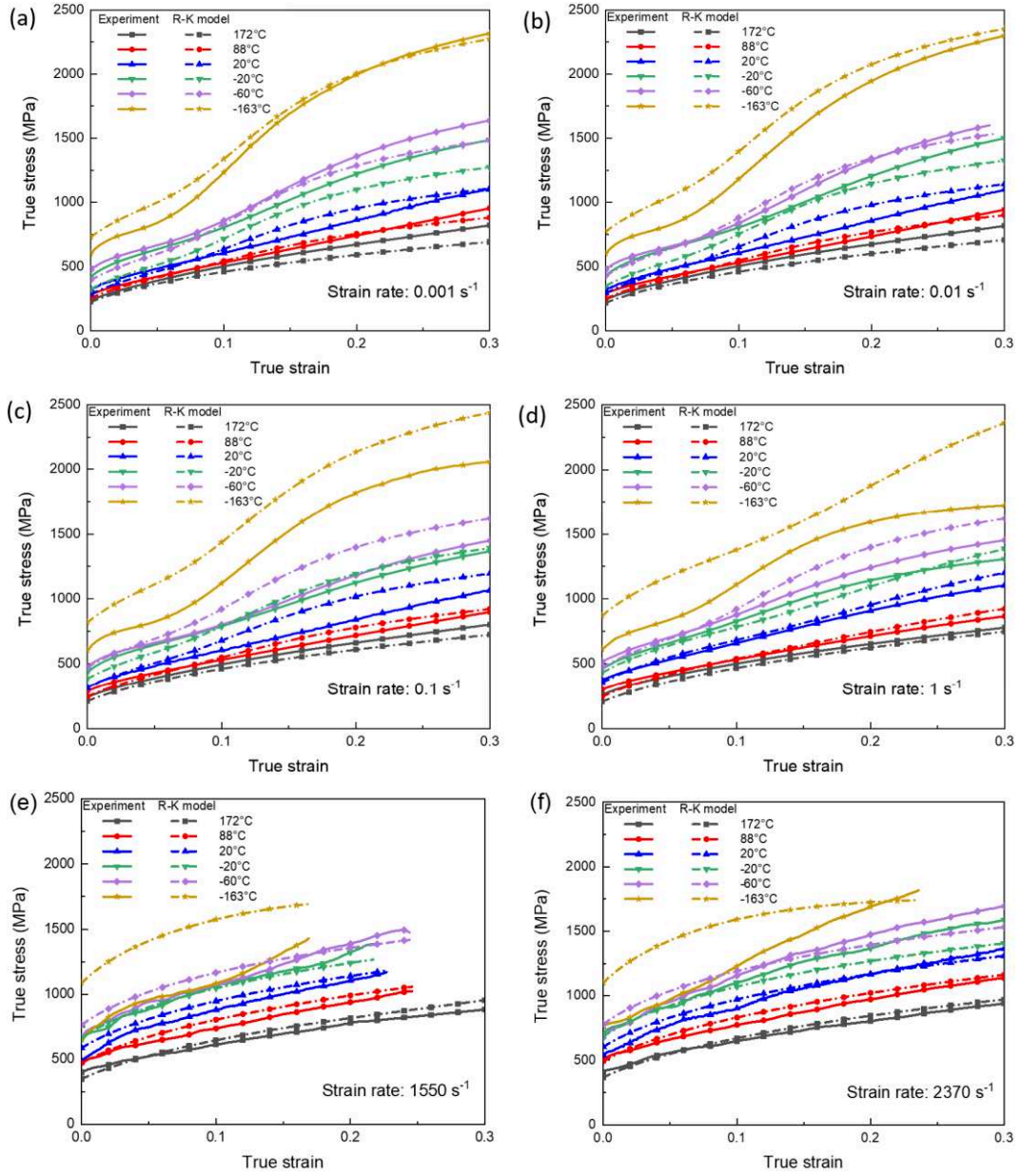
5.2 Comparison between experimental and predicted flow stress for 304 ASS

A comparison between experiments and predicted stress-strain curves using the extended R-K model of 304 ASS as well as the corresponding prediction errors are shown in Fig. 2.17 and Fig. 2.18, respectively. The prediction error Δ is used to assess the fitting result and is defined as

$$\Delta = \frac{1}{N} \sum_{i=1}^N \left| \frac{\sigma_i^{exp} - \sigma_i^{pre}}{\sigma_i^{exp}} \right| \times 100\% \quad \text{Eq. 2.18}$$

It is observed that a good agreement is achieved for initial temperatures between -60°C and 172°C. The prediction errors are respectively 7.6% and 4.9% for quasi-static and dynamic tests. According to J.A.Rodríguez-Martínez et al [28], an obvious temperature increase is still observed in TRIP steels at quasi-static tests, and it affects martensitic transformation significantly. However, in this study, the quasi-static tests are considered as isothermal for flow stress prediction. Therefore, the prediction results for quasi-static tests are not as good as the dynamic ones. In addition, due to the unexpected low strain rate sensitivity of 304 ASS at -163°C shown in Fig. 2.10, the predicted flow stress is significantly higher than the experimental ones with an average error of 21.2%. This is mainly because in the

extended RK model, a phenomenological instead of physical function is used to describe the martensitic transformation: the function works well within a limited temperature regime. However, for a better martensitic transformation behavior description, a further improvement of the extended RK model is needed.



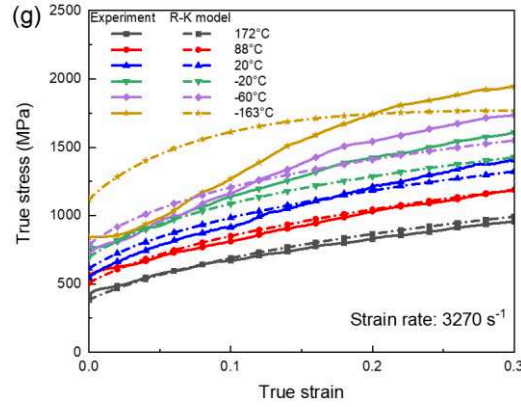


Fig. 2.17. Comparison between experimental data and RK model description for (a) 10^{-3} s^{-1} , (b) 10^{-2} s^{-1} , (c) 10^{-1} s^{-1} , (d) 1 s^{-1} , (e) 1550 s^{-1} , (f) 2370 s^{-1} and (g) 3270 s^{-1} .

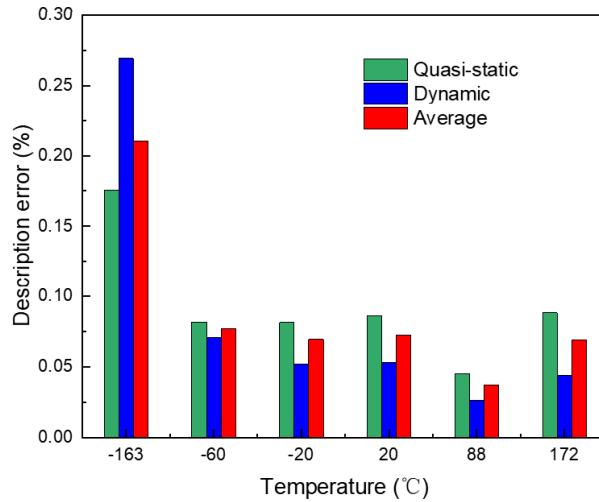


Fig. 2.18. The description error of the R-K model.

To compare the experimental data and predicted ones in more details, the evolution of flow stress with strain rate at two strains 0.05 and 0.2 are shown in Fig. 2.19. It is clear in Fig. 2.19 (a) that the extended RK model gives satisfactory predictions concerning the strain rate sensitivity at various initial temperatures except for -163°C . In the dynamic strain rate regime, the coupled relationship between strain rate and temperature is also captured by the model: the material shows higher strain rate sensitivity at elevated temperatures. In fig. 2.19 (b), the negative strain rate sensitivity in quasi-static regime is not predicted correctly by the

constitutive model. As explained before, this is because in quasi-static tests the experimentally observed temperature rise is not taken into consideration when performing constitutive behavior modeling.

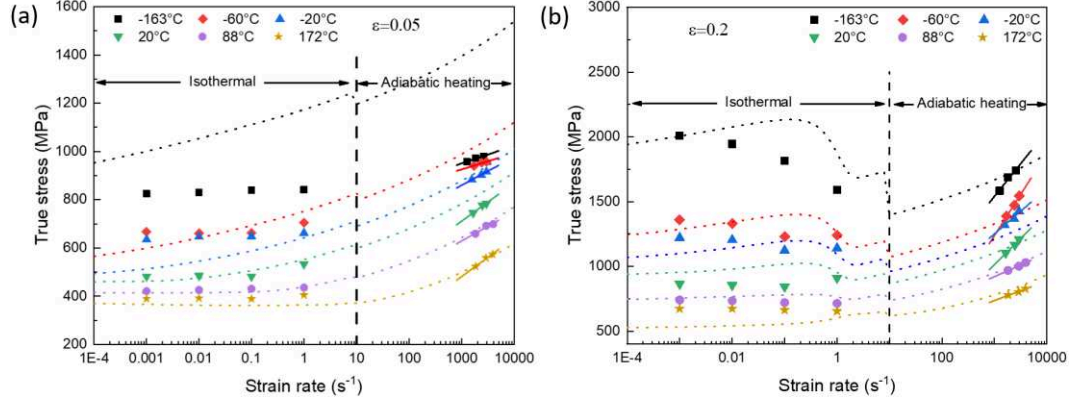


Fig. 2.19. Comparison between the experimental and the predicted results: dependence of flow stress with strain rate at true strains of: (a) 0.05 and (b) 0.2.

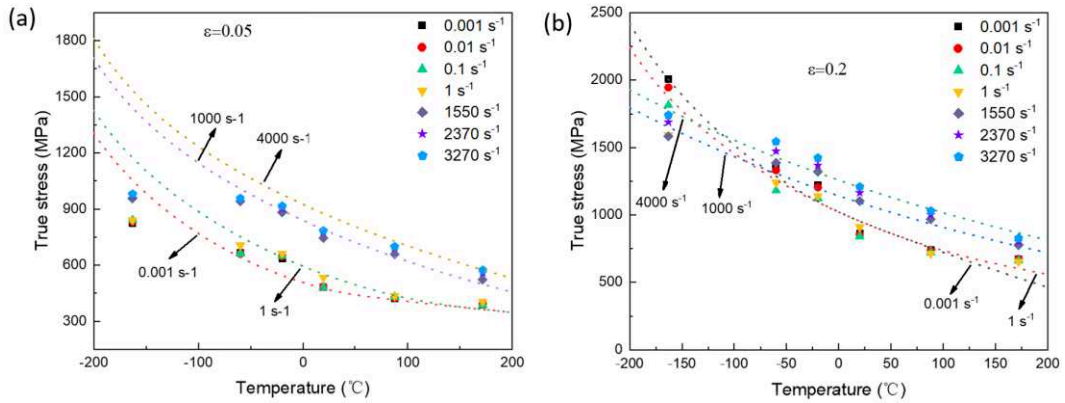


Fig. 2.20. Comparison between the experimental and the predicted results: dependence of flow stress with the temperature at true strains of: (a) 0.05 and (b) 0.2.

Concerning the temperature sensitivity prediction by the extended RK model, a comparison between experiments and the model is shown in Fig. 2.20. It is clear that the model defines the temperature sensitivity accurately between $-60^{\circ}C$ and $172^{\circ}C$. In Fig. 2.20 (b), the decreased temperature sensitivity with increasing strain rate is also captured by the extended model. On the whole, the extended R-K model

predicts the deformation behavior of 304 ASS correctly for initial temperatures $T_0 \geq -60^\circ\text{C}$.

6. Conclusion

The thermo-viscoplastic behavior of 304 ASS has been systematically studied over a wide range of strain rates, 10^{-3} s^{-1} - 3270 s^{-1} , and temperatures ranging from -163°C to 172°C . Dynamic tests at low/elevated temperatures were conducted using the Hopkinson technique coupled with a specifically designed cooling device/heating furnace, and reliability of the technique was verified by thermal simulations. The deformation behavior of 304 ASS was analyzed in terms of the strain hardening rate, strain rate sensitivity and temperature sensitivity. Based on experimental results, an extension of the RK model considering SIMT was used to describe the constitutive behavior of 304 ASS. Several noteworthy conclusions are drawn:

With the coupled cooling device/heating furnace, dynamic tests at low/elevated temperatures can be conducted by the Hopkinson technique at temperatures ranging from -163°C to 172°C . According to the numerical results, the temperature distribution within the tested specimen is uniform with a maximum temperature fluctuation of 1.2°C .

The deformation mechanism of 304 ASS is a competition between dislocation glide and martensitic transformation; strain rate and temperature both have a significant influence on the two mechanisms. Hence, the deformation behavior of 304 ASS, mainly represented by the strain hardening rate, strain rate sensitivity and temperature sensitivity, is different from metallic alloys commonly deformed by pure dislocation slip. Several unexpected phenomena such as the S-shaped stress-strain curves, the negative strain rate sensitivity and the changing temperature sensitivity from quasi-static to dynamic strain rates, are observed.

From -60°C to -163°C and under dynamic strain rates, the temperature sensitivity of 304 ASS was lower than for the other temperatures. According to the thermally activated dislocation motion theory, this is mainly caused by the comparatively smaller effective stress σ^* increase from -60°C to -163°C.

The extended RK model was used to describe the constitutive behavior of 304 ASS with an additional term linked to martensitic transformation. The model predicted the flow stress of 304 ASS above -60°C correctly with the several unexpected phenomena introduced above being captured. The prediction errors for quasi-static and dynamic tests were 7.6% and 4.9%, respectively.

References

- [1] Rusinek A, Klepaczko JR. Shear testing of a sheet steel at wide range of strain rates and a constitutive relation with strain-rate and temperature dependence of the flow stress. *International Journal of Plasticity* 2001;17:87–115. doi:10.1016/S0749-6419(00)00020-6.
- [2] Rodríguez-Martínez JA, Rusinek A, Klepaczko JR, Pęcherski RB. Extension of R–K constitutive relation to phase transformation phenomena. *Materials & Design* 2009;30:2513–20. doi:10.1016/j.matdes.2008.09.043.
- [3] Malinowski JZ, Klepaczko JR. A unified analytic and numerical approach to specimen behaviour in the Split-Hopkinson pressure bar. *International Journal of Mechanical Sciences* 1986;28:381–91. doi:10.1016/0020-7403(86)90057-3.
- [4] Moćko W, Rodríguez-Martínez JA, Kowalewski ZL, Rusinek A. Compressive Viscoplastic Response of 6082-T6 and 7075-T6 Aluminium Alloys Under Wide Range of Strain Rate at Room Temperature: Experiments and Modelling. *Strain* 2012;48:498–509. doi:10.1111/j.1475-1305.2012.00847.x.
- [5] Malinowski JZ, Klepaczko JR, Kowalewski ZL. Miniaturized Compression Test

at Very High Strain Rates by Direct Impact. *Exp Mech* 2007;47:451–63. doi:10.1007/s11340-006-9007-7.

[6] Jankowiak T, Rusinek A, Lodygowski T. Validation of the Klepaczko–Malinowski model for friction correction and recommendations on Split Hopkinson Pressure Bar. *Finite Elements in Analysis & Design* 2011;10:1191–208. doi:10.1016/j.finel.2011.05.006.

[7] Jia B, Rusinek A, Bahi S, Bernier R, Pesci R, Bendarma A. Perforation Behavior of 304 Stainless Steel Plates at Various Temperatures. *Journal of Dynamic Behavior of Materials* 2019:1–16. doi:10.1007/s40870-019-00208-9.

[8] Multiphysics C. COMSOL Multiphysics Reference Manual, Version 5.2 a. Comsol, 2015, p. 269.

[9] Hecker SS, Stout MG, Staudhammer KP, Smith JL. Effects of Strain State and Strain Rate on Deformation-Induced Transformation in 304 Stainless Steel: Part I. Magnetic Measurements and Mechanical Behavior. *MTA* 1982;13:619–26. doi:10.1007/BF02644427.

[10] Murr LE, Staudhammer KP, Hecker SS. Effects of Strain State and Strain Rate on Deformation-Induced Transformation in 304 Stainless Steel: Part II. Microstructural Study. *MTA* 1982;13:627–35. doi:10.1007/BF02644428.

[11] Talonen J, Hänninen H, Nenonen P, Pape G. Effect of strain rate on the strain-induced $\gamma \rightarrow \alpha'$ -martensite transformation and mechanical properties of austenitic stainless steels. *Metall and Mat Trans A* 2005;36:421–32. doi:10.1007/s11661-005-0313-y.

[12] Lichtenfeld JA, Van Tyne CJ, Mataya MC. Effect of strain rate on stress-strain behavior of alloy 309 and 304L austenitic stainless steel. *Metall and Mat Trans A* 2006;37:147–61. doi:10.1007/s11661-006-0160-5.

- [13] Nemat-Nasser S, Guo W-G. Thermomechanical response of HSLA-65 steel plates: experiments and modeling. *Mechanics of Materials* 2005;37:379–405. doi:10.1016/j.mechmat.2003.08.017.
- [14] Kocks UF. Thermodynamics and kinetics of slip / 1975.
- [15] Klepaczko JR, Rusinek A, Rodríguez-Martínez JA, Pęcherski RB, Arias A. Modelling of thermo-viscoplastic behaviour of DH-36 and Weldox 460-E structural steels at wide ranges of strain rates and temperatures, comparison of constitutive relations for impact problems. *Mechanics of Materials* 2009;41:599–621. doi:10.1016/j.mechmat.2008.11.004.
- [16] Masumura T, Nakada N, Tsuchiyama T, Takaki S, Koyano T, Adachi K. The difference in thermal and mechanical stabilities of austenite between carbon- and nitrogen-added metastable austenitic stainless steels. *Acta Materialia* 2015;84:330–8. doi:10.1016/j.actamat.2014.10.041.
- [17] Campbell JD, Ferguson WG. The temperature and strain-rate dependence of the shear strength of mild steel. *The Philosophical Magazine: A Journal of Theoretical Experimental and Applied Physics* 1970;21:63–82. doi:10.1080/14786437008238397.
- [18] Duffy J, Chi YC. On the measurement of local strain and temperature during the formation of adiabatic shear bands. *Materials Science and Engineering: A* 1992;157:195–210. doi:10.1016/0921-5093(92)90026-W.
- [19] Meyers MA, Xu YB, Xue Q, Pérez-Prado MT, McNelley TR. Microstructural evolution in adiabatic shear localization in stainless steel. *Acta Materialia* 2003;51:1307–25. doi:10.1016/S1359-6454(02)00526-8.
- [20] Bronkhorst CA, Cerreta EK, Xue Q, Maudlin PJ, Mason TA, Gray GT. An experimental and numerical study of the localization behavior of tantalum and stainless steel. *International Journal of Plasticity* 2006;22:1304–35.

doi:10.1016/j.ijplas.2005.10.002.

[21] Peirs J, Verleysen P, Degrieck J, Coghe F. The use of hat-shaped specimens to study the high strain rate shear behaviour of Ti–6Al–4V. *International Journal of Impact Engineering* 2010;37:703–14. doi:10.1016/j.ijimpeng.2009.08.002.

[22] Meyers MA, Staudhammer KP, Murr LE. *Metallurgical applications of shock-wave and high-strain-rate phenomena*. Dekker; 1986.

[23] Spatial evolution of adiabatic shear localization in stainless steel, titanium, and titanium-aluminum-vanadium alloy. 2002.

[24] Khan AS, Zhang H, Takacs L. Mechanical response and modeling of fully compacted nanocrystalline iron and copper. *International Journal of Plasticity* 2000;16:1459–76. doi:10.1016/S0749-6419(00)00023-1.

[25] Shi FF, Merle R, Hou B, Liu JG, Li YL, Zhao H. A critical analysis of plane shear tests under quasi-static and impact loading. *International Journal of Impact Engineering* 2014;74:107–19. doi:10.1016/j.ijimpeng.2014.06.012.

[26] Harding J, Huddart J. The use of the double-notch shear test in determining the mechanical properties of uranium at very high rates of strain. *Mechanical Properties at High Rates of Strain*, 1979 1980.

[27] Guo Y, Li Y. A Novel Approach to Testing the Dynamic Shear Response of Ti–6Al–4V. *Acta Mech Solida Sin* 2012;25:299–311. doi:10.1016/S0894-9166(12)60027-5.

[28] Rodríguez-Martínez JA, Pesci R, Rusinek A. Experimental study on the martensitic transformation in AISI 304 steel sheets subjected to tension under wide ranges of strain rate at room temperature. *Materials Science and Engineering: A* 2011;528:5974–82. doi:10.1016/j.msea.2011.04.030.

[29] Farrokh B, Khan AS. Grain size, strain rate, and temperature dependence of

flow stress in ultra-fine grained and nanocrystalline Cu and Al: Synthesis, experiment, and constitutive modeling. *International Journal of Plasticity* 2009;25:715–32. <https://doi.org/10.1016/j.ijplas.2008.08.001>.

Chapter 3 A new shear testing technique for extreme high strain rates

1. Introduction

Dynamic shear deformation and failure are present in many engineering applications such as metal forming and machining, car crashworthiness and ballistic impact. Therefore, over the last decades, the mechanical properties of metallic alloys have been investigated intensively by shear testing. According to the literature review in Chapter 1, two questions are frequently encountered in dynamic shear tests. First, how to obtain a pure shear stress state inside specimen shear zones. Mechanical properties of materials are strongly influenced by stress state. A pure shear stress state is particularly important for shear deformation and failure behavior study. However, limited by specimen dimensions, a shear-compression or shear tension stress state is often obtained [1-3]. Second, how to determine shear stress-shear strain relationship of materials accurately. Dynamic shear specimens are commonly designed for two purposes: microstructure and failure behavior study such the hat shape specimen and quantitative assessment of the specimen's stress-strain response. Compared to the former one, the later one is more difficult. If the stress state inside specimen shear zones is not pure shear or the stress components distribution is inhomogeneous [4,5], it is difficult to extract the real shear stress-shear strain behavior of materials from globally obtained force-displacement data.

In this chapter, a new shear specimen geometry is designed and validated for dynamic shear testing of bulk materials using the conventional SHPB system. First, the newly designed shear specimen and the corresponding shear testing technique are introduced. Then, this method is used to test the shear behavior of 304 ASS and the preliminary experimental results are analyzed. In the third section, the validation of the new shear specimen including the experimentally extracted shear stress-shear strain relationship and the stress state distribution inside specimen shear zones is conducted by finite element analysis (FEA). In the fourth section, the shear behavior of 304 ASS under strain rates from 0.001 s^{-1} to 39000 s^{-1} and temperatures from

77 K to 473 K are presented and analyzed. Finally, the main conclusions are summarized in section 5.

2. The new shear specimen

For a well-designed shear specimen, the following requirements should be fulfilled:

- 1) A pure shear stress state inside specimen shear zones. Stress state can be represented by the parameter stress triaxiality η which is defined as the ratio of the hydrostatic stress σ_m to the von Mises stress $\bar{\sigma}$ as follows:

$$\eta = \frac{\sigma_m}{\bar{\sigma}} = \frac{\sqrt{2}(\sigma_1 + \sigma_2 + \sigma_3)}{3\sqrt{(\sigma_1 - \sigma_2)^2 + (\sigma_2 - \sigma_3)^2 + (\sigma_3 - \sigma_1)^2}} \quad \text{Eq. 3.1}$$

$$\mu = \frac{(2\sigma_2 - \sigma_1 - \sigma_3)}{\sigma_1 - \sigma_3} \quad \text{Eq. 3.2}$$

where σ_1 , σ_2 and σ_3 are the three principal stresses with $\sigma_1 \geq \sigma_2 \geq \sigma_3$. Values of η are 1/3, 0 and -1/3 for uniaxial tension, pure shear and uniaxial compression stress state, respectively.

- 2) Homogeneous stress and strain distribution inside the specimen shear zone.
- 3) A straightforward relationship between the experimentally obtained force-displacement curves and the real shear stress-shear strain behavior of materials.

In order to adopt the new shear specimen to the conventional SHPB system for dynamic shear behavior study, two other requirements are imposed:

- 4) Achieving a force equilibrium state within the specimen from the initial stage of plastic deformation.
- 5) No use of clamping system or screws to fix the specimen on the SHPB bars.

A newly designed single shear specimen (SSS) which meets the requirements mentioned above is shown in Fig. 3.1: it is a cylinder 17 mm in height and 10 mm in diameter. Two “L” shaped symmetric slots are machined with the shear zone located between them. The SSS specimen is designed to be a whole without any clamping grips, fixtures or screws as they may cause signal oscillation during strain wave propagation process and introduce unpredictable errors into the deformation data measurement. The top and bottom surfaces of the SSS specimen are in contact with the conventional SHPB bars directly. The height and width of the shear zone, represented by H and L, are designed to be 1.5 and 1.0 mm, respectively. The width L can be reduced to 0.5 and 0.3 mm to obtain higher strain rates (the corresponding specimen height H is also reduced to 15.5 mm and 12 mm to achieve force equilibrium state more quickly). In the connection areas between the shear zone and the support parts, fillets with a radius of 0.1 mm are machined to reduce stress concentration. All the specimen dimensions are optimized according to numerical simulations by ABAQUS/Explicit. For example, if the shear zone width is too large it becomes difficult to obtain extremely high strain rates above 10^4 s^{-1} ; if it is too small, the specimen is deformed without the force equilibrium state.

It should be emphasized that the SSS specimen is designed to be single shear zone without additional clamping system, so the specimen can move freely in the lateral direction. Hence, the tension or compression components commonly encountered in double shear specimens due to their constraint lateral movement [6] can be largely avoided, and the actual stress state in specimen shear zones is pretty close to pure shear.

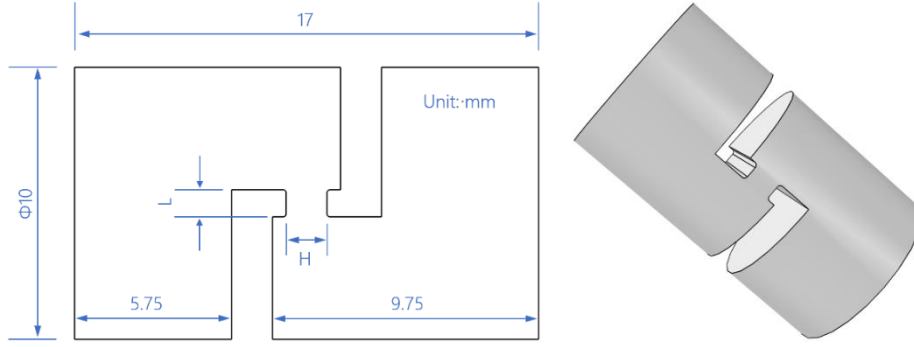


Fig. 3.1. Schematic diagram of the SSS specimen.

3. Preliminary experimental results

Dynamic shear tests of 304 ASS under nominal shear strain rates ranging from 3000 s^{-1} to 45000 s^{-1} at room temperature were carried out using a conventional SHPB system. SSS specimens with different shear zone width L were used for various strain rate regimes: $L = 1 \text{ mm}$ for $\dot{\gamma}_{nominal} \leq 15000 \text{ s}^{-1}$; $L = 0.5 \text{ mm}$ for $15000 \text{ s}^{-1} \leq \dot{\gamma}_{nominal} \leq 30000 \text{ s}^{-1}$; $L = 0.3 \text{ mm}$ for $30000 \text{ s}^{-1} \leq \dot{\gamma}_{nominal}$. The typical strain wave signals measured from one test at $\dot{\gamma}_{nominal} = 6000 \text{ s}^{-1}$ are shown in Fig. 3.2. It is seen that at $424 \text{ }\mu\text{s}$, part of the incident signal begins to transfer into the shear specimen, forming the transmitted signal. After that, the transmitted signal increases continuously while the reflected signal keeps almost constant. At $542 \text{ }\mu\text{s}$, the transmitted signal starts to decrease, indicating damage initiation and growth in the specimen shear zone. Finally, specimen fractures at $588 \text{ }\mu\text{s}$, and at the same time the reflected signal reaches the maximum value.

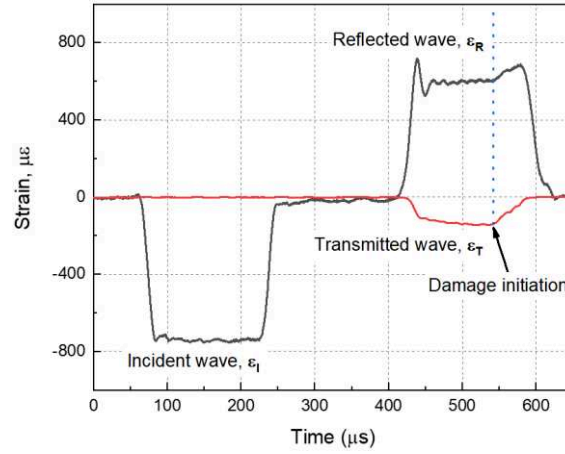


Fig. 3.2. The typical strain wave signals measured in SHPB bars.

According to the strain wave signals in Fig. 3.2, the two forces acting on the end faces of SSS specimen, F_{in} and F_{out} , are calculated and shown in Fig. 3.3. In addition, the parameter R is calculated by Eq. 1.53 to validate the force equilibrium state. It is seen from Fig. 3.3 that at the initial stage of deformation, due to the cross-section mismatch between the incident bar and the SSS specimen a strong signal oscillation is observed in F_{in} , and parameter R deviates obviously from zero. Hence, no force equilibrium state is achieved within the initial 45 μs . After that, the two forces are reasonably close to each other and parameter R is always smaller than 0.1, indicating a force equilibrium state within the SSS specimen.

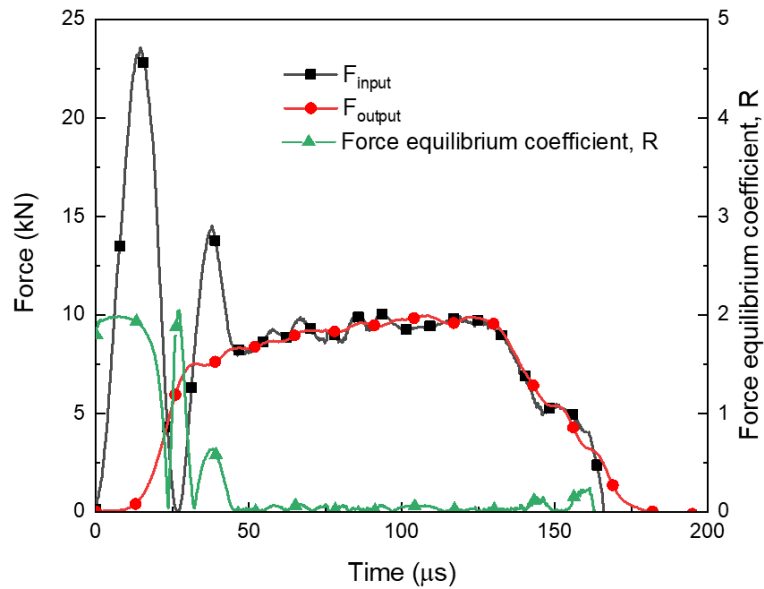


Fig. 3.3. Evolution of F_{in} , F_{out} and force equilibrium coefficient R with time.

According to Eq. 1.54, 1.55 and 1.56, the nominal shear stress-shear strain curve and the corresponding shear strain rate are calculated and shown in Fig. 3.4. The yield stress of 304 ASS is measured to be 485 MPa; after yield point, the flow stress increases continuously with an average strain hardening rate of 318 MPa/Unit strain. Damage initiates at $\gamma_{nominal}=0.66$ and then develops quickly; finally, specimen fracture was observed at $\gamma_{nominal}=1.05$. During the whole plastic deformation process, the nominal shear strain rate keeps constant at $\dot{\gamma}(t)_{nominal}=6000 \text{ s}^{-1}$. One thing that should be noticed is the experimentally measured shear modulus is 6.0 GPa, merely 8.5% of the actual value 70 GPa. Two reasons are supposed to be responsible for the difference: first, according to Fig. 3.3, no force equilibrium state is achieved during the initial elastic deformation stage. Second, the shear stress-shear strain curve is calculated based on the dimensions of the specimen shear zone, while elastic deformation of areas outside the specimen shear zone is neglected. Therefore, errors are introduced in the experimentally obtained shear stress-shear strain curves. This phenomenon will be further analyzed by finite element (FE) simulations in section 4.

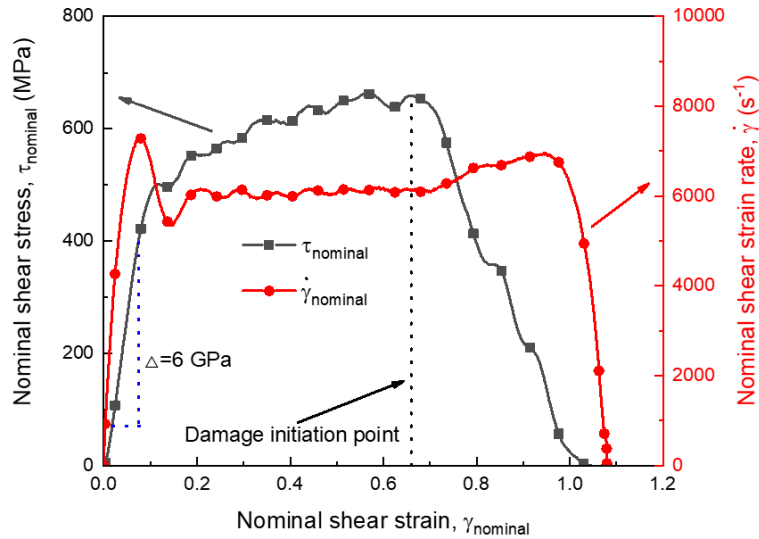


Fig. 3.4. The nominal shear stress/shear strain rate vs the nominal shear strain curves.

To check the repeatability of SSS specimens, three tests were performed under

the same conditions. The resulting nominal shear stress-nominal shear strain curves are shown in Fig. 3.5. It is seen that the three curves match each other well, even during the elastic deformation and the damage propagation period. Therefore, the new shear technique including both the SSS specimen and the SHPB method has a good reliability. The original and tested SSS specimens are shown in Fig. 3.6.

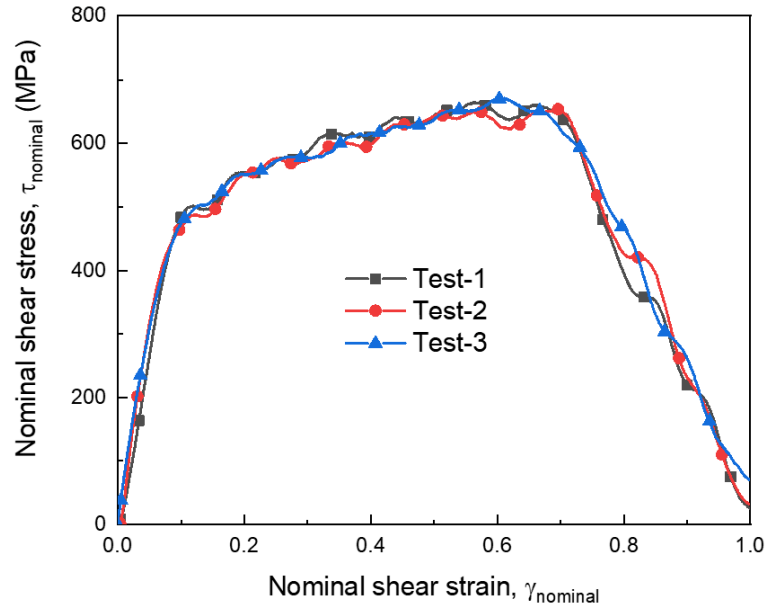


Fig. 3.5. The nominal shear stress-nominal shear strain curves of three tests conducted under the same conditions.



Fig. 3.6. The SSS specimens before and after tests at a nominal shear strain rate of 6000 s^{-1} .

4. Numerical analysis of the new shear specimen

4.1 Validity of the pulse signals in dynamic shear tests

To validate the new shear specimen and the corresponding SHPB technique, numerical simulations of dynamic shear tests have been performed using software ABAQUS/Explicit. A 3D full size finite element (FE) model consisting of the incident bar, the SSS specimen and the transmitted bar has been built, Fig. 3.7. To reduce calculation time, the projectile is not included in the model. Instead, the experimentally obtained force was applied on the left end face of the incident bar. The bar/specimen interfaces are assumed to be in frictional contact with a coefficient of 0.1, a value commonly used for lubricated steels [7].

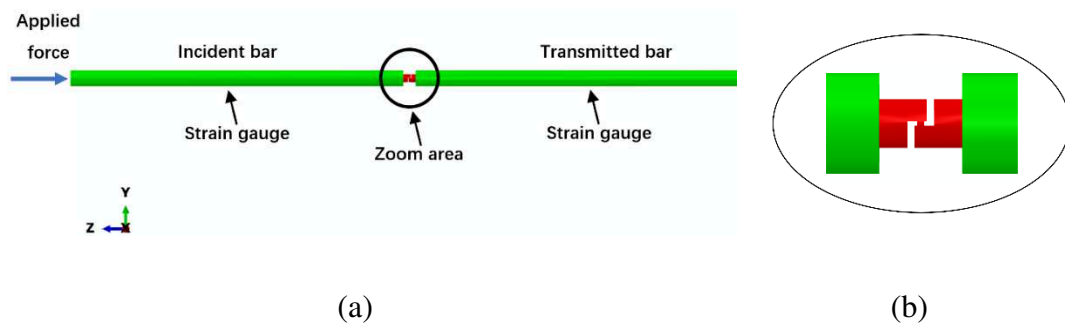


Fig. 3.7. The model assembly used for numerical simulations: (a) the assembly, (b) magnification of SSS specimen.

The FE meshes of the SHPB bars and the SSS specimen are shown in Fig. 3.8. The 8-node linear brick, reduced integration element (C3D8R) is selected for the SHPB bars, while the complete integration coupled with temperature element (C3D8T) is selected for the SSS specimen. To reduce calculation time, different mesh sizes were used for various parts of the model. Near the bar/specimen interface, a finer mesh of the SHPB bars is used to ensure good contact between them. The

minimum element size is 0.03 mm in specimen shear zone. The element numbers are 156210 and 139046 for the SHPB bars and the SSS specimen, respectively.

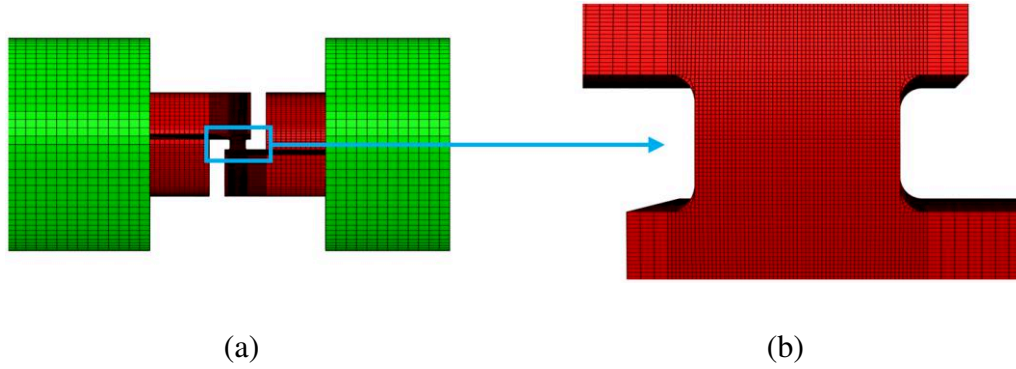


Fig. 3.8. The FE meshes in the model: (a) the end parts of the SHPB bars and the SSS specimen, (b) magnification of the refined meshes in the specimen shear zone.

The material parameters used in the numerical simulations are shown in Table. 3.1. The SHPB bars are regarded as elastic bodies. As for the SSS specimen, the nominal shear stress-nominal shear strain curve shown in Fig 3.4 is used as the input model to Abaqus. No failure behavior is considered.

Table. 3.1. Material parameters used in the numerical simulations.

Part	ρ (kg/m ³)	E (GPa)	μ	Thermal conductivity (W/m·°C)	Specific heat (J/kg·°C)
specimen	7.8	210	0.3	16.2	500
SHPB bars	8.2	210	0.3	25.3	450

A comparison between the experimentally obtained strain pulses and the simulated ones at $\dot{\gamma}(t)_{nominal}=6000 \text{ s}^{-1}$ is shown in Fig. 3.9. During numerical simulations, the strain pulses are obtained at exactly the same positions as the strain gauges in experiments. It can be seen that within the initial 200 μs , the incident and

reflected signals agree well with the experimental ones. At around 200 μs , specimen failure occurs but the failure process is not considered in numerical simulations. Hence, the experimental and simulated signals separate from each other. Concerning the transmitted signal, an average difference of 4.2% exists between the experimental and numerical ones, indicating an inaccuracy of the constitutive model. This point will be further analyzed in the following parts.

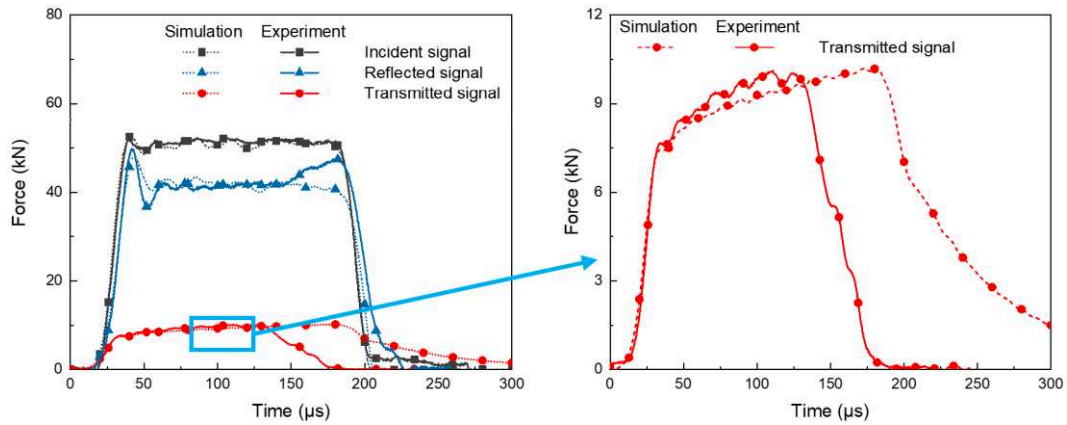


Fig. 3.9. Comparison between the experimental and numerical force wave signals.

Force equilibrium state in the specimen is also analyzed according to the numerical results. The forces-time curves acting on the two end faces of the specimen and a magnification of the initial rising up stage are shown in Fig. 3.10 (a) and (b), respectively. It is seen from Fig. 3.10 (a) that the two curves coincide with each other and force equilibrium is obtained during the whole deformation process. However, according to Fig. 3.10 (b) a time delay of around 5 μs exists between the two curves. This is the time needed for the stress wave to travel from the top to the bottom of the specimen. Compared to the whole deformation duration of 118 μs , the value is significantly smaller and hence can be neglected. However, for tests at extreme high strain rates such as 60000 s^{-1} , the effect of rising up time on testing results will be obvious. According to a study by Davies and Hunter, at least three reverberations inside the specimen is needed to achieve force equilibrium [8]. Hence, for dynamic tests using the SSS specimen, a deformation duration of more than 30

μs is needed to ensure validity of experimental results.

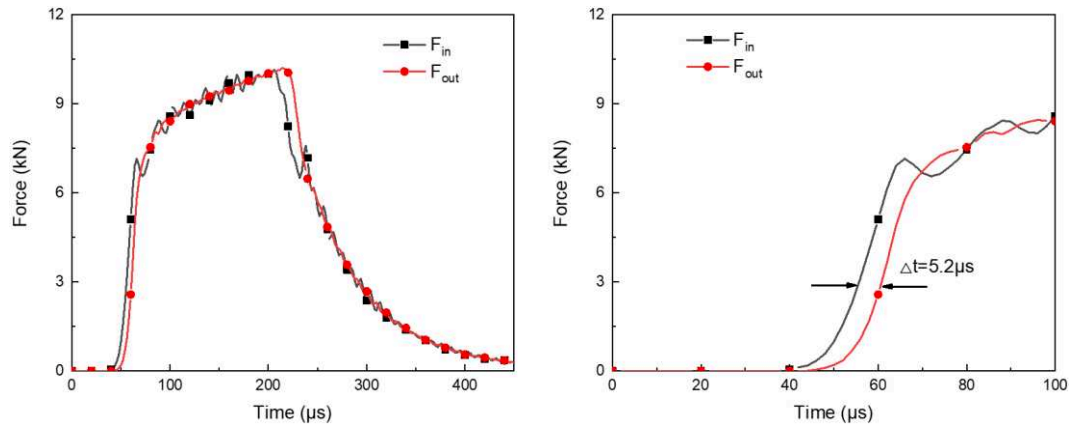


Fig. 3.10. Comparison of the two forces acting on the specimen/bar interfaces.

In order to obtain a pure shear stress state inside the specimen shear zone, the SSS specimen is designed to be non-axisymmetric. According to a study of Tian and Hu [9], eccentric deformation of specimens using the SHPB system [3,10,11] may generate bending waves, thus leading to distortion of reflected and transmitted signals by superposition of the bending waves. Therefore, based on the numerical results, the distribution of the strain pulses in the transmitted bar is analyzed. As is shown in Fig. 3.11, five positions are selected on the cross-section of the transmitted bar. Line AB is parallel to the thickness direction of the specimen shear zone and passes through the center point E of the incident bar, while line CD is perpendicular to line AB. In Fig. 3.12 (a), it is seen that at the specimen/bar interface, a strong signal is observed at position E while the signals at the other positions are obviously weaker, remaining near zero. With the stress wave propagation, signals at different positions interact with each other and the difference between the five positions decreases continuously. It is seen from Fig. 3.12 (b) that at 0.5 m away from the specimen/bar interface, signals at positions A, B and E become coincident. However, disturbed and complementary signals are observed at positions C and D, with the average value coincides with positions A, B and E. Hence, the influence of bending waves could be eliminated efficiently by mounting strain gauges in series. In

addition, by extending length of the transmitted bar from 1.5 m to 3 m in numerical simulations, the signals of the five positions at 1 m and 1.5 m away from the specimen/bar interface are shown in Fig. 3.12 (b). It is observed that beyond 1.5 m the strain pulse pulses at different positions totally overlap. Hence, another method to remove the bending waves is mounting strain gauges far away from the specimen/bar interface. During the dynamic shear tests in our study, the transmitted signals were recorded by strain gauges in series 0.75 m away from the specimen/bar interface. Therefore, the experimentally obtained signals are valid.

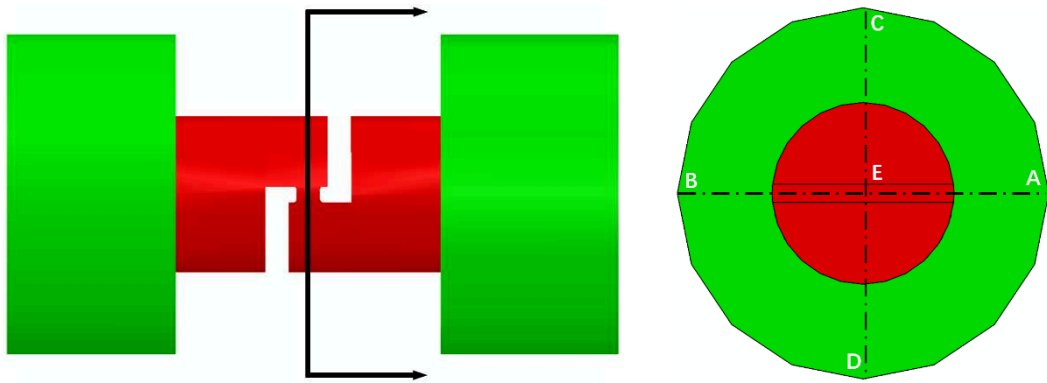


Fig. 3.11. Schematic presentation of the selected positions for stress signal measurement.

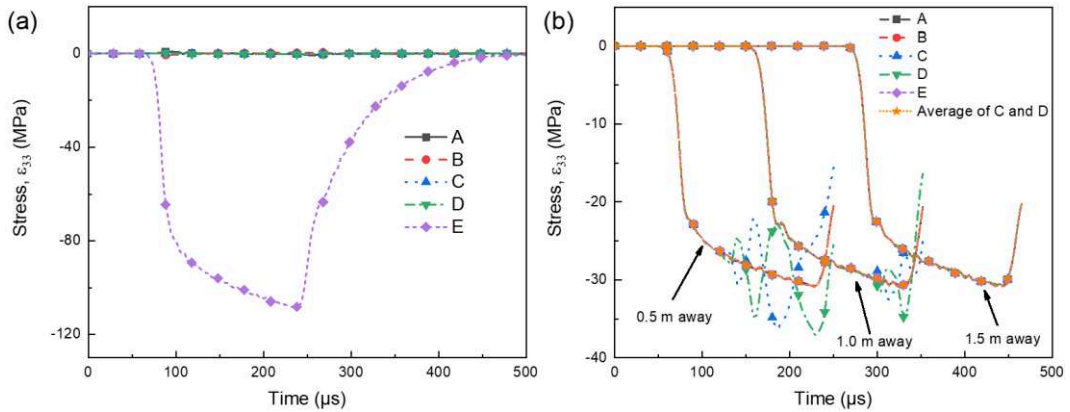


Fig. 3.12. The transmitted stress signals at different positions on the bar: (a) at the specimen/bar interface and (b) at 0.5, 1.0 and 1.5 mm away from the specimen/bar interface.

In addition, a comparison between the integrated force at the bar/specimen interface and at the strain gauge position is shown in Fig. 3.13. It can be seen that the forces at the two positions are the same, except that the former one has more and irregular oscillations. Hence, during stress wave propagation, the integrated force remains unchanged and represents the actual force acting on the bar/specimen interface.

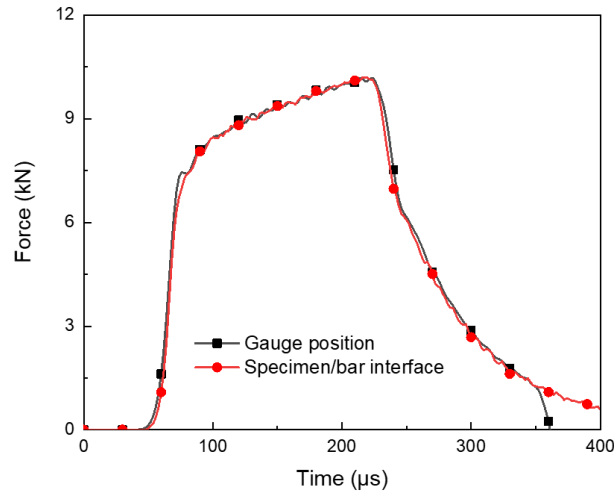


Fig. 3.13. Comparison between the force measured at the specimen/bar interface and the gauge position.

4.2 Analysis of stress state in specimen shear zone

According to the numerical results, the stress state in the specimen shear zone is analyzed. The average stress and logarithmic strain components of the whole specimen shear zone as a function of the nominal shear strain are shown in Fig. 3.14 (a) and (b), respectively. It is seen from Fig. 3.14 that during the whole deformation process the specimen shear zone is dominated by the shear stress component σ_{13} and the shear strain component ϵ_{13} . In Fig. 3.14 (a), with increasing nominal shear strain, normal stress components σ_{22} and σ_{33} increases continuously, while shear stress components σ_{12} and σ_{23} remain at zero. The evolution of stress components in the SSS specimen is similar to that in the double shear specimen (DSS) developed

by Xu [12]. However, different from the DSS, stress component σ_{11} of SSS specimen increases slightly first and then remains constant at large strains. This is because no clamping device is used to fix the specimen and the specimen shear zone can move freely in the lateral direction. Hence, the strong tension component σ_{11} at large strains, which is often observed in classical double shear specimens, does not exist in SSS specimen. In Fig. 3.14 (b), the evolution of strain components is similar to that of stress components. Shear strain component ϵ_{13} is always significantly larger than ϵ_{11} and ϵ_{33} , while the other components maintain at zero. In fact, at nominal shear strain of 0.66, the strain corresponding to damage initiation point during experiments, the absolute values of ϵ_{13} , ϵ_{11} and ϵ_{33} are -0.38, -0.07 and 0.07, respectively. According to stress/strain components analysis above, deformation process of the SSS specimen is dominated by shear components σ_{13} and ϵ_{13} with the others being comparatively lower; stress state inside specimen shear zone can be regarded as plane shear.

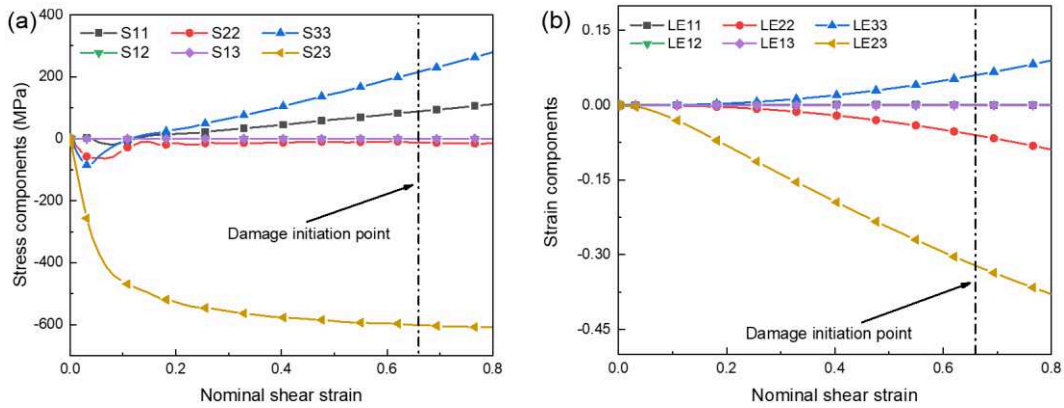


Fig. 3.14. Evolution of average stress and strain components in specimen shear zone: (a) stress components and (b) strain components.

Fig. 3.15 shows the distribution of von Mises stress on the central x-y and y-z planes of the shear zone at nominal shear strains of 0.66. It is seen that von Mises stress distributes uniformly in most areas of the specimen shear zone, except the upper and bottom free surface where a stress gradient from 600 MPa to 1300 MPa is observed. From the shear zone to the other parts of the specimen, however, a

strong stress gradient is observed. In addition, stress concentration is observed at four corners of the shear zone. Distribution of equivalent plastic strain at nominal shear strains of 0.66 is shown in Fig. 3.16. Plastic deformation is limited in the specimen shear zone and its distribution is pretty uniform too. At upper left and bottom right corners of the shear zone, the largest plastic deformation is observed, which indicates that the specimen may fail along diagonal of the shear zone, a phenomenon has already been observed by Meyer and Halle [13] in double shear specimens.

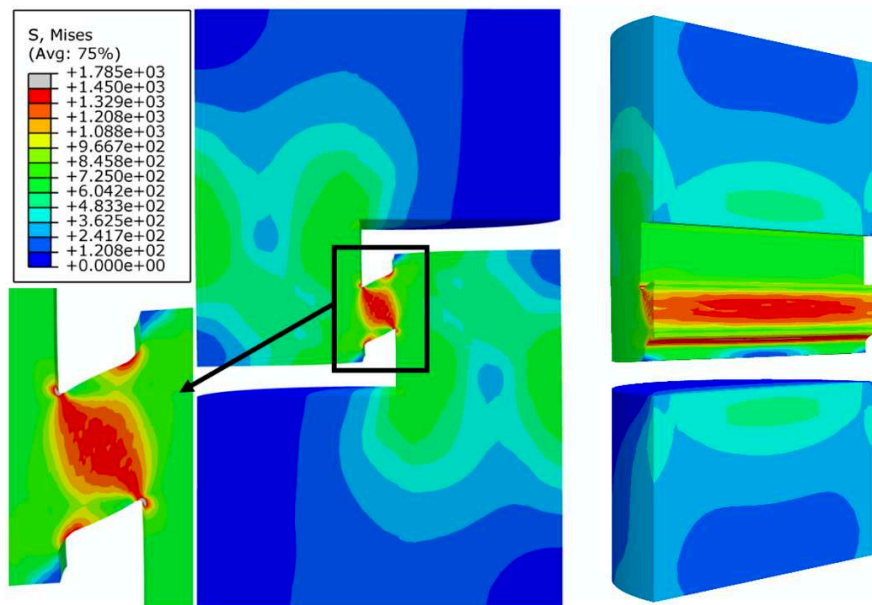


Fig. 3.15. Distribution of von Mises stress at a nominal shear strain of 0.66.

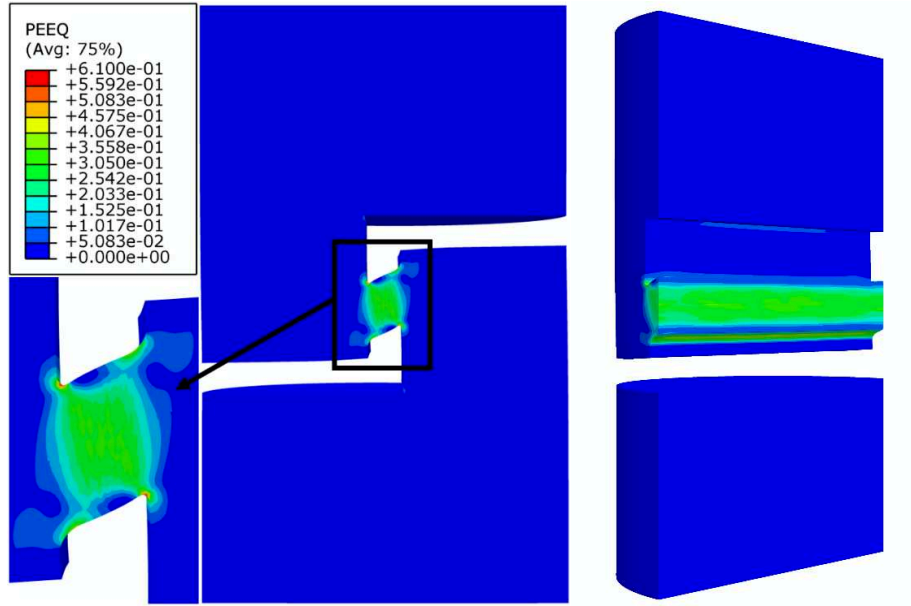


Fig. 3.16. Distribution of equivalent plastic strain at a nominal shear strain of 0.66.

The evolution of the average stress state of the whole specimen shear zone with the nominal shear strain is shown in Fig. 3.17. During the whole plastic deformation regime, the value of stress triaxiality increases continuously from -0.051 to 0.082, indicating that the corresponding stress state changes from slight shear-compression to shear-tension. The averaged stress triaxiality of the whole plastic deformation period is 0.032. Evolution of the Lode angle parameter shows an opposite trend: it decreases quickly from 0.112 to 0 first and then declines linearly until the damage initiation point, and the averaged Lode angle parameter is 0.004. According to the evolution of stress triaxiality and Lode angle parameter, the stress state in the specimen shear zone can be regarded as simple shear.

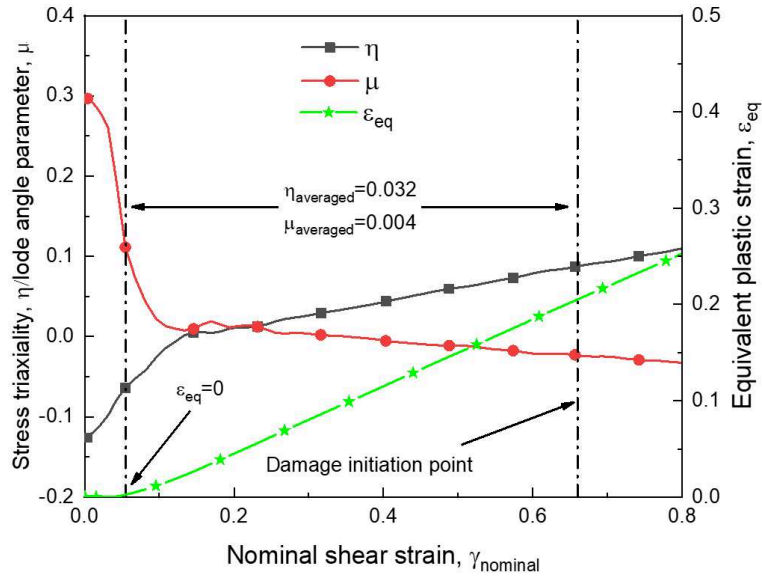


Fig. 3.17. The average stress state of the whole specimen shear zone as a function of the nominal shear strain.

Compared to the commonly used double shear specimens, the stress triaxiality and Lode angle parameter in the SSS specimen shear zones are relatively lower. This is mainly because the SSS specimen is designed to be a single shear zone without any clamping system. During shear testing by double shear specimens, a clamping device, Fig. 3.18, is commonly used to prevent specimen rotation and achieve a homogeneous stress/strain distribution. However, due to the clamping device, the lateral displacement of the specimen is constrained. As a result, more and more tension components are observed at large deformation [6]. Compared to double shear specimen, the SSS specimen is sandwiched between the Hopkinson bars without clamping device. Moreover, the end faces of the specimen are coated with the lubricant to reduce friction. Therefore, the SSS specimen can move easily in both the vertical and the lateral directions. No strong tension components are observed anymore, Fig. 3.13. This point is further verified by another numerical simulation. As shown in Fig. 3.19, a displacement restriction on two surfaces 0.3 mm away from the specimen shear zone is added: no lateral displacement is allowed on the two surfaces. The other boundary conditions are exactly the same as the model

introduced in section 4.1.

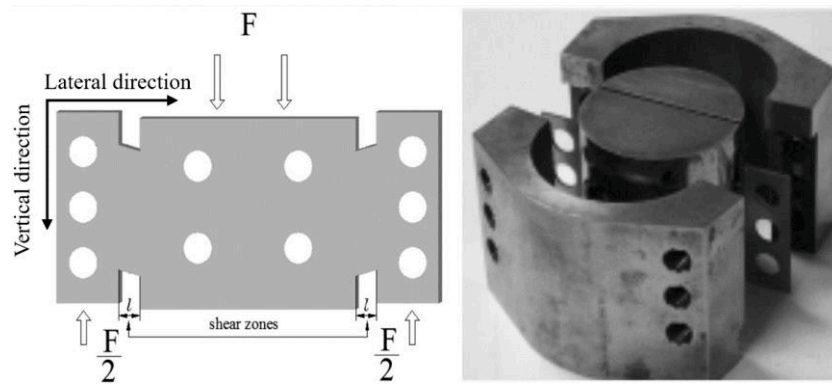


Fig. 3.18. The clamping device for double shear specimens.

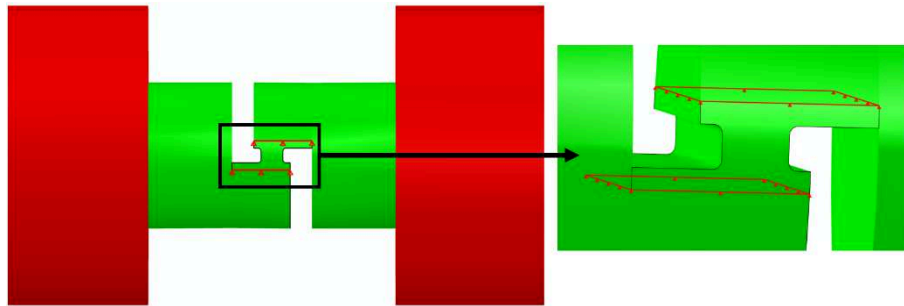


Fig. 3.19. Additional boundary conditions: displacement restriction on two surfaces 0.3 mm away from the specimen shear zone.

According to the numerical results, average stress triaxiality and Lode angle parameters of the specimen shear zone are compared to those without the displacement restriction, Fig. 3.20. It can be seen that affected by the fixed lateral displacement boundary conditions, both the stress triaxiality and the Lode angle parameter deviate obviously from pure shear. For example, compared to the previous model, at the damage initiation point, values of stress triaxiality and Lode angle parameter change from 0.082 to 1.92 and from -0.024 to -0.058, respectively. Moreover, the relative deformation along the thickness direction of the specimen shear zone is also shown in the figure. Without the additional boundary conditions, the shear zone thickness reduces from 1 mm to 0.94 mm, a 6% deformation.

However, the thickness decreases from 1 mm to 0.982 mm, merely a 1.8% deformation when the lateral displacement restriction is added to the model. Therefore, although the clamping device helps to reduce specimen distortion and achieve a uniform stress/strain distribution, it affects the stress state of the specimen shear zone. Compared to double shear specimens, the SSS specimen without any clamping device helps to achieve a stress state closer to pure shear.

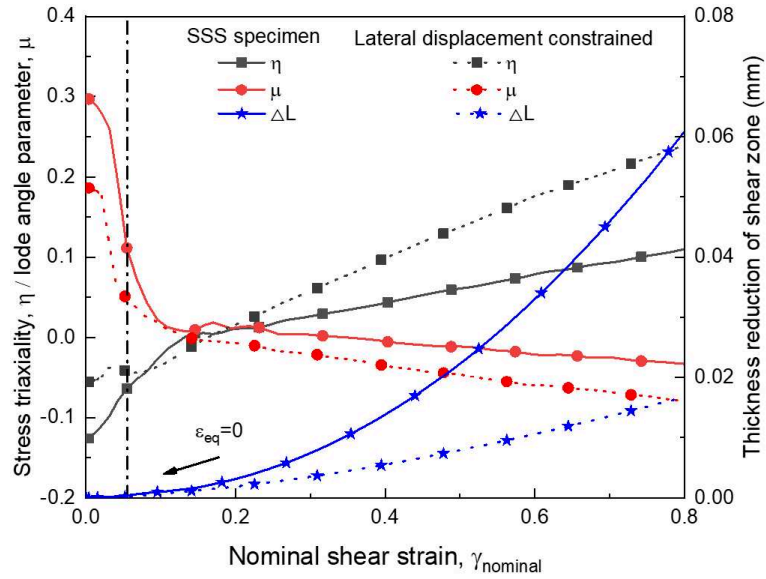


Fig. 3.20. Comparison of the average stress state of the specimen shear zone between with and without lateral displacement restriction.

4.3 Determination of shear stress-shear strain relations

One of the goals of the SSS specimen is to obtain accurate shear stress-shear strain relationships for constitutive behavior modelling. Hence, in this section, the real shear stress-shear strain behavior of the tested material is extracted from the force-displacement data and then verified through comparisons with the numerical results.

Based on the numerical results in section 4.1, a comparison between the stress-strain data of all the elements in the specimen shear zone (representing the real deformation behavior of the specimen) and the nominal shear stress-nominal shear

strain curve calculated from the force-displacement data (representing the overall response of the whole specimen) is shown in Fig. 3.21. For easy comparison, the $\tau_{\text{nominal}} - \gamma_{\text{nominal}}$ curve is transferred into the von Mises stress σ_{eq} - equivalent plastic strain ε_{eq} curve by equations.

$$\sigma_{\text{eq}} = \sqrt{3}\tau_{\text{nominal}} \quad \text{Eq. 3.2}$$

$$\varepsilon_{\text{eq}} = \frac{\gamma_{\text{nominal}}}{\sqrt{3}} \quad \text{Eq. 3.3}$$

It is seen from Fig. 3.21 that an obvious gap exists between the two curves: the calculated $\sigma_{\text{eq}} - \varepsilon_{\text{eq}}$ curve underestimates the flow stress with an averaged error of 11%. This is mainly because a pure shear stress state is assumed when transferring the $\tau_{\text{nominal}} - \gamma_{\text{nominal}}$ into $\sigma_{\text{eq}} - \varepsilon_{\text{eq}}$ curve, while the real stress state in the specimen shear zone deviates slightly from pure shear. In addition, a significant difference is observed between the two curves in the initial stage of deformation: while the yield stress of the prescribed constitutive model is around 660 MPa, flow stress of the extracted curve starts from 0 MPa. A similar phenomenon is observed by Dorogoy and Rittel in shear-compression specimen (SCS) [7]. This is caused by the stiffness exaggeration of areas outside the specimen shear zone. According to the analysis above, the experimentally obtained nominal shear stress-nominal shear strain data does not represent the real shear stress-shear strain relationship of the tested material. This explained why a slight difference exists between the experimental and numerical stress wave signals in Fig. 3.9. Hence, correction of the experimental data is necessary to obtain more accurate shear behavior of materials.

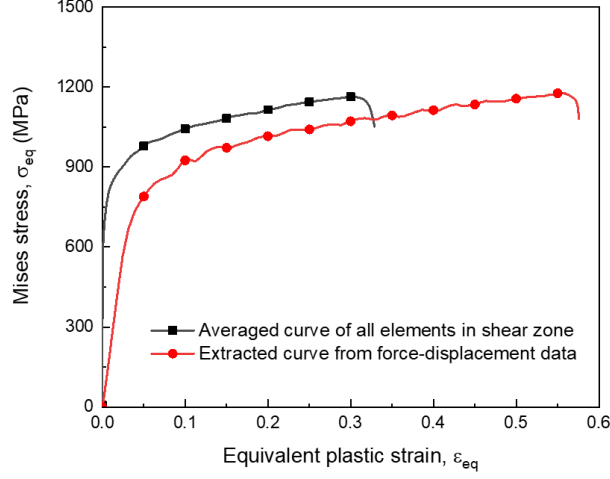


Fig. 3.21. Comparison between the average stress-strain curve of all elements in the specimen shear zone and the calculated one from the force-displacement data.

Here a corrective coefficient method used by Rusinek and Klepaczko [14] is adopted to extract the real shear stress-shear strain curves from the nominal shear stress-nominal shear strain data.

A numerical simulation of the quasi-static shear test using the SSS specimen has been conducted by Abaqus/Standard. It aims to determine the relations between the nominal shear stress ($\tau_{nominal}$)-nominal shear strain ($\gamma_{nominal}$) and the averaged shear stress (τ)-shear strain (γ) of all elements in the specimen shear zone using the following equations:

$$\gamma = \lambda_{\gamma}(\gamma_{nominal} - \gamma_{yield}) \quad \text{Eq. 3.4}$$

$$\tau = \lambda_{\tau}\tau_{nominal} \quad \text{Eq. 3.5}$$

where γ_{yield} refers to the displacement at which the SSS specimen starts to yield. Values of λ_{γ} and λ_{τ} are determined from the numerical analysis. The boundary conditions of the numerical model are shown in Fig. 3.22 (a). The model consists of a SSS specimen and a rigid plate locates on the upper surface of the specimen. A vertical downward displacement of 0.8 mm, corresponding to a nominal shear strain of 0.8, is applied on the rigid plate, while the bottom surface of the SSS specimen is

fixed. Frictional contact between the rigid plates and the specimens is assumed and a friction coefficient of 0.1 is used. The mesh of the model is shown in Fig. 3.22 (b). It consists of 118130 8-node linear brick, reduced integration elements (C3D8R) with a minimum size of 0.03 mm in the specimen shear zone.

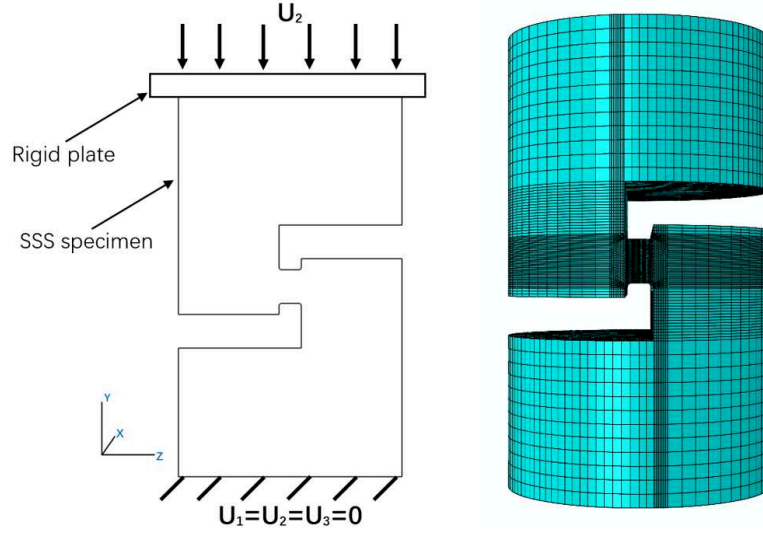


Fig. 3.22. (a) The applied boundary conditions and (b) the meshed SSS specimen.

An elastic-plastic constitutive model, as shown in Fig. 3.23, is used in the numerical simulation. The curve is derived from dynamic compression tests of 304 ASS under strain rate of 2500 s^{-1} at room temperature. The Young's modulus is $E=210 \text{ GPa}$ and Poisson's ratio $\nu=0.33$. The yield stress σ_0 was taken as 1050 MPa and the strain hardening behavior is described by the Voce type law [15] $\sigma = \sigma_0 + A(1 - e^{-C\varepsilon_p})$ with values of A and C are 888 and 3.14, respectively.

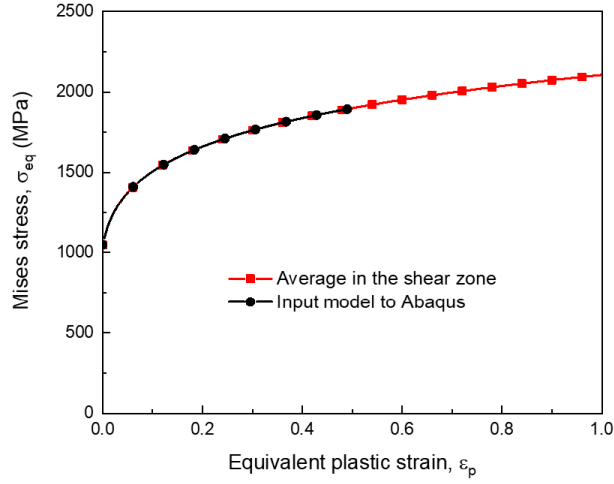


Fig. 3.23. The input constitutive model to Abaqus.

The average Mises stress versus equivalent plastic strain of all elements in the specimen shear zone is plotted in Fig. 3.23 together with the input model to Abaqus. It is seen that the average values in the specimen shear zone represent the constitutive behavior of the simulated material correctly.

Fig. 3.24 (a) shows the average shear strain in the specimen shear zone and the nominal shear strain versus the applied displacement. From the ratio between the two curves, the corrective parameter λ_γ is found to be 1.03. Fig. 3.24 (b) shows the evolution of the average shear stress in the specimen shear zone and the nominal shear stress with the applied displacement. Using a least square method, value of λ_τ is fitted to be 1.12.

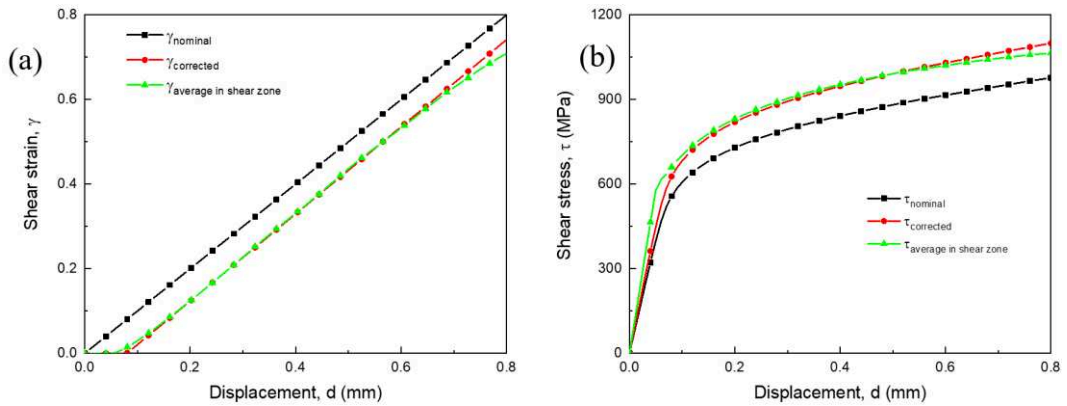


Fig. 3.24. Comparison of (a) shear strain and (b) shear stress vs displacement

before and after correction by Eq. 3.4 and 3.5.

Fig. 3.25 shows a comparison between the nominal $\tau_{nominal} - \gamma_{nominal}$, the $\tau_{corrected} - \gamma_{corrected}$ and the $\tau_{average} - \gamma_{average}$ values in the specimen shear zone. It is seen that the correction of the nominal data by three coefficients λ_γ , λ_τ and γ_{yield} leads to an increase of shear stress and a decrease of shear strain. After correction, the shear stress and shear strain data match the real deformation behavior of the tested material well. In fact, the relative errors for shear stress and shear strain data are 1.0% and 0.9%, respectively. Therefore, Eq. 3.4 and 3.5 can be used to determine the shear stress-shear strain relationship of the tested material accurately. Following the same procedure, the correction parameters for SSS specimens with different shear zone width L are calculated and shown in Table. 3.2.

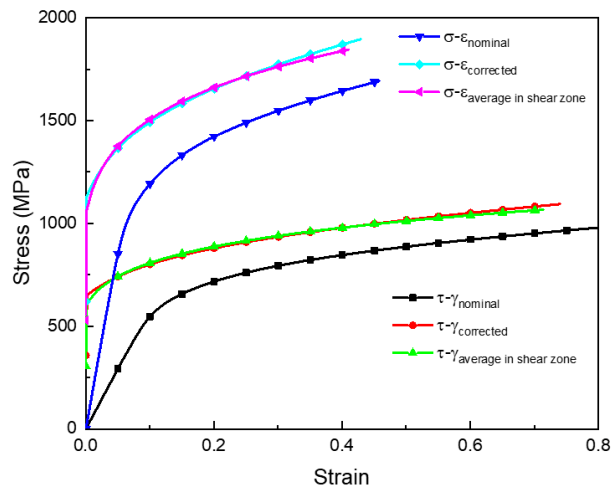


Fig. 3.25. Comparison of the flow stress curves before and after correction.

Table. 3.2. Corrective coefficients for SSS specimens with different shear zone width.

Specimen shear zone width L (mm)	λ_τ	λ_γ
0.3	0.860	1.055

0.5	0.870	1.070
1.0	1.120	1.030

Using Eq. 3.4 and 3.5 and the corrective coefficients in Table. 3.2, the nominal shear stress-nominal shear strain curves in Fig. 3.4 are converted to the correct stress-strain curves, Fig. 3.26. In order to validate the corrected stress-strain curves in Fig. 3.26, the numerical simulation described in section 4.1 was performed again. The purpose of the validation is to check if the experimental force-displacement data can be replicated with the use of the corrected $\sigma_{eq} - \varepsilon_{eq}$ curve in Fig. 3.26. All the model assembly, boundary conditions and mesh details are exactly the same except that the previous constitutive model to Abaqus is replaced by the $\sigma_{eq} - \varepsilon_{eq}$ curve shown in Fig. 3.26. An extension of the $\sigma_{eq} - \varepsilon_{eq}$ curve is necessary as the curve is obtained under the assumption of average equivalent plastic strain, while in reality particular elements in the specimen shear zone do experience much higher strains.

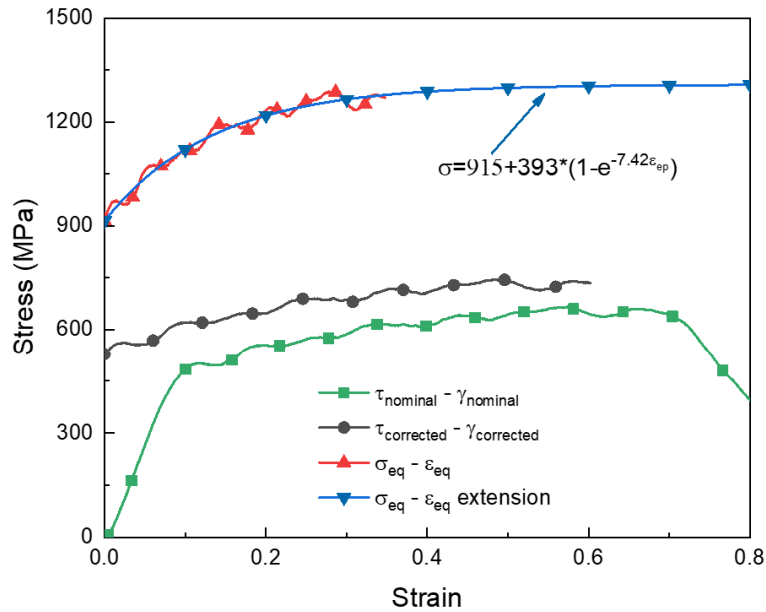


Fig. 3.26. Correction and extension of the nominal shear stress-nominal shear strain curve for numerical simulations.

A comparison between the numerical strain wave signals and the experimental ones are shown in Fig. 3.27. It is seen that all the incident, the reflected and the transmitted signals agree well with the experimental ones. Therefore, the input model to Abaqus, shown in Fig. 3.27, represents the deformation behavior of the tested material accurately.

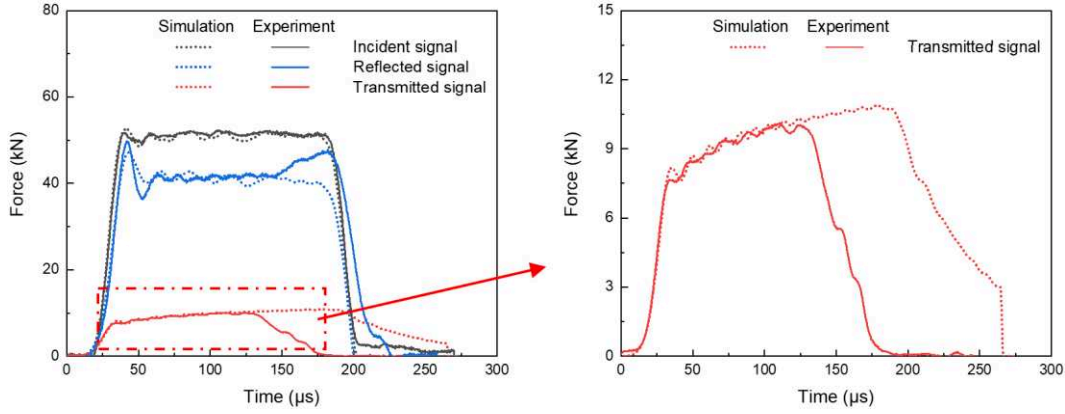


Fig. 3.27. Comparison between the experimental and numerical force wave signals.

5. Shear stress-shear strain relations of 304 ASS

The shear behavior of 304 ASS was studied over a wide range of strain rates (0.001 s^{-1} to 39000 s^{-1}) and temperatures (77 K to 473 K) using the SSS specimen and the data correction method. SSS specimens with different shear zone width L were used for various strain rate regimes: $L = 1 \text{ mm}$ for $\dot{\gamma}_{nominal} \leq 15000 \text{ s}^{-1}$; $L = 0.5 \text{ mm}$ for $15000 \text{ s}^{-1} \leq \dot{\gamma}_{nominal} \leq 30000 \text{ s}^{-1}$; $L = 0.3 \text{ mm}$ for $30000 \text{ s}^{-1} \leq \dot{\gamma}_{nominal}$.

Under quasi-static strain rates, the shear stress-shear strain curves obtained at three different temperatures are shown in Fig. 3.28. The temperature has a significant effect on the strain hardening rate: at 77 K, the flow stress curves show an obvious strain hardening effect; with the increasing temperatures from 77 K to 473 K, the strain hardening rate decreases monotonically; at 473 K, no strain hardening is observed anymore and the corresponding flow stress basically keeps constant at

different shear strains. Compared to temperature, no obvious effect of the strain rate on the strain hardening rate is observed. The average strain hardening rates for 77, 293 and 473 K are 484, 300 and 67 MPa/Unit strain, respectively. The temperature's effect on the flow stress can be seen from the curves clearly. Under both strain rates, the flow stress decreases evidently with increasing temperature. At 77 K, the flow stress at a shear strain of 0.2 is 776 MPa; the values reduce by 30.5% and 45.2% at 293 and 423 K, respectively. Concerning strain rate's effect on the flow stress of the curves, no evident difference exists between the two strain rates 0.001 and 0.1 s^{-1} .

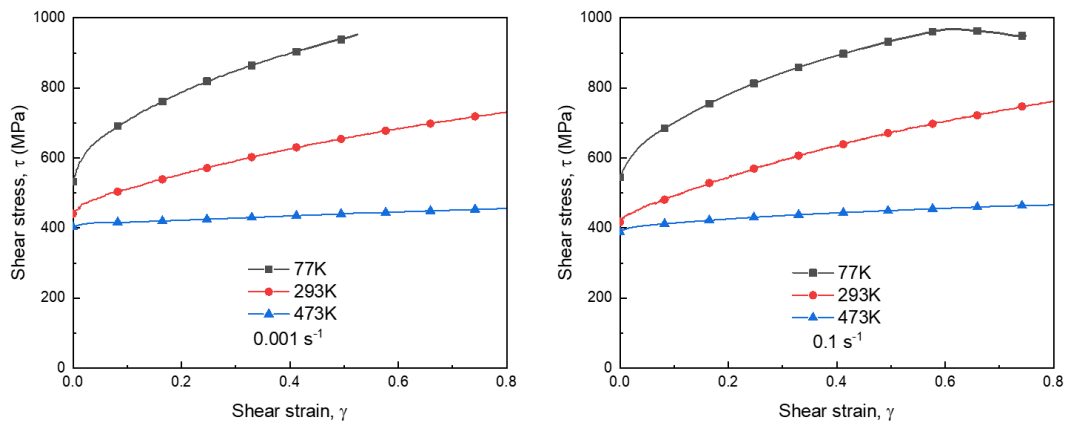


Fig. 3.28. Shear stress-shear strain curves of 304 ASS at three temperatures under quasi-static strain rates: (a) 0.001 s^{-1} and (b) 0.1 s^{-1} .

The dynamic shear stress-shear strain ($\tau - \gamma$) curves obtained at six shear strain rates (3000 s^{-1} to 39000 s^{-1}) and three temperatures (77 K to 473 K) are shown in Fig. 3.29. The influence of temperature on the flow stress and strain hardening rate of the curves is similar to that under quasi-static strain rates: both the flow stress and the strain hardening rate decrease gradually with the increasing temperature. At the maximum temperature of 473 K, the flow stresses either keep constant at different shear strains or show a negative strain hardening rate. The strain rate's effect on the flow stress can be seen clearly from the curves. The flow stress increases abruptly with the increasing shear strain rate. For example, from 3000 s^{-1} to 39000 s^{-1} , the flow stresses at the shear strain of 0.1 increase obviously by 38.4%, 27.9% and 31.7%

for 77 K, 293 K and 473 K, respectively. Concerning the strain rate's effect on the strain hardening rate, it keeps positive at shear strain rates below 26000 s^{-1} first but then changes into negative at the maximum shear strain rate of 39000 s^{-1} .

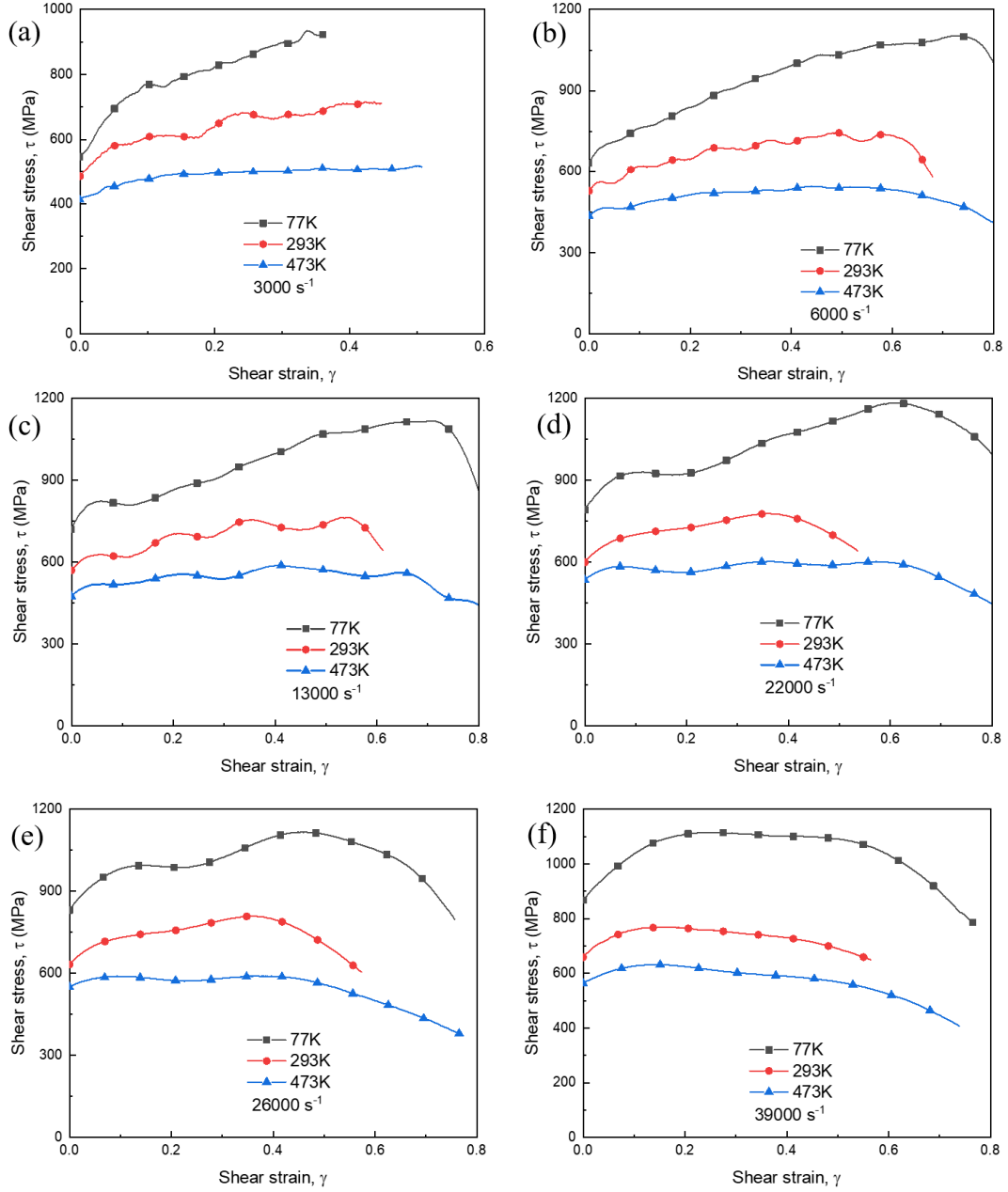


Fig. 3.29. Shear stress-shear strain curves of 304 ASS at three temperatures under different shear strain rates: (a) 3000 s^{-1} , (b) 6000 s^{-1} , (c) 13000 s^{-1} , (d) 22000 s^{-1} , (e) 26000 s^{-1} and (f) 39000 s^{-1} .

To study the effects of temperature and strain rate on the flow stress in more

details, the evolution of the flow stress as a function of strain rate for three temperatures is shown in Fig. 3.30. Both strain rate hardening and thermal softening can be seen from the curves clearly. Under quasi-static strain rates, the flow stress keeps constant for all the three temperatures. From 0.1 s^{-1} to 6000 s^{-1} , a slight enhancement in flow stress with increasing strain rate is identified. Concerning even higher strain rate regime, a rapid upturn of flow stress with strain rate is observed, indicating a fast increase in strain rate sensitivity. For example, from 12000 s^{-1} to 39000 s^{-1} at 77 K, 293 K and 473 K, the corresponding flow stresses increase by 30.5%, 12.7% and 16.0%, respectively. The enhanced strain rate sensitivity at shear strain rates above 6000 s^{-1} is commonly attributed to the change of rate-controlling deformation mechanism from thermal activation to viscous drag. A typical flow stress behavior of metallic materials dominated by thermal activation mechanism is shown in Fig. 2.11. The total flow stress can be decomposed into the athermal part σ_μ and the thermal part σ^* . In the thermal part, the barriers to dislocation motion can be readily overcome with the aid of the thermal activation energy. Therefore, with the increasing temperature, the effective stress needed for dislocation to pass through the barriers declines gradually. Moreover, at increasing strain rates, the time available for dislocations to accumulate a vigorous thermal fluctuation for overcoming the barriers reduces. Consequently, a higher effective stress is needed for continuation of the dislocation movement. At very high strain rates, due to the interactions of dislocation-phonon and dislocation-electron, the viscous drag effect surpasses the thermal activation mechanism and becomes dominant. Hence, a dramatic flow stress increase is observed in this strain rate regime. In addition, Follansbee and Kocks [16,17] investigated the deformation behavior of pure copper under strain rates between 10^{-4} s^{-1} and 10^4 s^{-1} . An enhanced dislocation accumulation rate is observed at strain rates higher than 10^3 s^{-1} , and this leads to the apparent strong flow stress increase. Therefore, enhanced dislocation accumulation instead of the viscous drag effect is another likely explanation of the strong strain rate sensitivity at extreme high strain rates.

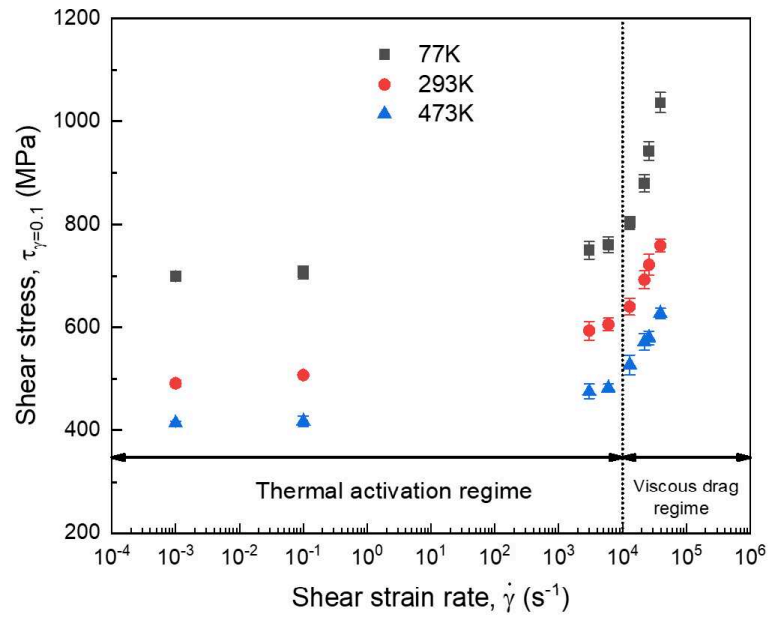


Fig. 3.30. Flow stress as a function of shear strain rate at three different temperatures.

To investigate the strain hardening rate quantitatively, the plastic deformation stage of the shear stress-shear strain curves is fitted linearly, and the slope of the fitted lines is regarded as the average strain hardening rate. The evolution of the strain hardening rate as a function of shear strain rate for three temperatures is shown in Fig. 3.31. It is seen that with the increase of temperature, the strain hardening rate decreases continuously. For example, at 0.001 s⁻¹ and 77 K, the average strain hardening rate is 695 MPa, and then the value reduces by 42.4% and 88.8% at 293 and 473 K, respectively. The effect of shear strain rate on the strain hardening rate can be divided into two regimes: from 0.001 s⁻¹ to 3000 s⁻¹, the strain hardening rate keeps almost constant; at even higher shear strain rates exceeding 3000 s⁻¹, the strain hardening rates decrease monotonically for all the three temperatures. Specially, at the maximum shear strain rate of 39000 s⁻¹, the strain hardening rates become negative, indicating a decrease of flow stress with increasing shear strain. In addition, although the strain hardening rate is elevated at lower temperatures, it declines more dramatically. From 3000 s⁻¹ to 26000 s⁻¹, the evolution of the strain hardening rate is fitted linearly and the slopes of the curves are -223, -108 and -55.3 MPa/Unit strain

rate for 77, 293 and 473 K, respectively. At the maximum shear strain rate of 39000 s⁻¹, the strain hardening rates for the three temperatures become close to each other. The evolution of strain hardening rate with strain rate and temperature can be explained according to the thermally activated dislocation motion theory [18] too. The strain hardening rate originates from a competition between the generation, multiplication and annihilation of dislocations. At elevated temperatures, the dislocations overcome the encountered barriers more easily with the aid of thermal activation energy. Hence, both the thermal part σ^* of the total flow stress and the corresponding strain hardening rate decrease. At dynamic strain rates, due to the adiabatic heating effect, the strain hardening rate is weakened. According to the work of Vazquez-Fernandez et al. [19], the Taylor–Quinney coefficient, characterizing the fraction of plastic work converted to heat, cannot be regarded as a constant and is elevated at increasing strain rates. Moreover, Behrens et al. [20] and Bronkhorst et al. [21] found even under dynamic strain rates exceeding 1000 s⁻¹, thermal conduction still exists but the time available for the heat dissipates to the surroundings is reduced: it is not accurate to assume the deformation process to be 100% adiabatic. Therefore, thermal softening caused by adiabatic heating effect exists in all dynamic shear tests but is more obvious at higher strain rates. In addition, as shown in Fig. 2.11, the ratio of the thermal part σ^* to the total flow stress declines with the increasing temperature. Hence, during dynamic shear tests, adiabatic heating has less effect on the deformation process at elevated temperatures. Therefore, the influence of strain rate on the strain hardening rate is weakened at high temperatures.

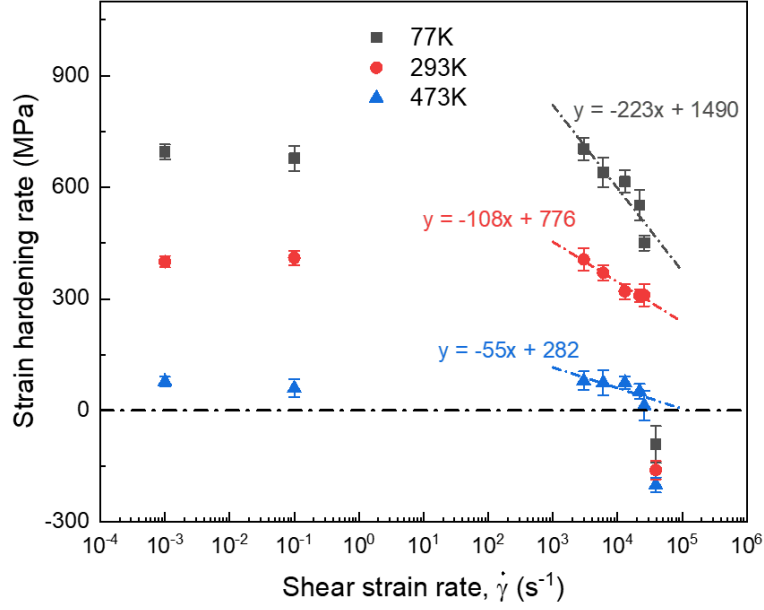


Fig. 3.31. Strain hardening rate as a function of shear strain rate at three different temperatures.

6. Conclusion

In this chapter, a new kind of SSS specimen is presented for shear behavior characterization of bulk metals using the traditional SHPB system. Using the SSS specimen, the shear properties of bulk metals can be tested over a wide range of shear strain rates (between 10^{-3} s^{-1} and 39000 s^{-1}) under a stress state of simple shear.

According to numerical results, deformation of the specimen shear zone is dominated by shear stress/ strain components. Stress state parameters represented by stress triaxiality η and Lode angle parameter μ are pretty low, representative of simple shear. Besides, the relationship between the real and the nominal shear stress-shear strain curves is not straight-forward. A corrective coefficient method helps to extract the real shear behavior from the experimentally obtained force-displacement data.

The technique was applied to 304 ASS over a wide range of shear strain rates (0.001 s^{-1} , 0.1 s^{-1} , 3000 s^{-1} , 6000 s^{-1} , 13000 s^{-1} , 22000 s^{-1} , 26000 s^{-1} , 39000 s^{-1}) and

temperatures (77 K, 293 K, 473 K). The temperature has an obvious effect on both the flow stress and the strain hardening rate: they decrease gradually with the increasing temperature. The effect of strain rate on the flow stress can be divided into two regimes: from 0.1 s^{-1} to 6000 s^{-1} , a slight increase in flow stress with increasing strain rate is identified. At even higher strain rate regime, due to viscous drag effect or enhanced dislocation accumulation, a rapid upturn of flow stress with strain rate is observed. The effect of strain rate on the strain hardening rate mainly comes from the adiabatic heating effect: during dynamic shear tests, the thermal softening effect becomes more obvious at higher strain rates. Under the maximum shear strain rate of 39000 s^{-1} , a negative strain hardening rate is observed.

Reference

- [1] Dorogoy A, Rittel D, Godinger A. A Shear-Tension Specimen for Large Strain Testing. *Exp Mech* 2016;56:437–49. doi:10.1007/s11340-015-0106-1.
- [2] Peirs J, Verleysen P, Degrieck J. Novel Technique for Static and Dynamic Shear Testing of Ti6Al4V Sheet. *Exp Mech* 2012;52:729–41. doi:10.1007/s11340-011-9541-9.
- [3] Dorogoy A, Rittel D, Godinger A. Modification of the Shear-Compression Specimen for Large Strain Testing. *Exp Mech* 2015;55:1627–39. doi:10.1007/s11340-015-0057-6.
- [4] Xu Z, Liu Y, Sun Z, Hu H, Huang F. On shear failure behaviors of an armor steel over a large range of strain rates. *International Journal of Impact Engineering* 2018;118:24–38. doi:10.1016/j.ijimpeng.2018.04.003.
- [5] Experimental Study of Sheet Metals under Dynamic Double Shear at Large Strains n.d. <https://www.scientific.net/KEM.274-276.787> (accessed September 14, 2018).

- [6] Shi FF, Merle R, Hou B, Liu JG, Li YL, Zhao H. A critical analysis of plane shear tests under quasi-static and impact loading. *International Journal of Impact Engineering* 2014;74:107–19. doi:10.1016/j.ijimpeng.2014.06.012.
- [7] Dorogoy A, Rittel D. Dynamic large strain characterization of tantalum using shear-compression and shear-tension testing. *Mechanics of Materials* 2017;112:143–53. doi:10.1016/j.mechmat.2017.06.003.
- [8] Chen G, Hao Y, Chen X, Hao H. Compressive behaviour of tungsten fibre reinforced Zr-based metallic glass at different strain rates and temperatures. *International Journal of Impact Engineering* 2017;106:110–9. doi:10.1016/j.ijimpeng.2017.03.017.
- [9] 田杰, 胡时胜. 准静态压缩应力-应变曲线测量方法的探索. *实验力学* 2005;20:265–9.
- [10] Formation of adiabatic shear band within Ti–6Al–4V: Effects of stress state. *Mechanics of Materials* 2019;137:103102. doi:10.1016/j.mechmat.2019.103102.
- [11] Fransplass H, Langseth M, Hopperstad OS. Experimental and numerical study of threaded steel fasteners under combined tension and shear at elevated loading rates. *International Journal of Impact Engineering* 2015;76:118–25. doi:10.1016/j.ijimpeng.2014.08.004.
- [12] Xu Z, Ding X, Zhang W, Huang F. A novel method in dynamic shear testing of bulk materials using the traditional SHPB technique. *International Journal of Impact Engineering* 2017;101:90–104. doi:10.1016/j.ijimpeng.2016.11.012.
- [13] Meyer LW, Krüger L. Drop-weight compression shear testing. *ASM Handbook* 2000;8:452–454.
- [14] Rusinek A, Klepaczko JR. Shear testing of a sheet steel at wide range of strain rates and a constitutive relation with strain-rate and temperature dependence of the

flow stress. *International Journal of Plasticity* 2001;17:87–115. doi:10.1016/S0749-6419(00)00020-6.

[15] VOCE E. The Relationship between Stress and Strain for Homogeneous Deformation. *Journal of the Institute of Metals* 1948;74:537–62.

[16] Follansbee PS, Kocks UF. A constitutive description of the deformation of copper based on the use of the mechanical threshold stress as an internal state variable. *Acta Metallurgica* 1988;36:81–93. doi:10.1016/0001-6160(88)90030-2.

[17] Zerilli FJ, Armstrong RW. The effect of dislocation drag on the stress-strain behavior of F.C.C. metals. *Acta Metallurgica et Materialia* 1992;40:1803–8. doi:10.1016/0956-7151(92)90166-C.

[18] Kocks UF, Argon AS, Ashby MF. *Thermodynamics and Kinetics of Slip*. Argonne National Laboratory; 1973.

[19] Vazquez-Fernandez NI, Soares GC, Smith JL, Seidt JD, Isakov M, Gilat A, et al. Adiabatic Heating of Austenitic Stainless Steels at Different Strain Rates. *J Dynamic Behavior Mater* 2019;5:221–9. doi:10.1007/s40870-019-00204-z.

[20] Behrens B-A, Chugreev A, Bohne F, Lorenz R. Approach for modelling the Taylor-Quinney coefficient of high strength steels. *Procedia Manufacturing* 2019;29:464–71. doi:10.1016/j.promfg.2019.02.163.

[21] Bronkhorst CA, Cerreta EK, Xue Q, Maudlin PJ, Mason TA, Gray GT. An experimental and numerical study of the localization behavior of tantalum and stainless steel. *International Journal of Plasticity* 2006;22:1304–35. doi:10.1016/j.ijplas.2005.10.002.

Chapter 4 Perforation behavior of 304 ASS

1. Introduction

During the service process, 304 ASS may be subjected to impact loading over a wide range of temperatures. For example, liquid natural gas storage and transportation at low temperature [1,2], or during sheet metal forming at high temperatures [3,4]. However, in this case, the behavior of 304 ASS remains unclear: the purpose is here to study the effect of the initial temperature on the perforation and failure behavior of 304 ASS.

First, an original cooling device was developed to test the structure behavior at low temperatures, ranging from -163°C to -20°C . The temperature distribution along the specimen surface was measured and simulated to be sure about the uniform temperature distribution.

Then, ballistic impact tests were carried out on 304 steel plates under temperatures from -163°C to 200°C using the newly developed cooling device and a heating chamber (Rusinek et al. [5]). The target thickness was 1.5 mm and the projectile velocity was varying between 80 to 180 m/s. The experimental setup allowed measuring the initial and residual velocities V_0 and V_R . Based on the compression behavior obtained in chapter 2, numerical simulations of the perforation process have been finally launched and compared to the experimental results.

In addition, the volume fraction of martensite in the perforated specimens was measured by the X-ray diffraction technique to explain the improved energy absorption capacity of 304 ASS at low temperatures.

2. Material and setup description

2.1 Ballistic impact setup

Ballistic impact tests were performed on 304 ASS using the device shown in Fig. 4.1 (a). During the testing process, the projectile is launched using a pneumatic gas gun and goes through the gas gun tube. At the end of the gun barrel, two laser sensors are fixed to measure the initial velocity of the projectile V_0 , Fig. 4.1 (b). When the projectile cuts off the first laser, a time counter t_1 is triggered. Similarly, another time counter t_2 is triggered when the projectile comes to the second laser. The time for the projectile to go from the first laser to the second one is $\Delta t = t_1 - t_2$. As the distance Δd between the two laser sensors is measured, V_0 can be obtained easily. With the same measurement method, the residual velocity of the projectile V_R is measured after the perforation process, Fig. 4.1 (c). By changing the initial gas gun pressure P_0 , the impact velocity V_0 of the projectile may change up to more than 180 m/s for a projectile mass of 29 g.

In addition, the ballistic impact device is equipped with piezoelectric sensors for resistance force measurement, Fig. 4.1 (d). Four sensors are fixed on the four corners of the rigid target holder. The maximum force for each sensor is 15 kN, so the sensor group works well within 60 kN. The experimentally measured initial-residual velocity curves and the resistance force data reflect not only the ballistic impact behavior of the tested material but also the mechanical response of the whole set-up. What's more, the experimental data can be used to validate the numerical results.

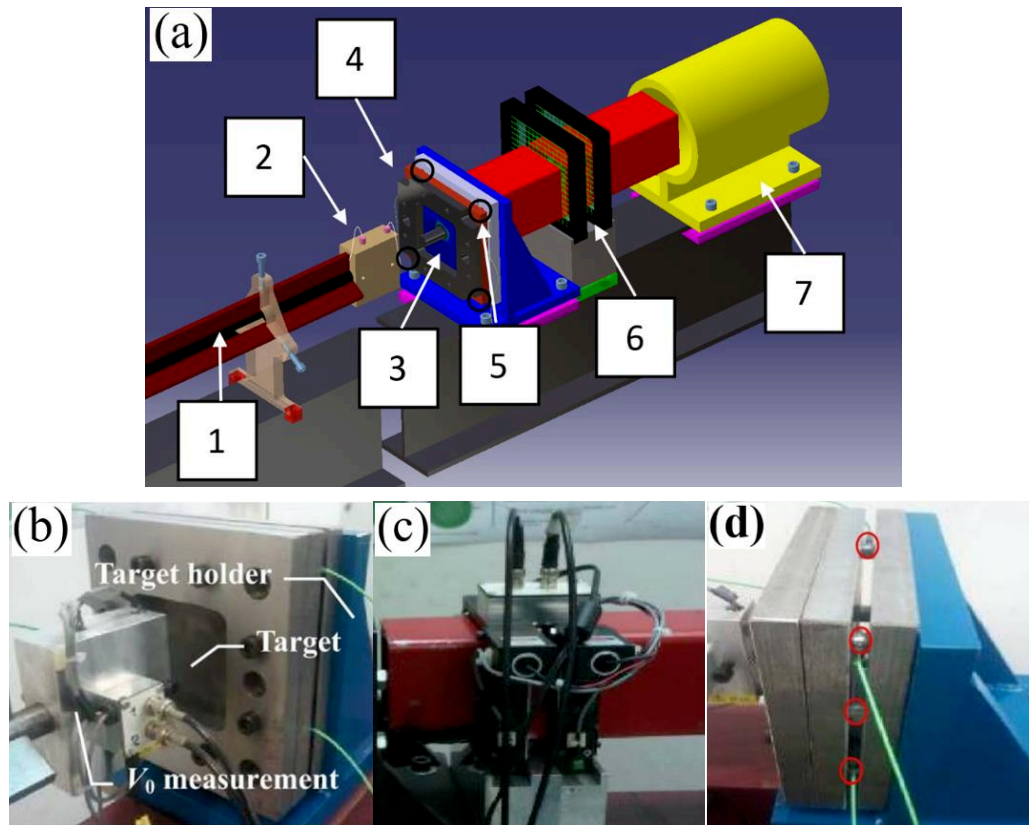


Fig. 4.1 (a) Schematic view of the ballistic impact device: 1) gun barrel, 2) initial velocity measurement, 3) target, 4) target holder, 5) force sensor, 6) residual velocity measurement, 7) projectile catcher. (b) Initial velocity measurement. (c) Residual velocity measurement. (d) Force sensors.

Experimental results such as target deflection, fracture pattern and energy absorption capacity of materials are all influenced by the shape and mechanical properties of the projectile. Hence, it will be introduced in the next section.

2.2 Projectile and target description

Projectiles with various nose shapes such as conical, blunt and hemispherical are commonly used to study the ballistic impact behavior of thin metallic plates, Fig. 4.2. For conical shape projectile, the plates fail by ductile petalling resulting from radial necking, whereas for blunt shape projectile a plug ejection due to high strain rate shearing is frequently observed. Finally, circumferential necking and the

corresponding plug ejection is observed in hemispherical shape projectile. The different failure behaviors are mainly controlled by the stress state dependent failure modes. The stress triaxiality values for conical, blunt and hemispherical shape projectiles are found to be $1/3$, 0 and $2/3$ respectively. A failure criterion taking effect of stress triaxiality into consideration is needed for accurate perforation behavior modelling.

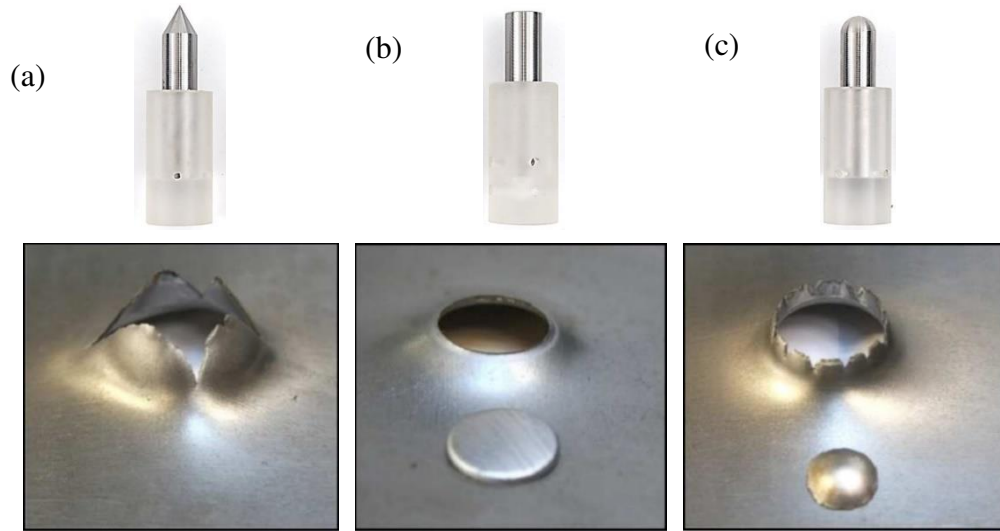


Fig. 4.2. The failure patterns for different kinds of projectiles: (a)conical; (b) hemispherical and (c) blunt [6,7].

In this work, we aimed to study the effect of testing temperature on the perforation behavior of 304 ASS. A conical projectile is chosen for the study as the perforation details such as the failure pattern and the number of petals change significantly under different temperatures. Dimensions of the conical projectile are shown in Fig. 4.3. It is a cylinder with 12.8 mm in diameter and 25 mm in length and corresponding to a mass of 29 g. At the top of the cylinder, a conical nose with an angle of 72° is machined as reported in [8]. The projectile is made of Maraging steel with a hardness of 640 HV and a yield stress of 2 GPa. The hardness and the strength are so high that the projectile is assumed to be rigid during experiments and numerical simulations.

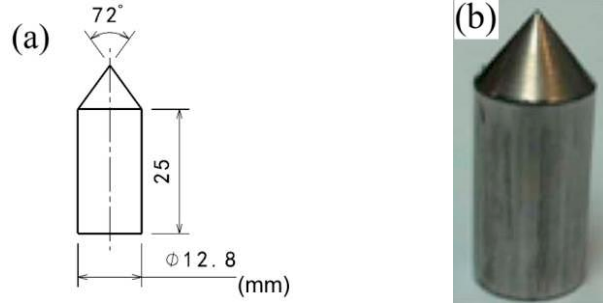


Fig. 4.3. Geometry and dimensions of the conical projectile used in perforation tests: (a) schematic illustration and (b) actual shape.

The specimens were delivered as thin plates the dimensions of which are $130 \times 130 \times 1.5 \text{ mm}^3$, Fig. 4.4. The initial microstructure was 100% austenitic and they were tightly fixed by the target holders to avoid sliding. The active surface area, after being clamped by the target holders, is $100 \times 100 \times 1.5 \text{ mm}^3$.

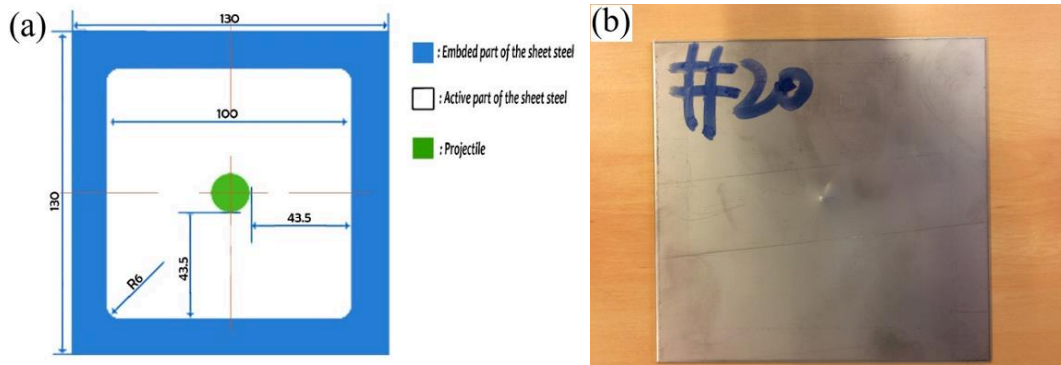


Fig. 4.4. Geometry and dimensions of the 304 ASS plates used in perforation tests: (a) schematic illustration and (b) actual shape.

After ballistic impact tests, the failure modes of the targets can be divided into three kinds: no perforation, critical perforation and complete perforation, as shown in Fig. 4.5. “No perforation” means initial velocity V_0 of the projectile is too small to go through the target and will be bounced back (Fig. 4.5 a). “Critical perforation” means kinetic energy of the projectile is enough to perforate the target but not enough to go any further, so it will be stuck in the target (Fig. 4.5 b). “Complete perforation” means the initial velocity V_0 of projectile is so high that it will perforate

the target and continue to fly a further distance with a residual velocity V_R (Fig. 4.5 c).

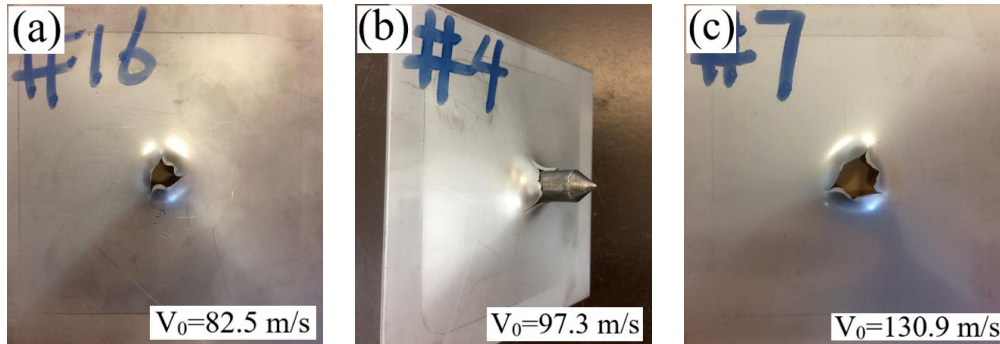


Fig. 4.5. Typical failure modes of the targets after perforation tests: (a) no perforation, (b) critical perforation, (c) complete perforation.

In order to perform perforation tests at various temperatures, a cooling device/heating furnace are adopted and will be introduced in the next section.

2.3 Thermal chamber/cooling device for high/low temperature perforation tests

For perforation tests at high temperature (200°C), a thermal chamber developed by Rusinek et al. [5] was adopted, Fig. 4.6. A furnace is used to heat up the air inside the chamber and then hot air is flowing around using a fan. A sarcophagus is used around the specimen so both sides of the specimen are heated up at the same time. By thermal conductivity and after a certain waiting time, the specimen reaches the expected temperature. Two thermocouples are fixed in the chamber: one to monitor the temperature inside the oven, another one in the center of the specimen to calibrate the temperature difference between the specimen and the air in the thermal chamber. Evolution of the two temperatures with time is shown in Fig. 4.7. The maximum initial testing temperature can be reached is 300°C . In order to reach a uniform temperature distribution in the specimen, a waiting time of 25 min is imposed.

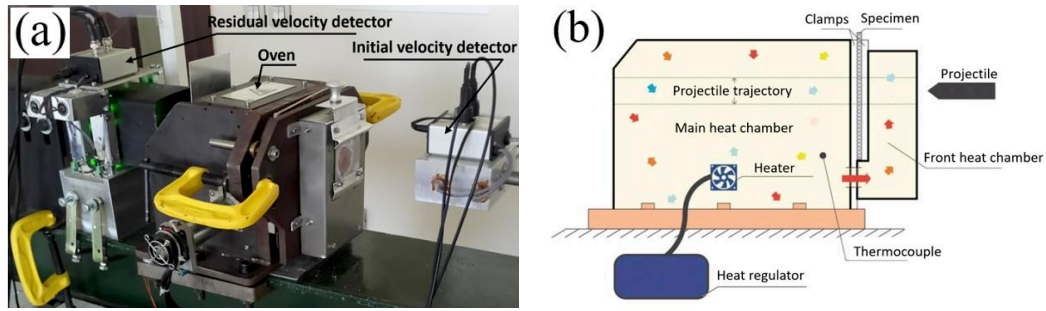


Fig. 4.6. Device for high temperature perforation testing: (a) general view of the ballistic impact system and (b) schematic view of the thermal chamber [5].

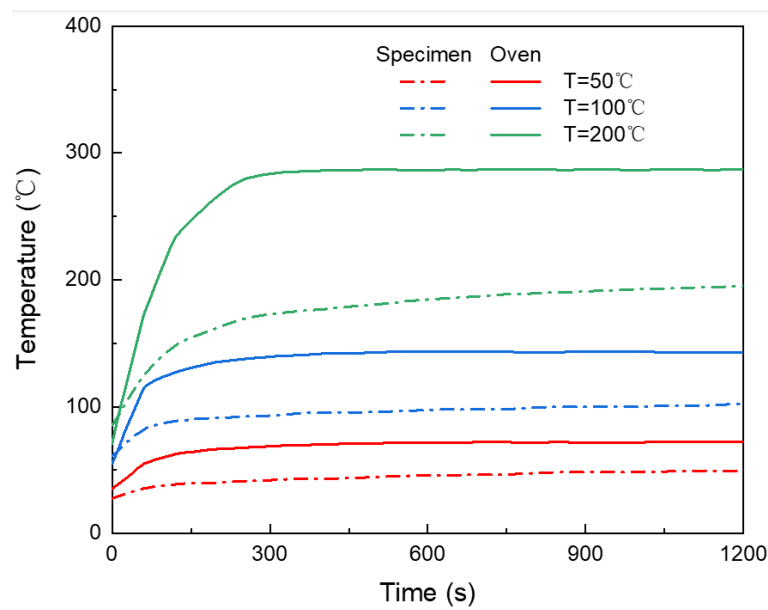


Fig. 4.7. The temperature evolution of the specimen by setting the oven temperatures to be 75°C, 145°C and 285°C.

To conduct perforation tests at low temperatures, a cooling device has been designed and developed. A schematic illustration and the corresponding practical arrangement are shown in Fig. 4.8 (a) and (b), respectively. The cooling box is fixed on the ballistic impact setup. On the one hand, the cold nitrogen gas flows from a liquid nitrogen tank through an aluminum pipe into the cooling box; on the other hand, the temperature inside the cooling box is monitored by a thermocouple connected to a temperature controller. Once the temperature inside the box reaches the set value, the temperature controller cuts off the power of the pump to stop the

nitrogen gas flow. By this method, low temperatures between -90°C and -20°C can be obtained. In addition, by filling the cooling box with liquid nitrogen directly, -163°C can be reached, Fig. 4.8 (c).

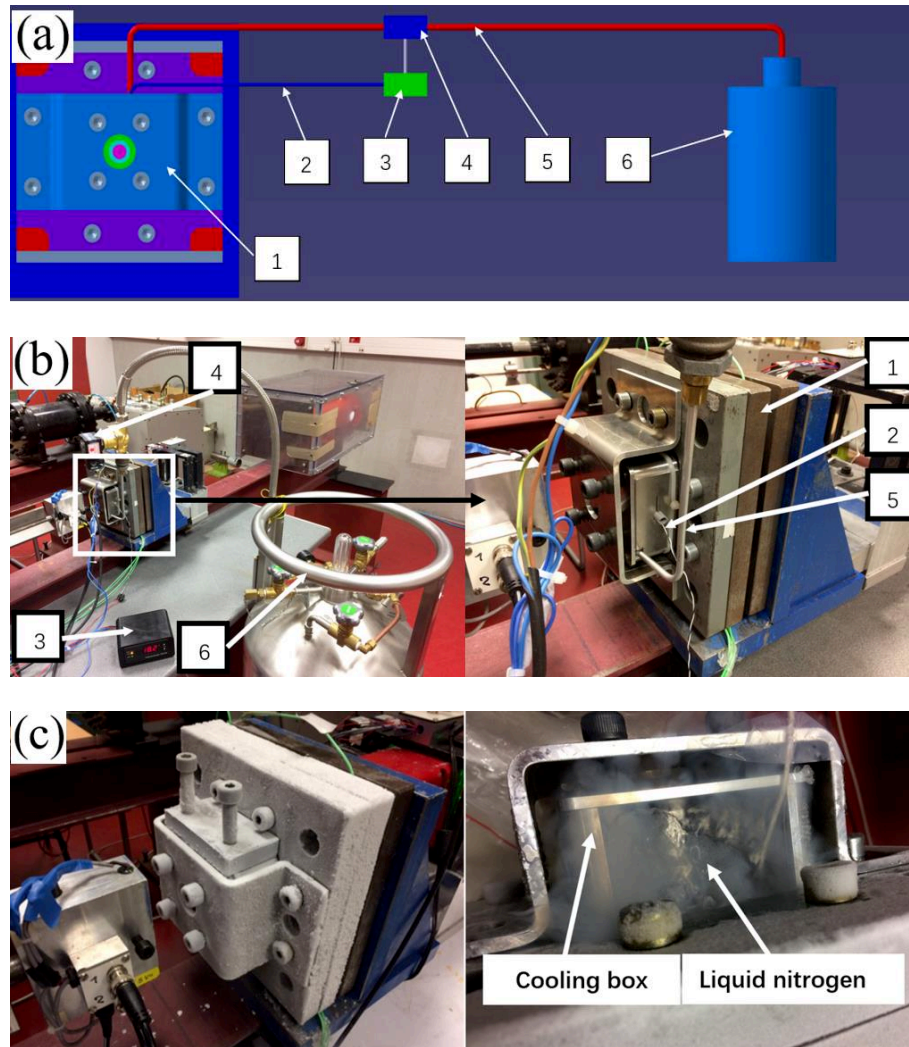


Fig. 4.8. Cooling device for ballistic impact tests at (a) and (b) between -90°C to -20°C and (c) at -163°C : 1) ballistic impact device, 2) thermocouple, 3) temperature controller, 4) pump, 5) pipe, 6) liquid nitrogen tank.

The arrangement of the cooling device on the ballistic impact device is shown in Fig. 4.9. The 304 ASS plate is fixed on the target holder and the cooling box is fixed on the target with another specific holder. The cooling box is made of aluminum alloy to ensure a good heat transfer. In addition, 4 screws are used to apply

a reduced force on the cooling box surface to ensure a tight contact between the plate and the cooling box during the whole testing process.

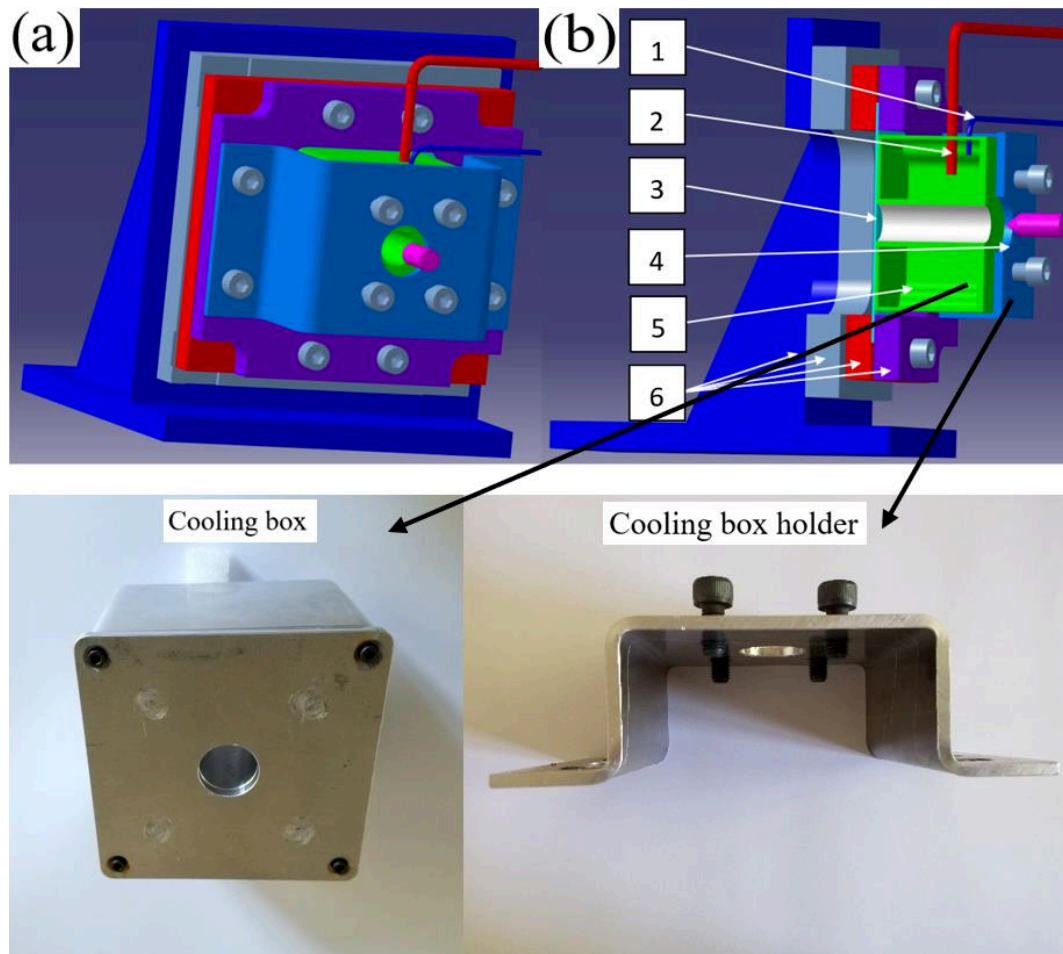


Fig. 4.9. Arrangement of the cooling device on the ballistic impact device: (a) isometric view and (b) sectional view: 1) thermocouple, 2) pipe, 3) target, 4) cooling box holder, 5) cooling box, 6) target holder.

3. Reliability verification of the cooling device

Since the cooling device for low temperature perforation tests was newly developed, its reliability should be verified before testing. Unlike the device for high temperature perforation tests in which the specimen is sealed firmly in a thermal chamber and a uniform temperature distribution is obtained easily, cryogenic

temperatures present an experimental complexity to be performed, especially in terms of stabilization at extreme low temperatures, close to -163°C . In addition, due to the decreasing thermal conductivity $k(T)$ and the specific heat capacity $C_p(T)$ under extreme low temperatures (Fig. 4.10), it is important to verify that the impacted zone is deformed in a uniform temperature environment.

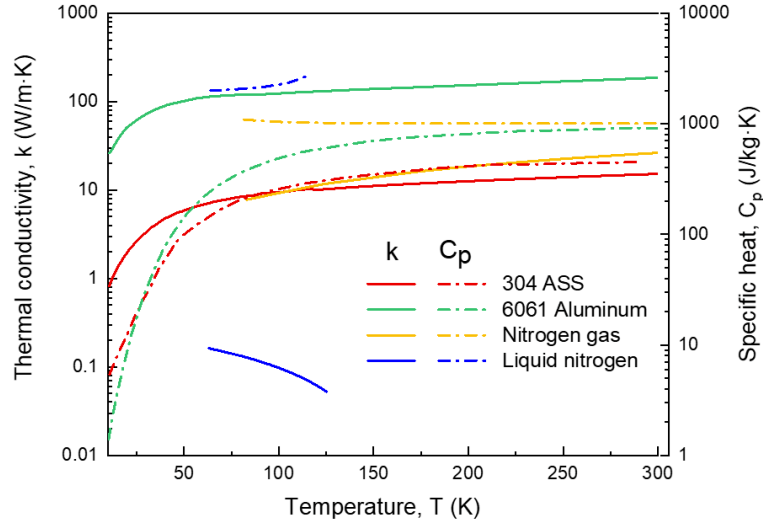


Fig. 4.10. Thermal conductivity k and specific heat C_p of materials used in the numerical simulations [9].

3.1 Temperature evolution and distribution along the diagonal line of the target

To verify the reliability of the cooling device, the temperature evolution and distribution in the target is measured and analyzed. As shown in Fig. 4.11 (a), the temperature of three radii on the target surface is measured (target center, 14 mm radius and 28 mm radius). The practical arrangement is shown in Fig. 4.11 (b), three thermocouples are fixed on the target surface by the laser welding method. It is supposed that temperature gradient does not exist along the thickness direction of the target. The measured temperature values represent the actual temperature on the target surface or inside the target.

The measurement results are shown in Fig. 4.12. By setting temperatures of the coolant to be -38°C , -64°C and -88°C , the corresponding temperatures on the target surface are -20°C , -40°C and -60°C , respectively. The temperature of -163°C is obtained directly by filling liquid nitrogen into the cooling box without using the temperature controller device. The temperature of the three locations is not exactly the same with $T_{14\text{mm}} < T_{\text{center}} < T_{28\text{mm}}$: it is due to the hole in the center of the cooling box, that is the path for the projectile to go through the cooling box and impact the target. Hence, the center of the target cannot be cooled by surface contact with the cooling box and its temperature is slightly higher. In fact, within an area 56 mm in diameter, the maximum temperature fluctuation is only 4°C . As the projectile diameter is only 12.8 mm, it can be assumed that the impacted zone is deformed in a uniform temperature environment.

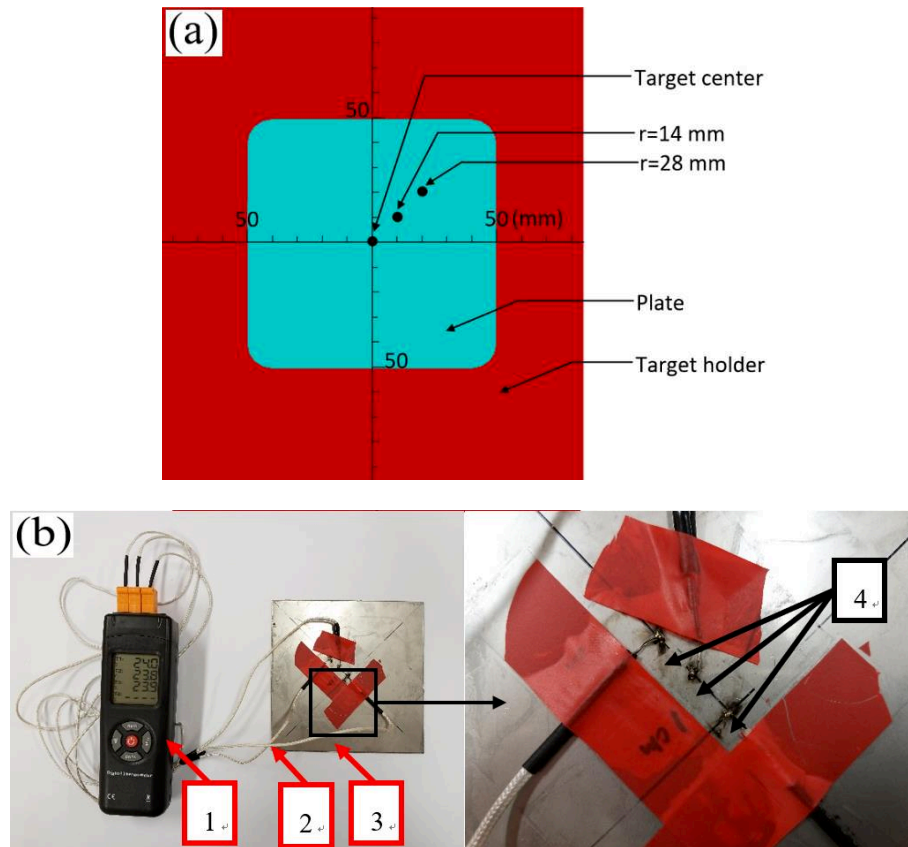


Fig. 4.11. Temperature measurement along the diagonal line of the target: (a) schematic illustration and (b) actual arrangement: 1) thermometer, 2)

thermocouple, 3) target, 4) temperature measurement points.

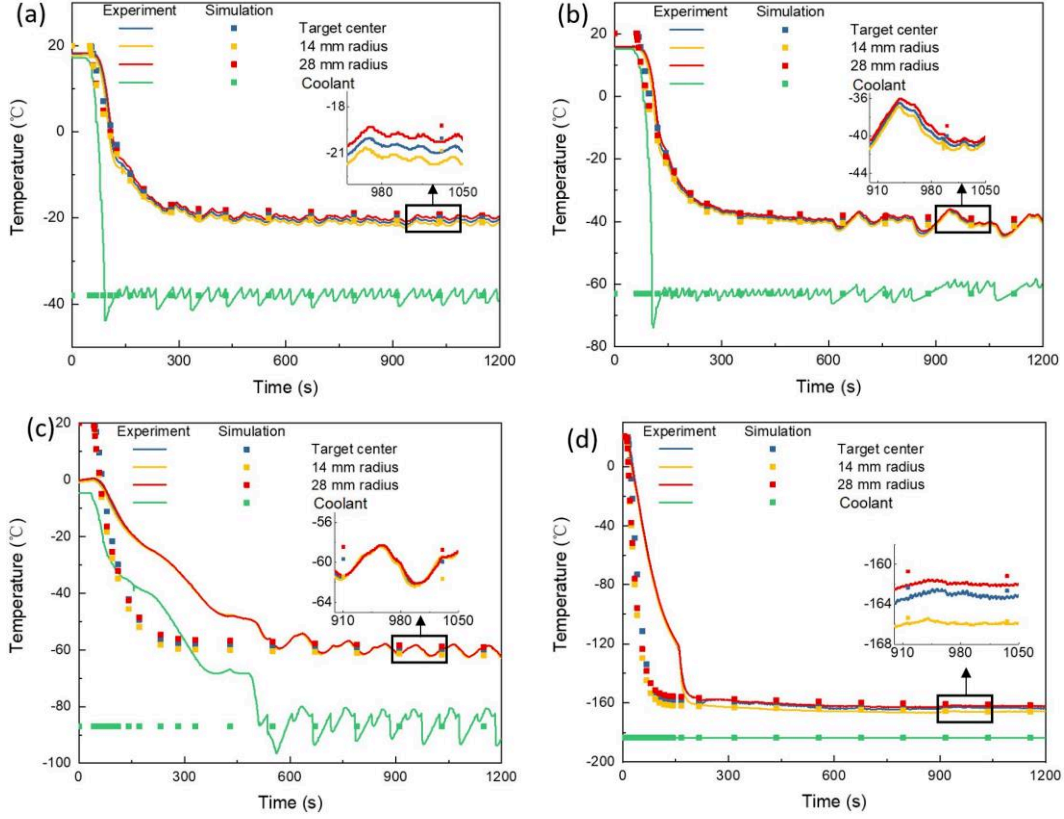


Fig. 4.12. Temperature distribution and evolution of the target with the coolant temperature set at: (a) -38°C , (b) -63°C , (c) -87°C and (d) -183°C .

3.2 Calibration and heat transfer modelling

To analyze the temperature uniformity on the target in details, numerical simulations using COMSOL Multiphysics have been performed. The thermal transfer is described by the generalized transient heat equation, Eq. 4.1.

$$\rho \cdot C_p(T) \cdot \frac{\partial T}{\partial t} - \nabla \cdot [k(T) \cdot \nabla T] = 0 \quad \text{Eq. 4.1}$$

The thermal conductivity $k(T)$ and the specific heat $C_p(T)$ of the materials used in the numerical simulations are shown in Fig. 4.10. The two parameters are strongly depending on the temperature, especially at very low temperatures.

The boundary conditions of the simulations are defined as follows, see Eq. 4.2, Eq. 4.3, Eq. 4.4 and Fig. 4.13:

- Natural convective heat flux q_c on the free surface of the device.
- Forced convective heat flux q_f through the inner free surfaces of the cooling box, due to the flow of the nitrogen gas.
- Thermal contact heat q_{int} between different interfaces of contacts in the device.

$$q_c = -h_c(T - T_0) \quad \text{in } \partial\Omega_c \quad \text{Eq. 4.2}$$

$$q_f = -h_f(T - T_0) \quad \text{in } \partial\Omega_f \quad \text{Eq. 4.3}$$

$$q_{int} = h_{int}(T - T_0) \quad \text{in } \partial\Omega_{int} \quad \text{Eq. 4.4}$$

where $h_c = 10 \text{ W}/(\text{m}^2 \cdot \text{K})$ and $h_f = 109 \text{ W}/(\text{m}^2 \cdot \text{K})$ are the natural and forced heat convection coefficients, respectively. The conductance h_{int} is equal to $10^5 \text{ W}/(\text{m}^2 \cdot \text{K})$.

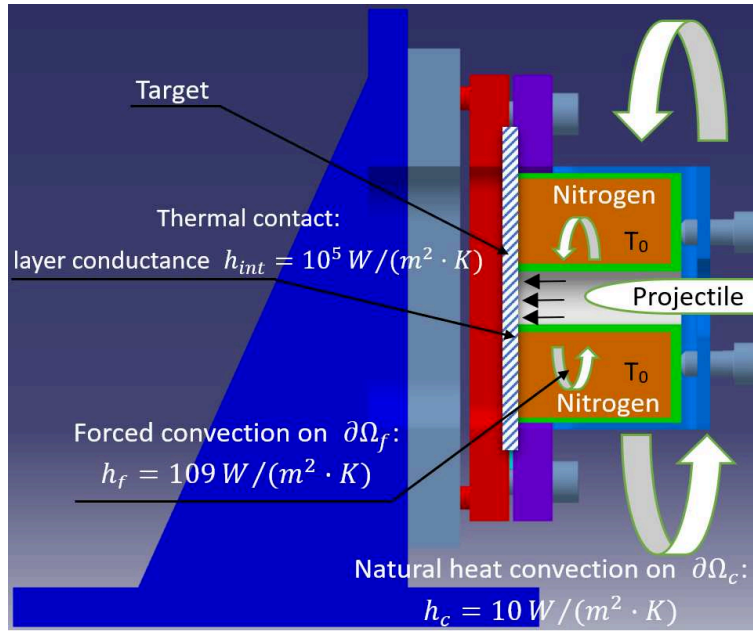
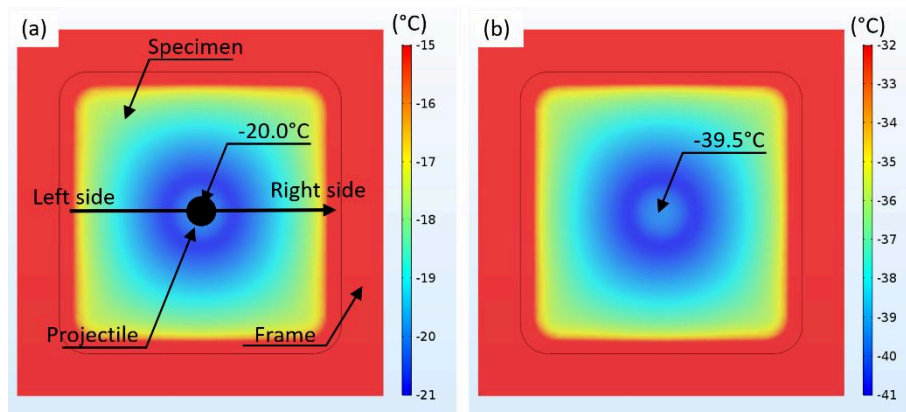


Fig. 4.13. Boundary conditions for temperature distribution analysis using COMSOL Multiphysics.

The numerical results are shown as dots in Fig. 4.12. In Fig. 4.12 (a) and (b): the numerical results and experiments are in good agreement. In Fig. 4.12 (c), the experimental curve decreases slower than the simulated one as the flow speed of nitrogen gas is slightly smaller. But after a certain waiting time around 500 s, the experimental values are consistent with the simulation results. In Fig. 4.12 (d), during the initial cooling stage, the experimental curve is comparatively higher. This is mainly because during experiments, it takes time to fill the cooling box with liquid nitrogen while it is assumed that the box is full of liquid nitrogen since the beginning of the simulations. In Fig. 4.12 (a), (b) and (c), the temperature fluctuation caused by the temperature controller is observed. In fact, the delay of the temperature controller is set to 3°C and it causes a temperature fluctuation of $\pm 3^\circ\text{C}$. In Fig. 4.12 (d), the target is cooled by filling the box with liquid nitrogen and the temperature fluctuation phenomenon is not observed anymore.

Based on numerical simulations, it is observed that the temperature distribution on the target surface at 1200 s may be assumed as uniform in the impact zone (Fig. 4.14). In fact, within the perforation zone, the maximum temperature differences in the four figures are 2°C, 3°C, 4°C and 8°C, respectively. For testing 304 ASS by a conical projectile, target deformation occurs mainly in the target center with a radius of 20 mm. Under this condition, the maximum temperature differences are 0.3°C, 0.4°C, 0.6°C and 1.4°C, respectively. Therefore, the temperature distribution on the target surface is pretty uniform during the perforation process.



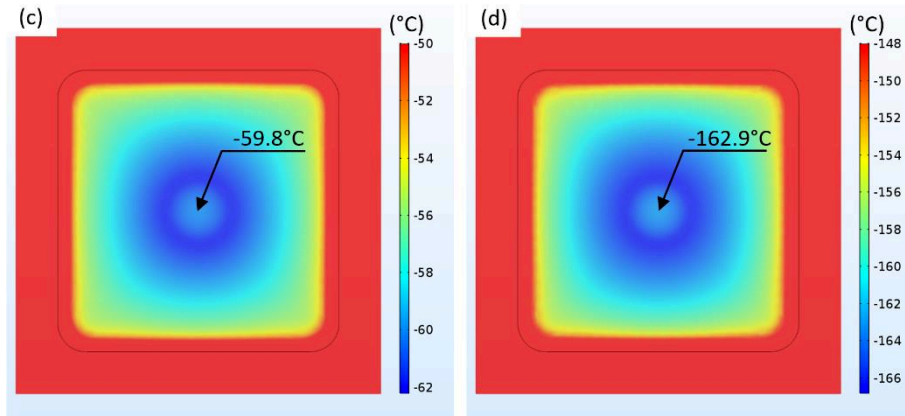


Fig. 4.14. Temperature distribution on target surface at 1200 s with the cooling box temperature set at: (a) -38°C , (b) -63°C , (c) -87°C and (d) -183°C .

In addition, the temperature evolution from the left edge to the right edge of the target (the black line in Fig. 4.14 (a)) is shown in Fig. 4.15. The temperature in the center of the target is slightly higher than the surrounding area, consistent with the experimental data in Fig. 4.12. Therefore, the simulation is in good agreement with experiments.

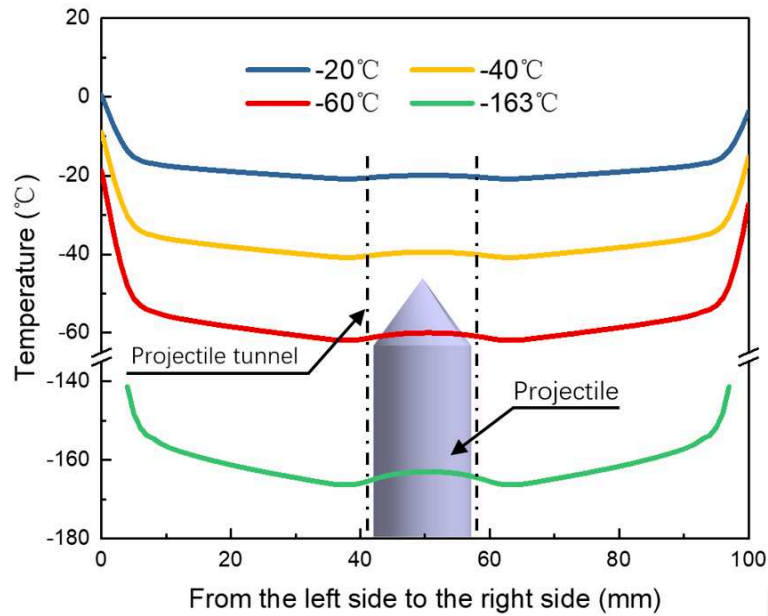


Fig. 4.15. Temperature from the left side to the right side of the target.

According to the temperature distribution analysis in this section, the temperature uniformity is obtained within the perforation area. Therefore, in the next

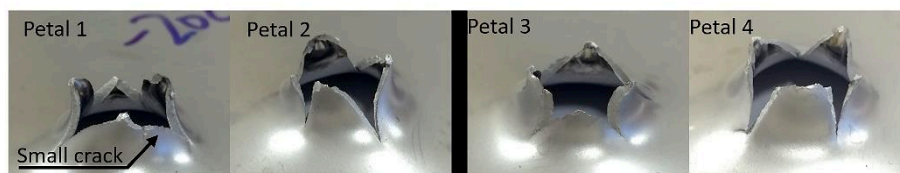
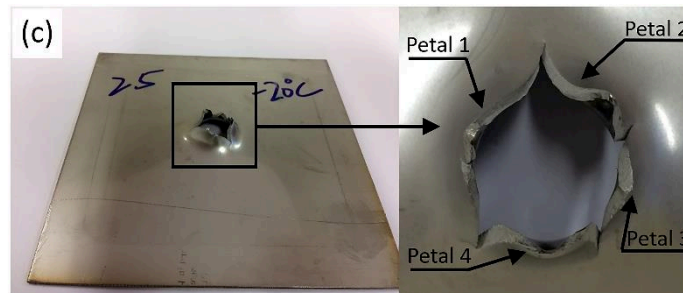
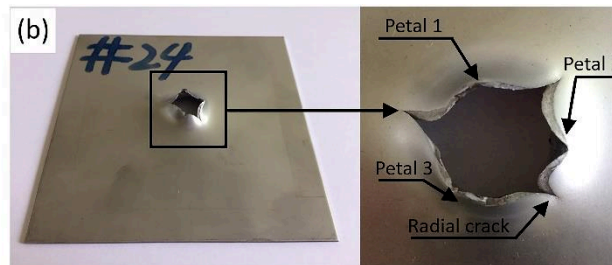
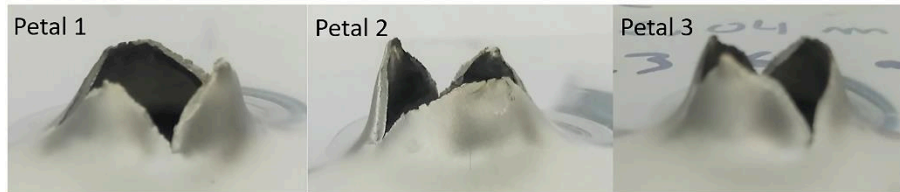
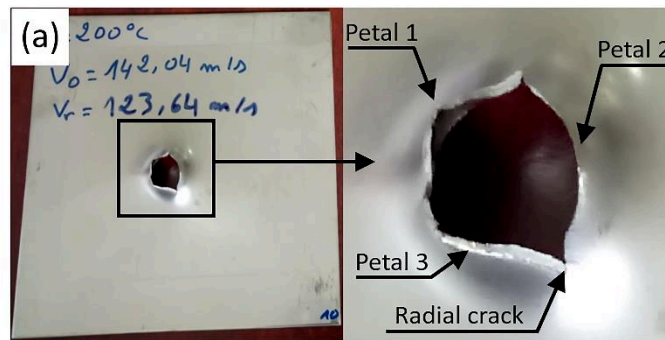
section, perforation tests of 304 ASS under low, room and elevated temperatures are performed and the results are presented.

4. Influence of testing temperature on the perforation process

In this section, perforation experiments were performed by a conical projectile for 5 initial temperatures: -163°C , -60°C , -20°C , 20°C and 200°C . The tests were conducted over a wide range of initial impact velocities, ranging from 80 to 180 m/s, to obtain a complete ballistic curve of the material. Therefore, the effect of the initial temperature on the perforation process is analyzed.

4.1 Effect of temperature on failure mode

The influence of the initial temperature on the failure mode of 304 ASS is shown in Fig. 4.16. For the tests at 200°C , failure by ductile petalling, resulting from radial necking during the piercing process [10] is observed. A representative petal pattern of the material at 20°C is shown in Fig. 4.16 (b), with a number of 3 triangle-shaped petals form: the shape of petals remains unchanged compared to 200°C but the fracture surface becomes slightly rough. In addition, several secondary cracks are observed on the bigger petals; if the crack propagates until the end of the petals, a failure pattern with 4 petals is observed. With a further decrease in testing temperature to -20°C , the average number of petals increases to 4 and the petal shape becomes irregular. One thing should be noticed is that no debris was found for the three testing temperatures above. Concerning perforation tests at -60°C and -163°C , the breaking patterns become even rougher including debris ejection. The average number of petals increases to 5 at -163°C , higher than that of -20°C , 20°C and 200°C . The end of the petals became pretty rugged and discontinuous. Moreover, a lot of small cracks were observed on the petal surfaces.



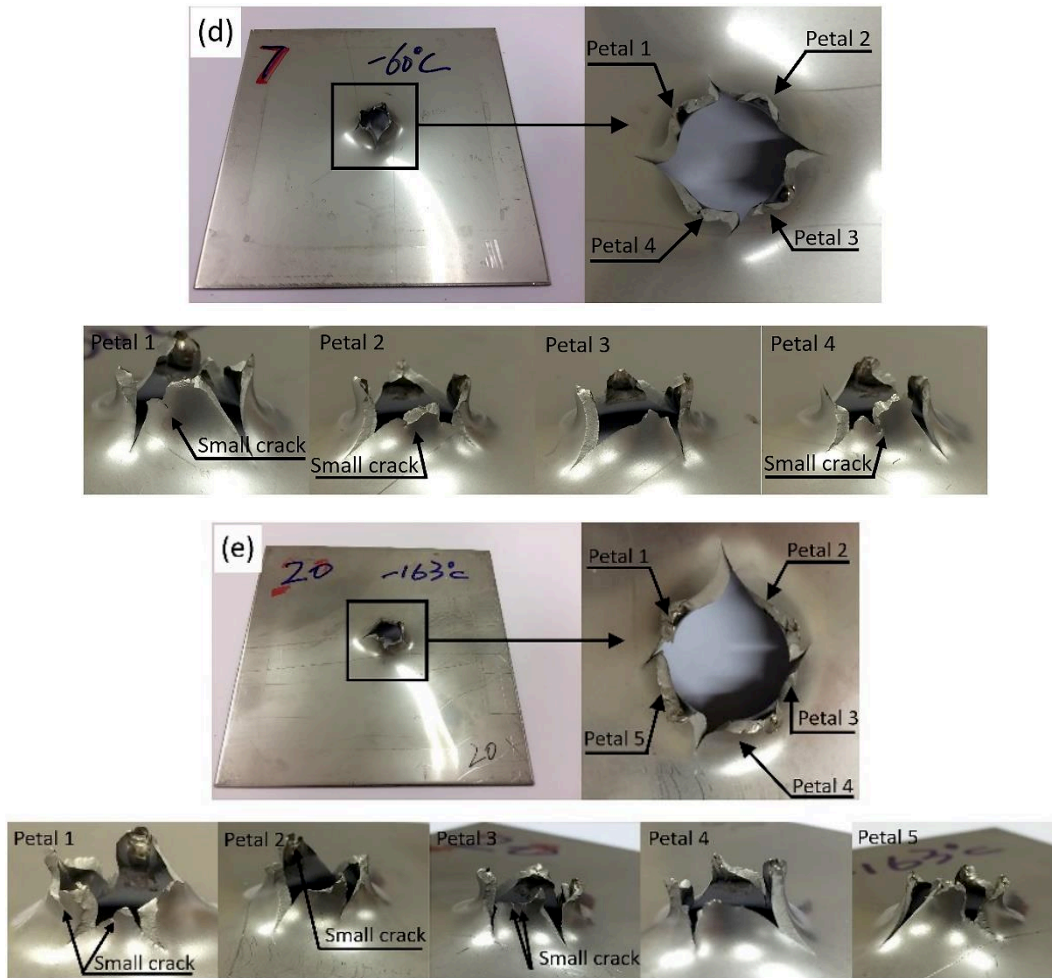


Fig. 4.16. Failure pattern for different testing temperatures: (a) 200°C, (b) 20°C, (c) -20°C, (d) -60°C and (e) -163°C.

In addition to the failure pattern, the ballistic curve $V_R - V_0$ and the ballistic limit velocity V_{bl} are also used to characterize the ballistic impact behavior of materials. They are presented as a function of the testing temperature in the next section.

4.2 Effect of temperature on the ballistic curves

Results in terms of ballistic curves $V_R - V_0$ are presented in Fig. 4.17. The curves are then fitted to the relation proposed by Recht and Ipson [11], Eq. 4.5, in which the residual velocity of the projectile is calculated as a function of the initial velocity

and the ballistic limit velocity.

$$V_R = (V_0^\alpha - V_{bl}^\alpha)^{1/\alpha} \quad \text{Eq. 4.5}$$

where V_0 and V_R are the initial and residual projectile velocities, V_{bl} is the ballistic limit velocity and α is a fitting parameter.

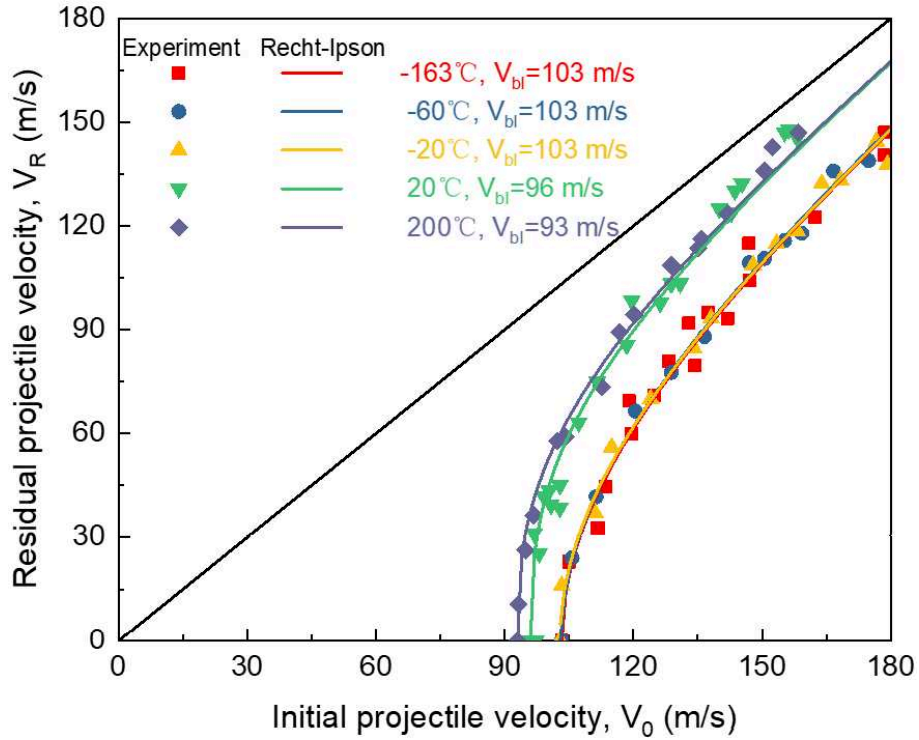


Fig. 4.17. Ballistic curves for 1.5 mm thick plates of 304 ASS impacted under different temperatures.

The ballistic limit velocities and fitting parameters for tests at different temperatures are given in Table. 4.1. As shown in Fig. 4.17, the equation defines the ballistic curve shape properly. For testing at -20°C , -60°C and -163°C , the ballistic limit velocity remains the same, 130 m/s. For testing at higher temperatures, V_{bl} decreases with increasing temperature. At a testing temperature of 200°C , the ballistic limit velocity is 93 m/s; while it is lower than that at 20°C , the difference between the two curves decreases with increasing impact velocity. At ballistic impact velocities higher than 150 m/s, the two curves coincide. The fitting parameter

α is also affected by testing temperature: the values at room and high temperatures are obviously lower than that at lower temperatures. A lower α means better impact resistance against projectile and higher ballistic limit velocity [12]. Therefore, the evolutions of experimentally obtained V_{bl} and α with testing temperature are consistent with each other.

Table. 4.1. The ballistic limit velocities V_{bl} and the fitting parameter α of 304 ASS under different testing temperatures.

Testing temperature (°C)	V_{bl} (m/s)	α
-163	103	2.006
-60	103	2.028
-20	103	2.005
20	96	2.712
200	93	2.660

Based on the ballistic curves $V_R - V_0$, the energy absorbed by the specimens can be calculated. In the next section, the effect of testing temperature and the initial projectile velocity V_0 on the energy absorption capacity of 304 ASS is analyzed.

4.3 Effect of temperature on the energy absorption capacity

During the perforation process, part of the kinetic energy of the projectile is absorbed by the plate. Knowing the initial V_0 and residual V_R velocities of the

projectile, the energy absorbed by the plate W_{Plate}^{Total} can be calculated as follows:

$$W_{Plate}^{Total} = \frac{1}{2} M_p (V_0^2 - V_R^2) \quad \text{Eq. 4.6}$$

where M_p is the mass of the projectile and equal to 29 g.

A part of the kinetic energy, Eq. 4.6, is transferred to the plate during the process of impact or perforation. However, as discussed in [10], the energy lost due to the elastic deformation of the plate, friction between the projectile and the target as well as that transferred to the ejected debris can be neglected. Therefore, the energy absorbed by the plate is then written as follows:

$$W_{Plate}^{Total} = W_{pb} + W_{ps} + W_p + W_c \quad \text{Eq. 4.7}$$

where W_{pb} is the plastic bending energy of the target, W_{ps} is the plastic stretching energy of the target, W_p is the plastic bending energy of the petals and W_c is the energy dissipation during crack formation and propagation process.

The energy absorption results as a function of V_0 for tests at different temperatures are presented in Fig. 4.18. First, energy absorption for tests at low temperatures (-163°C, -60°C and -20°C) is significantly higher than at 20°C, while energy absorption at 200°C is the lowest. This is consistent with the fracture pattern observed: more petals and cracks at low temperatures. A similar phenomenon was observed during low velocity perforation test of TRIP 1000 steel by Rodríguez-Martínez et al. [14]: the ballistic limit velocity V_{bl} changed from 2.6 to 3.1 m/s when testing temperature decreased from 15°C to -60°C. According to the analysis of Rodríguez-Martínez, the improved energy absorption at low temperature came from temperature sensitivity of the TRIP 1000 steel and no martensitic transformation was observed during the perforation process.

Another interesting phenomenon concerning the energy absorption capacity of 304 ASS is the evolution of the absorbed energy with impact velocity. For the tests

at low temperatures (-163°C , -60°C and -20°C), the initial projectile velocity V_0 does not affect the absorbed energy in the tested impact velocity range. In fact, the averaged energy absorption for these 3 temperatures are 156 J, 154 J and 155 J, respectively. However, for the tests at 20°C and 200°C , the absorbed energy decreases linearly with increasing impact velocity. Although the absorbed energy at 20°C is slightly higher than that at 200°C , it decreases faster and becomes lower at impact velocities larger than 137 m/s.

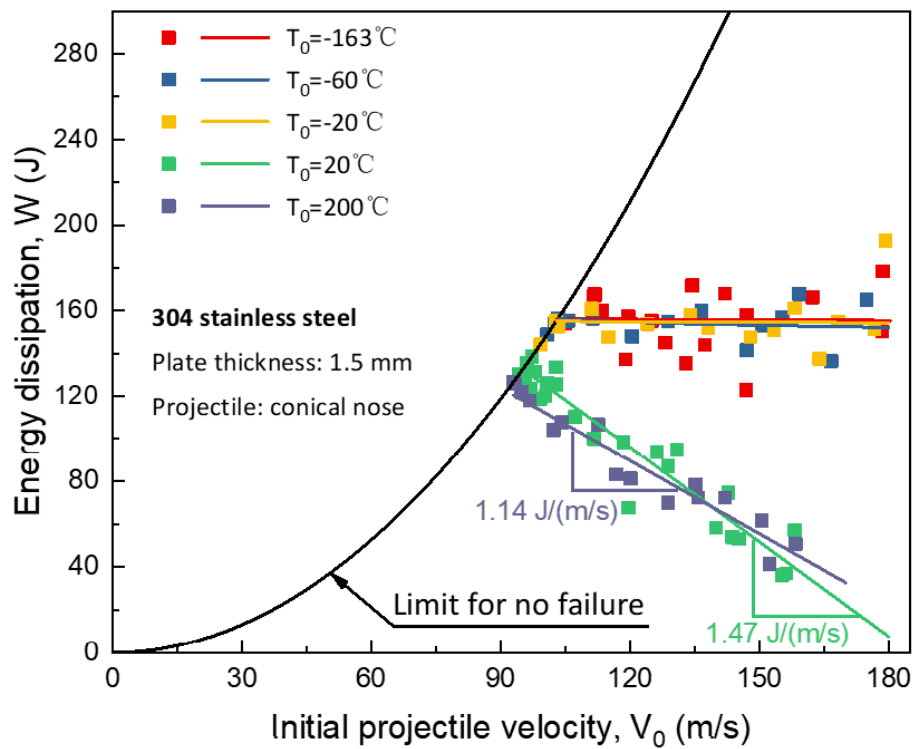


Fig. 4.18. Energy absorbed by the target as a function of the initial projectile velocity for different testing temperatures.

As discussed using Eq. 4.7, a part of the kinetic energy is induced to the plate to generate no perforation, partial or complete perforation depending on the quantity transferred to it. In order to analyze the effect of temperature on energy absorption mechanisms of 304 ASS in more details, the permanent deflection and bending of the impacted specimens at different temperatures was measured, Fig. 4.19. It is clear that the target deflection increases with increasing testing temperature. Plastic

bending of targets is larger at higher temperatures due to thermal softening [15]. This is further verified by petal thickness measurement.

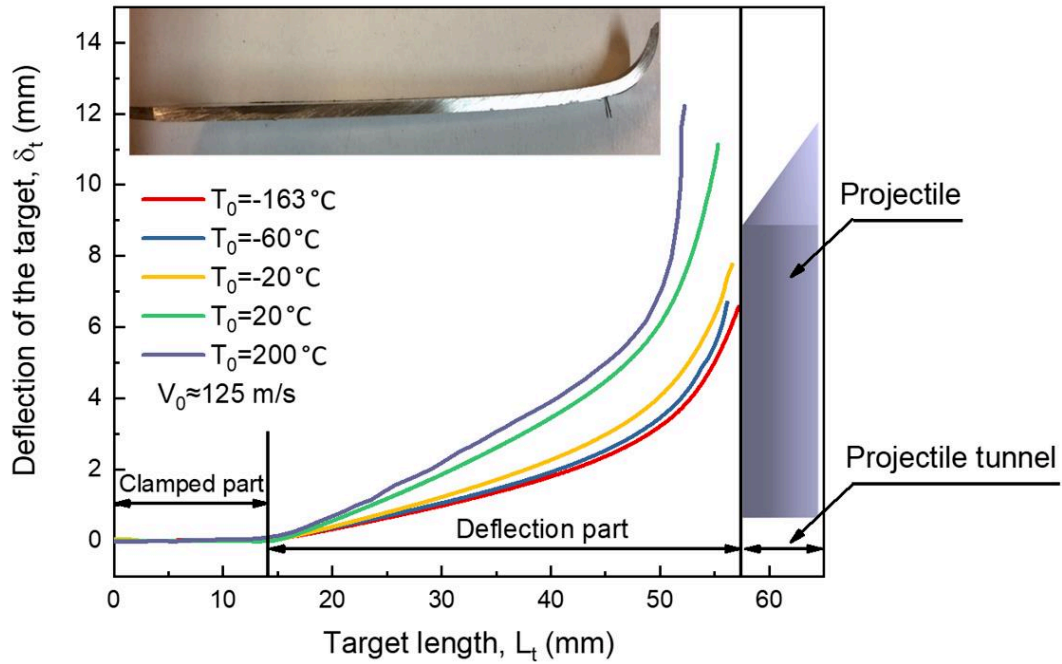


Fig. 4.19. Deflection of post mortem specimens tested at around 125 m/s under different temperatures.

To study the evolution of petal thickness with testing temperature, the perforated specimens at impact velocity around 146 m/s were cut and then the thickness of the petals was measured. As shown in Fig. 4.20, with increasing testing temperature from -163°C to 20°C , the thickness first remains constant at around 1.26 mm and then decreases continuously to 0.60 mm (the initial plate thickness t_0 was 1.5 mm). A smaller thickness at high temperatures indicates a bigger plastic strain to fracture and therefore a larger plastic deformation of the specimens [16].

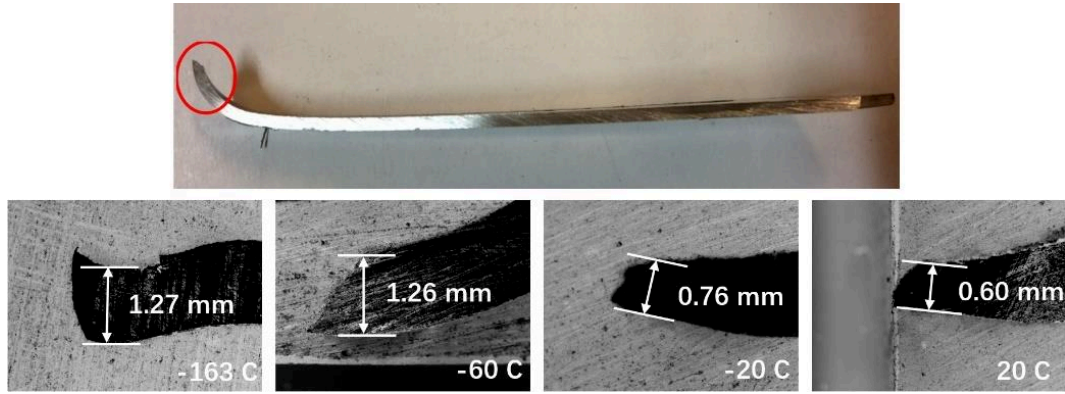


Fig. 4.20. The thickness of the petals under different initial testing temperatures,
 $t_0=1.5$ mm.

Although the plastic deformation of specimens declines with decreasing temperature, the targets absorb more energy at lower temperatures. Therefore, it is supposed that the improved energy absorption capacity of 304 ASS at low temperatures comes from its temperature sensitivity or the SIMT effect. According to martensite fraction measurement (presented in the next section), much martensite was found in the petal area under low temperatures. Hence, different from the results of Rodríguez-Martínez [14], the improved energy absorption of 304 ASS at low temperatures is related not only to the temperature sensitivity but also the SIMT effect.

5. X-ray diffraction analysis of perforated specimens

A notable phenomenon during the deformation process of 304 ASS is martensitic transformation. The transformation helps to increase not only the flow stress but also the ductility of the material. This phenomenon is often observed during quasi-static deformation tests of 304 ASS. However, studies concerning SIMT under impact loading are rarely published. To verify if martensitic transformation occurs during ballistic impact tests and also to study its influence on the perforation behavior of 304 ASS, the volume fraction of martensite was

measured in post mortem specimens by X-ray diffraction (XRD) technique.

After perforation, the microstructure of specimens changed from pure austenite to a combination of martensite α' (body-centered tetragonal phase) and austenite γ (face-centered cubic phase). The volume fraction of each phase is proportional to the integrated diffraction peak intensity. Hence, using a portable PROTO goniometer, Fig. 4.21, and by considering the integrated X-ray diffraction intensities of the two phases, the volume fraction of each phase is determined by Eq. 4.8 to 4.10.

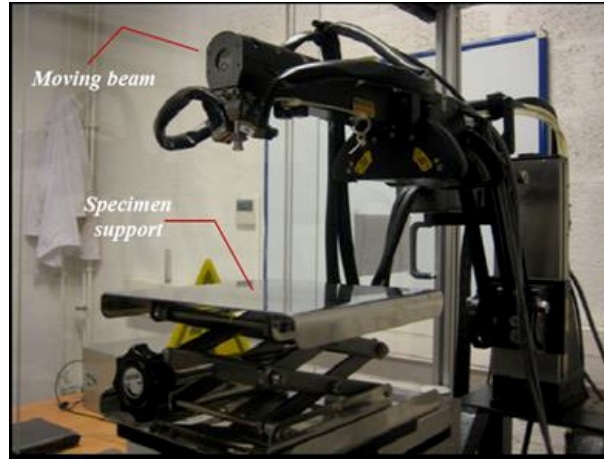


Fig. 4.21. Portable PROTO goniometer used for XRD measurement.

$$V_{\alpha'} = \frac{I_{\alpha'}/R_{\alpha'}}{[(I_{\alpha'}/R_{\alpha'}) + (I_{\gamma}/R_{\gamma})]} \quad \text{Eq. 4.8}$$

$$V_{\gamma} = \frac{I_{\gamma}/R_{\gamma}}{[(I_{\alpha'}/R_{\alpha'}) + (I_{\gamma}/R_{\gamma})]} \quad \text{Eq. 4.9}$$

$$V_{\alpha'} + V_{\gamma} = 1 \quad \text{Eq. 4.10}$$

where $I_{\alpha'}$ and I_{γ} are the integrated diffraction peak areas of martensite and austenite phases, respectively. $R_{\alpha'}$ and R_{γ} are parameters depending on the phase composition, crystal structure, interplanar spacing (hkl) and the Bragg angle. Two peaks for each phase were considered: $\{211\}$ and $\{200\}$ for martensite, $\{220\}$ and $\{200\}$ for austenite [17].

Martensitic transformation occurs in 304 ASS under certain conditions: it usually affects deformation and fracture behavior significantly. Martensite is often observed in austenite stainless steel under quasi-static strain rate or cryogenic temperatures. However, for martensitic transformation under dynamic loading, few studies can be found [18,19]. To investigate its influence on perforation behavior of 304 ASS, martensite distribution in perforated specimens under different temperatures was measured by X-ray diffraction technique. First, the plates impacted at around 146 m/s under -163°C, -60°C, -20°C and 20°C were cut, Fig. 4.22. The parameter M_d is the temperature above which no martensitic transformation occurs even with large plastic deformation [20]: it is measured for our material to be 140°C. Hence, there is no martensite formed for perforation tests at 200°C (hence not considered). Then, martensite fraction on the fracture surface of the petals, Fig. 4.22 (a), and along the cross-section of the plates, Fig. 4.22 (b), was measured.

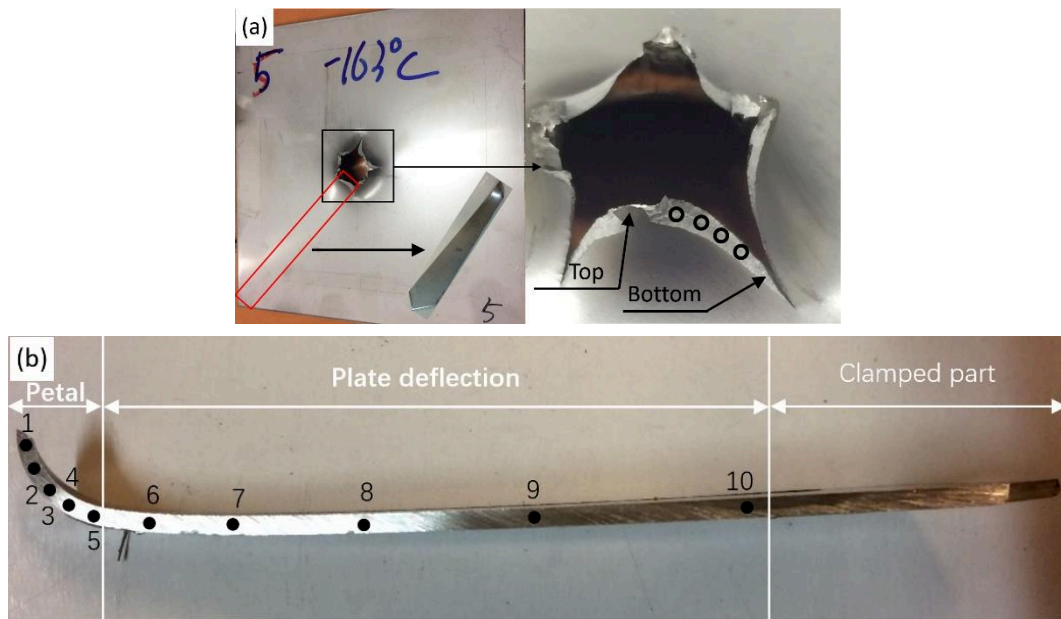


Fig. 4.22. Martensite measurement positions of the perforated specimens: (a) on the fracture surface of the petals and (b) along the cross-section of the plates.

Martensite fraction on the fracture surface of the petals is shown in Fig. 4.23 (a). It is clear that the martensite fraction decreases with increasing testing

temperature. A high amount of martensite of 87.1% was found at -163°C and this value decreases continuously to 32.4% at 20°C. As martensitic transformation is pretty sensitive to temperature, lower transformation rate at higher temperatures is often observed in quasi-static tension or shear tests [21-24].

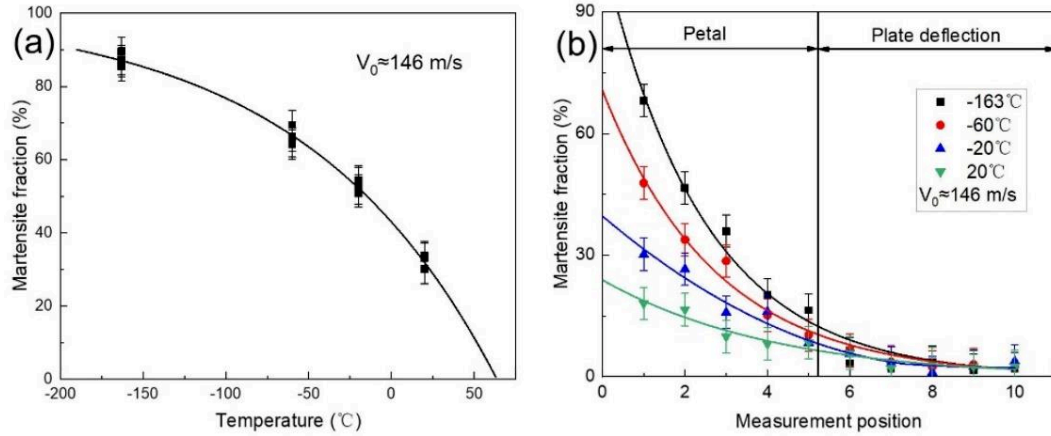


Fig. 4.23. Martensite fraction distribution measured for the perforated specimens: (a) on the fracture surface of the petals and (b) along the cross-section of the plates.

The martensite distribution along the cross-section of the plates is shown in Fig. 4.23 (b). Transformation occurs mainly in the petals: the quantity of martensite in the deflection zone is comparatively lower. With increasing temperature from -163°C to 20°C, the martensite fraction in the petals decreases continuously whereas the value is almost constant in the deflection zones. What is more, in the petals, the martensite fraction decreases quickly from the top to the bottom: compared to the martensite fraction on the fracture surface, martensite inside is obviously lower. This is mainly because the fracture surface corresponds to the maximum plastic deformation until failure while plastic deformation inside the petals is comparatively smaller.

6. Numerical simulations of the perforation process

To validate the experimental results in Chapter 2 and also to study the perforation behavior of 304 ASS in more details, numerical simulations of the perforation process of 304 ASS at different temperatures have been conducted. Limited by the prediction capacity of the extended RK model, only experimental results in the temperature range of -60°C and 200°C were validated while the results at -163°C is not taken into consideration.

6.1 Numerical model description

A 3D full size finite element (FE) model consisting of the projectile and the target has been built using software ABAQUS/Explicit, Fig. 4.24. The geometry and dimensions of the target are the same as the experimental ones. The target is set as a deformable body, and the constitutive behavior is characterized by the previously defined RK model and the corresponding model parameters. To reduce calculation time, the projectile is regarded as a rigid body with a constant mass of 29 g. The four edges of the plates were fixed and no displacement is allowed. The conical shape projectile was placed perpendicular to the target with a predefined velocity. For contact between the projectile and the target, penalty method with a friction coefficient of 0.1 is adopted, a value frequently used for dry steel-steel contact. The perforation process is regarded as adiabatic, no heat transfer between the target and the projectile or the surrounding environment is taken into consideration.

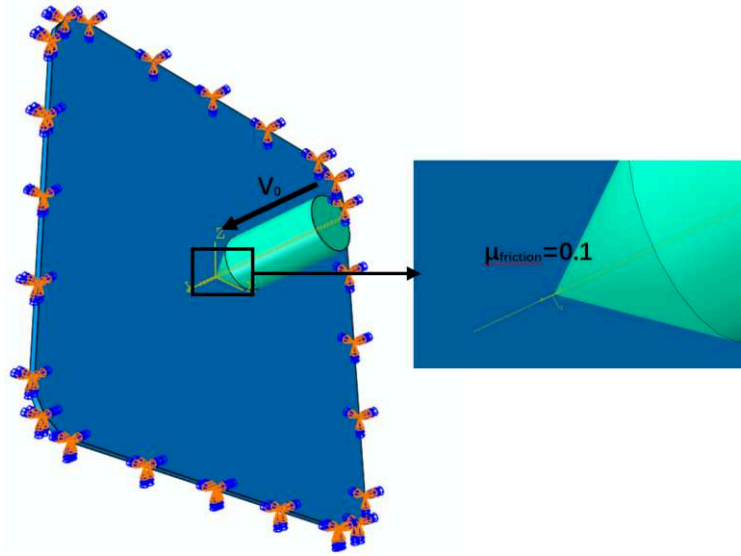


Fig. 4.24. The 3D full size finite element (FE) model consisting of the projectile and the target.

ALE adaptive meshing is commonly used in Abaqus/Explicit to simulate large deformation problems. It is an important technique to maintain a high quality mesh during the analysis. A comparison between two simulations with and without ALE adaptive meshing while the other boundary conditions remaining the same are shown in Fig. 4.25 and Fig. 4.26. Although in both Fig. 4.25 (a) and (b), the targets fail under the same equivalent plastic strain, the fracture patterns are completely different: with the ALE adaptive meshing technique, fracture occurs with 4 petals and each petal has a regular shape, the fracture surface is smooth. Without this technique, the fracture patterns become irregularly shaped and the fracture surfaces are pretty rough. In addition, much debris is observed, a phenomenon inconsistent with experiments. Affected by the different failure process with or without ALE adaptive meshing, the evolutions of projectile velocity are also different: with the ALE adaptive meshing technique, the velocity decrease is comparatively smaller, indicating a better ballistic impact resistance. In order to reproduce the perforation process accurately, ALE adaptive meshing technique is used in all the numerical models.

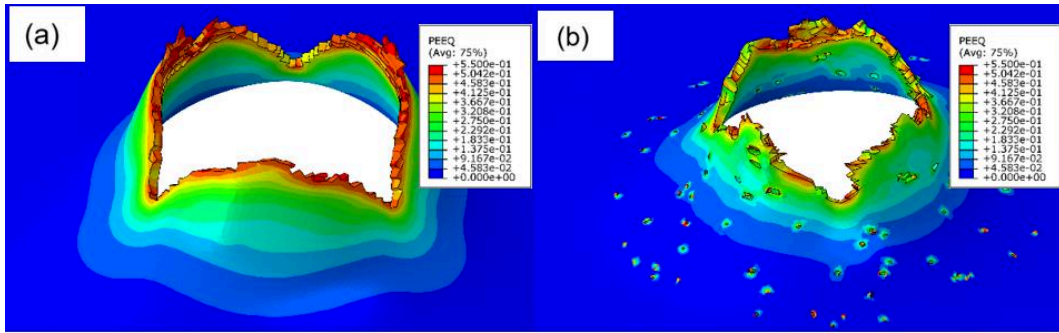


Fig. 4.25. Fracture patterns of perforated specimens (a) with and (b) without the ALE adaptive meshing technique.

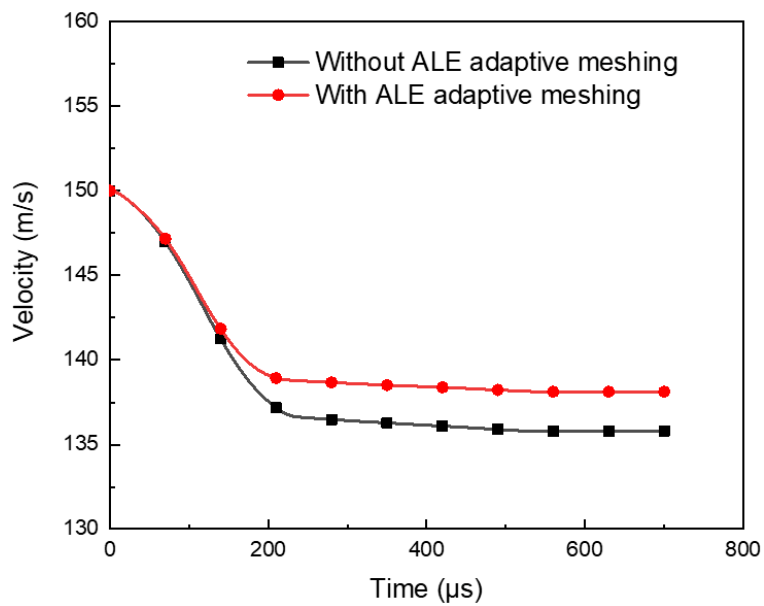


Fig. 4.26. Evolution of the projectile velocity with or without the ALE adaptive meshing technique.

The mesh dependency of the numerical simulations is studied by carrying out computations of the ballistic limit velocity using various mesh densities. Fig. 4.27 shows the relationship between the ballistic limit velocity and the mesh density across the target thickness. It can be seen that under all the four temperatures, the evolution of the ballistic limit velocity with the mesh density along the target thickness is similar: the values keep increasing up to 5 or 6 elements, and after that it becomes almost constant. Fig. 4.28 shows the evolution of the ballistic limit velocities with the element size in the central zone of the plates (a radius of 15 mm)

at different initial testing temperatures. With the increasing element size from 0.05 mm to 0.2 mm, the ballistic limit velocities remain constant or decrease slightly. With further increase of element size from 0.2 mm to 0.6 mm, the ballistic limit velocities decrease obviously. Considering the consumption of computational resource is proportional to the total number of elements, the element size in the central zone is selected as 0.2 mm.

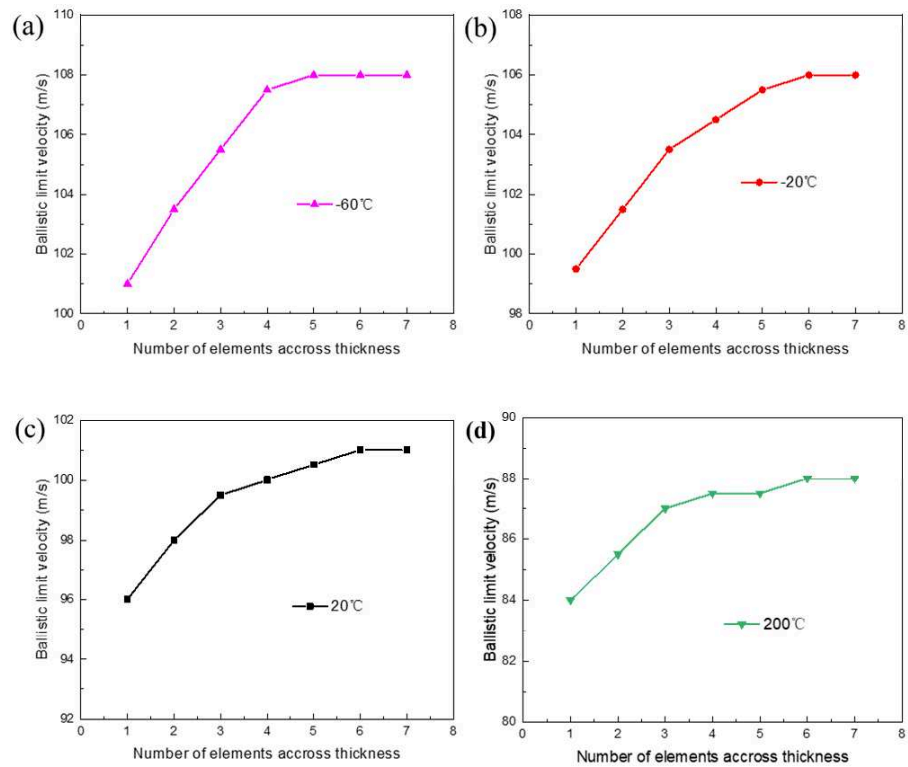


Fig. 4.27. Evolution of the ballistic limit velocities with the number of elements along the target thickness direction at (a) -60°C, (b) -20°C, (c) 20°C and (d) 200°C.

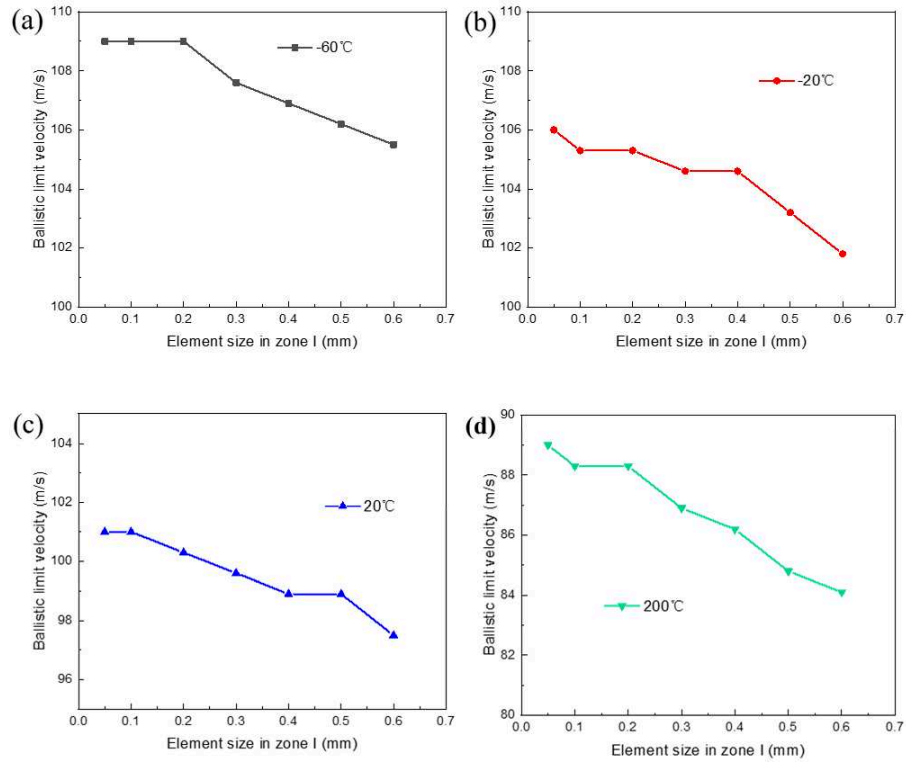


Fig. 4.28. Evolution of the ballistic limit velocities with the element size in zone I at (a) -60°C , (b) -20°C , (c) 20°C and (d) 200°C .

According to the mesh convergence study, the optimal density distribution is shown in Fig. 4.29. The central part is built with 107380 8-node linear bricks, reduced integration element, C3D8R with an initial element size of 0.2 mm. In the exterior area, where no projectile/target impact occurs, C3D8R elements with an initial element size of 1.5 mm were adopted. In the whole areas, five elements across the thickness direction were used. This mesh density is recommended by several authors when modeling ballistic impact behavior of thin metallic structures [7,18].

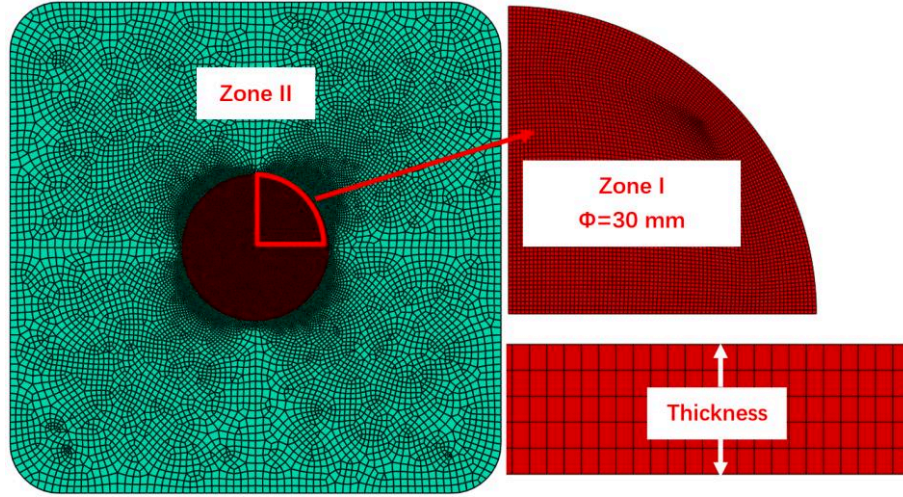


Fig. 4.29. Mesh density distribution in numerical simulations.

To capture fracture patterns of the targets, a failure criterion with element deletion is necessary. According to the work of Kpenyigba et al [7], a constant failure strain for each projectile shape is able to produce numerical results in good agreement with experiments. In this work, a constant value of equivalent plastic strain is assumed as the failure strain for each testing temperature. Based on a process of ballistic curves optimization for all the tested projectile velocities, the failure strains for different testing temperatures have been estimated, Table. 4.2.

The evolution of the failure strain under different temperatures is fitted by the Johnson-Cook type damage model: $\varepsilon_f = a + b * \frac{(T-T_0)}{(T_m-T_0)}$ and values of a and b are found to be 0.52 and 0.93, respectively, Fig. 4.30. The failure strains at different temperatures are then compared to the values used in the study of Pham and Iwamoto [25]. An obvious difference is observed between the two models. This is may be caused by the different mechanical properties of the two kinds of materials such as grain size and chemical composition. Another possible explanation is that the parameters of the failure model in [25] is defined under comparatively lower strain rates, in which the ductility of 304 ASS may be enhanced strongly by the TRIP effect. One thing to be noticed is that the failure strains in both models increases with the

increasing temperatures and the slope of two curves are the same.

Table. 4.2. Failure strain values used to simulate perforation tests depending on the initial testing temperatures.

Testing temperature (°C)	-60	-20	20	200
Failure strain, ϵ_f	0.49	0.55	0.6	0.67

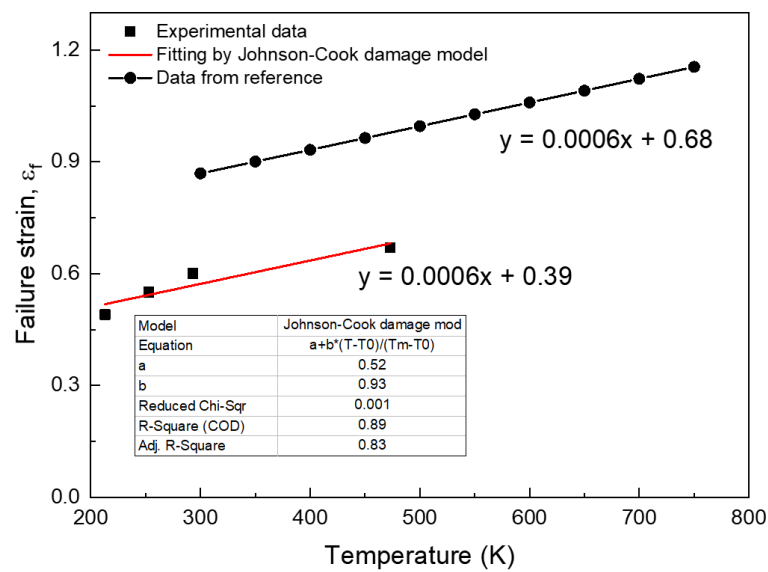


Fig. 4.30. Evolution of failure strain with temperatures.

Based on the boundary conditions mentioned above, numerical simulations of the perforation process at different temperatures have been conducted. In the next section, the numerical results will be presented and compared to the experimental data.

6.2 Numerical results of the ballistic curves and the fracture patterns

A comparison between the experimental and simulated ballistic curves is shown

in Fig. 4.31. It is seen that good agreements are observed for all the four temperatures studied. With the initial testing temperatures increasing from -60°C to -20°C , 20°C and 200°C , the predicted ballistic limit velocities decrease continuously from 108 m/s to 106 m/s, 100 m/s and 87 m/s. The prediction errors of the ballistic limit velocity V_{bl} for the four temperatures are 4.9%, 2.9%, 4.2% and 6.5%, respectively. In addition, the trend of the change of the residual velocity with the initial velocity is also captured by the numerical simulations correctly. Under all the four testing temperatures, the V_R - V_0 curves show a parabolic shape. Fitting the numerical V_R - V_0 curves into Eq. 4.5, values of parameter α at different temperatures are shown in Table. 4.3, and the experimentally fitted α is also shown for easy comparison. In both experiments and numerical simulations, α increases with the increasing initial testing temperatures. The higher α at elevated temperatures indicates the deteriorated ballistic impact resistance and lower ballistic limit velocity. Therefore, the evolution of V_{bl} and α are consistent with each other.

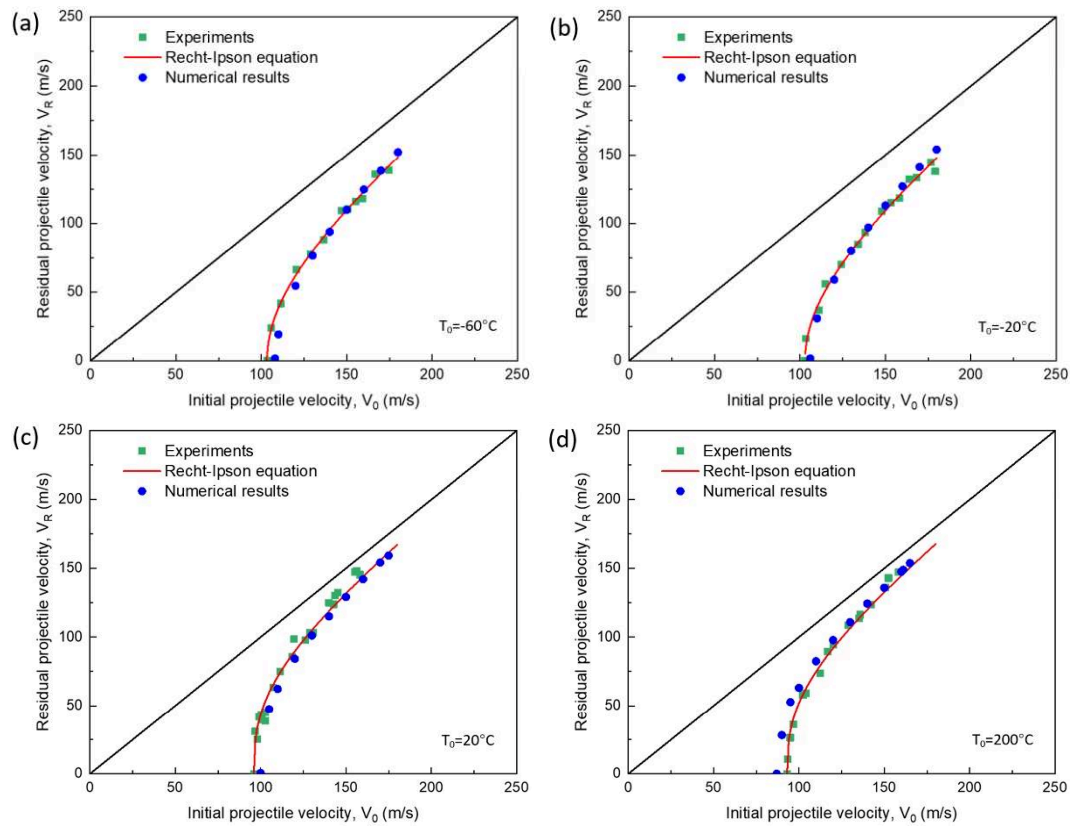


Fig. 4.31. The comparison of ballistic curves between experiments and numerical

simulations: (a), -60°C, (b) -20°C, (c) 20°C and (d) 200°C.

Table. 4.3. Parameter α under different testing temperatures in both experiments and numerical simulations.

Initial testing temperature (°C)	-60	-20	20	200
Values of α using experimental V_R-V_0	2.285	2.239	2.713	2.766
Values of α using numerical V_R-V_0	2.028	2.005	2.712	2.660

For a complete validation of the numerical simulations, the predicted failure mode is compared to the experimental ones, Fig. 4.32. It is seen that petalling resulting from radial necking during the piercing process is the failure mode, the same as is observed during experiments. Plastic deformation is only observed in the petals of the perforated specimens, especially on the fracture surface of the petals where the materials experienced the largest deformation until failure. Compared to the petals, plastic deformation of the other parts of the specimens is pretty limited, with a maximum value of 1.1% under different initial testing temperatures. The distribution of equivalent plastic strain explained why martensite fraction was observed only in the petals while the phase fraction in the other parts of the specimens was very low.

The number of petals varies under different temperatures. A comparison of the number of petals between experiments and numerical results is shown in Table. 4.4. During numerical simulations, the number of petals decreases continuously from 6 at -60°C to 4 at 200°C, while in experiments a similar tendency is observed but the corresponding values are comparatively smaller. In any case, to have a better understanding of the failure mode, further study on the failure behavior of 304 ASS as a function of strain rate, temperature and stress state is necessary.

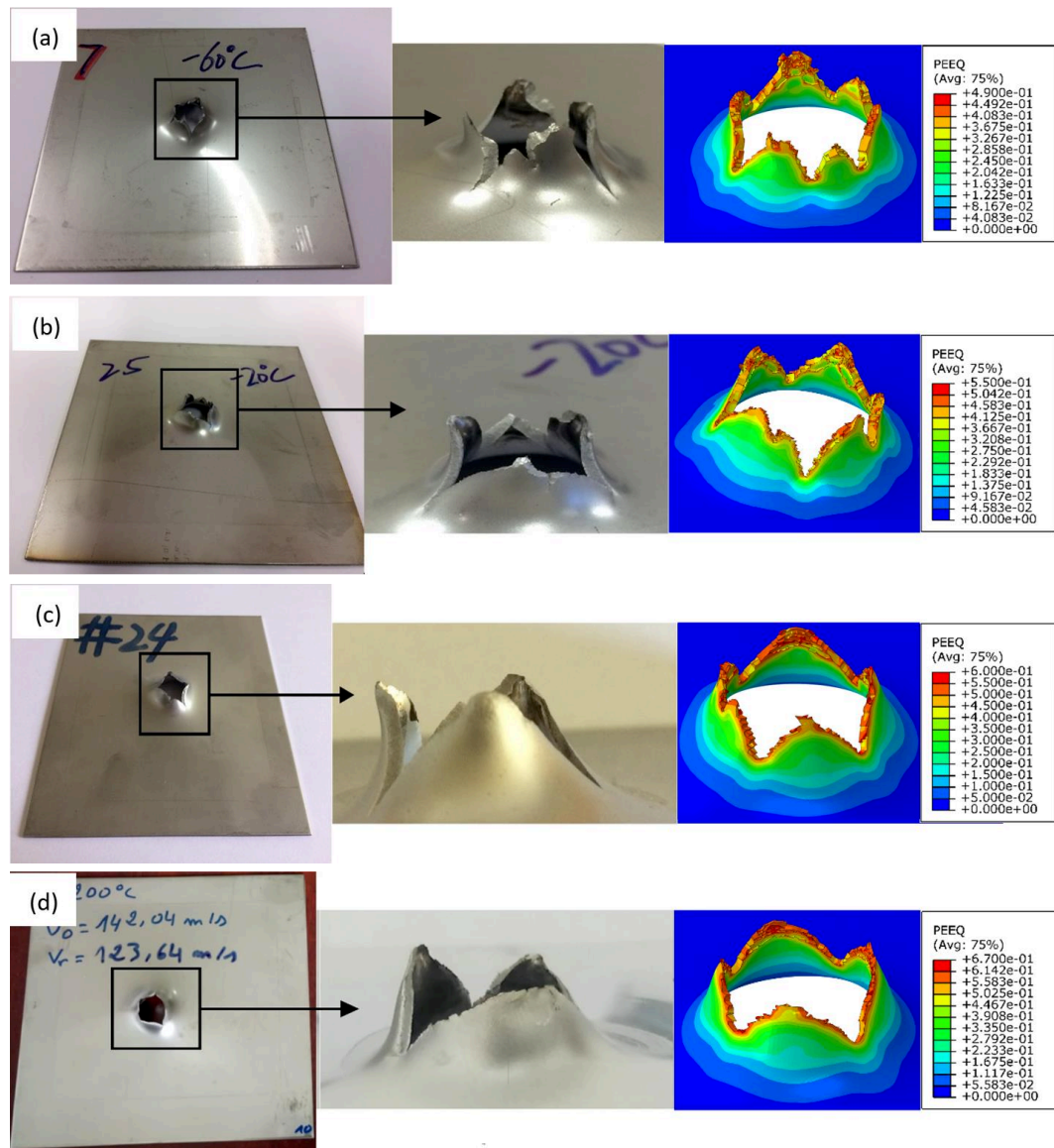


Fig. 4.32. Comparison of fracture pattern between experiments and numerical simulations: (a) -60°C, (b) -20°C, (c) 20°C and (d) 200°C.

Table. 4.4. Experimental and numerical results of the number of petals as a function of the initial testing temperatures, $V_0=110$ m/s.

Testing temperature (°C)	-60	-20	20	200
Experiment	5	4	3	3
Numerical simulation	6	5	4	4

The perforation process is regarded as adiabatic during which an obvious temperature rise is normally observed. Therefore, the temperature distribution in perforated specimens is analyzed. It can be seen from Fig. 4.33 that the distribution of temperature is similar to the distribution of equivalent plastic strain shown in Fig. 4.32. Adiabatic temperature rise occurs mainly in the petals, while temperature of the deflection and the clamped part of the specimens remain unchanged. Especially, the highest temperature is observed on the fracture surfaces of the petals, corresponding to areas with the largest plastic deformation. The maximum temperature rises are 152°C, 171°C, 197°C and 202°C for initial testing temperatures -60°C, -20°C, 20°C and 200°C, respectively. The value is higher at elevated initial testing temperatures. This is closely related to the evolution of failure strain with the testing temperature.

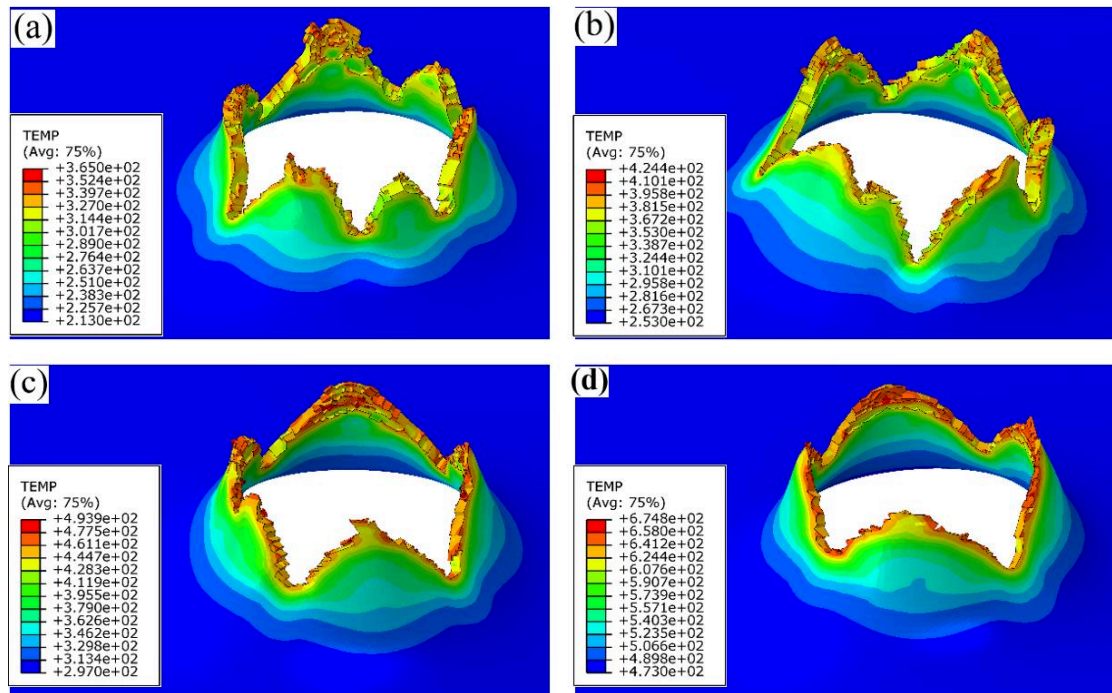


Fig. 4.33. Temperature distribution in perforated specimens under different initial testing temperatures: (a) -60°C, (b) -20°C, (c) 20°C and (d) 200°C.

In addition, the temperature evolution of elements along the fracture surface of petals, Fig. 4.34, is further analyzed and the results are shown in Fig. 4.35. It is seen

that for all the four initial testing temperatures, from the tip to the bottom of petals, the rate of temperature rise decreases continuously. This is because during the perforation process the projectile velocity declines gradually. What's more, the rate of temperature rise is also different at various initial testing temperatures. Due to the improved flow stress at lower temperatures, more plastic work is converted into heat, so the corresponding rate of temperature rise is enhanced.

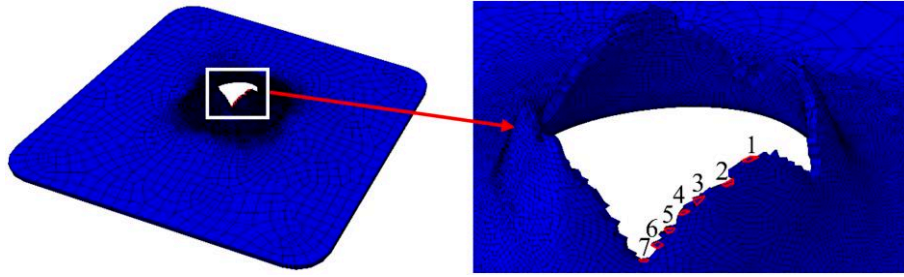


Fig. 4.34. Selected elements from the tip to the bottom of failure petals in perforated specimens.

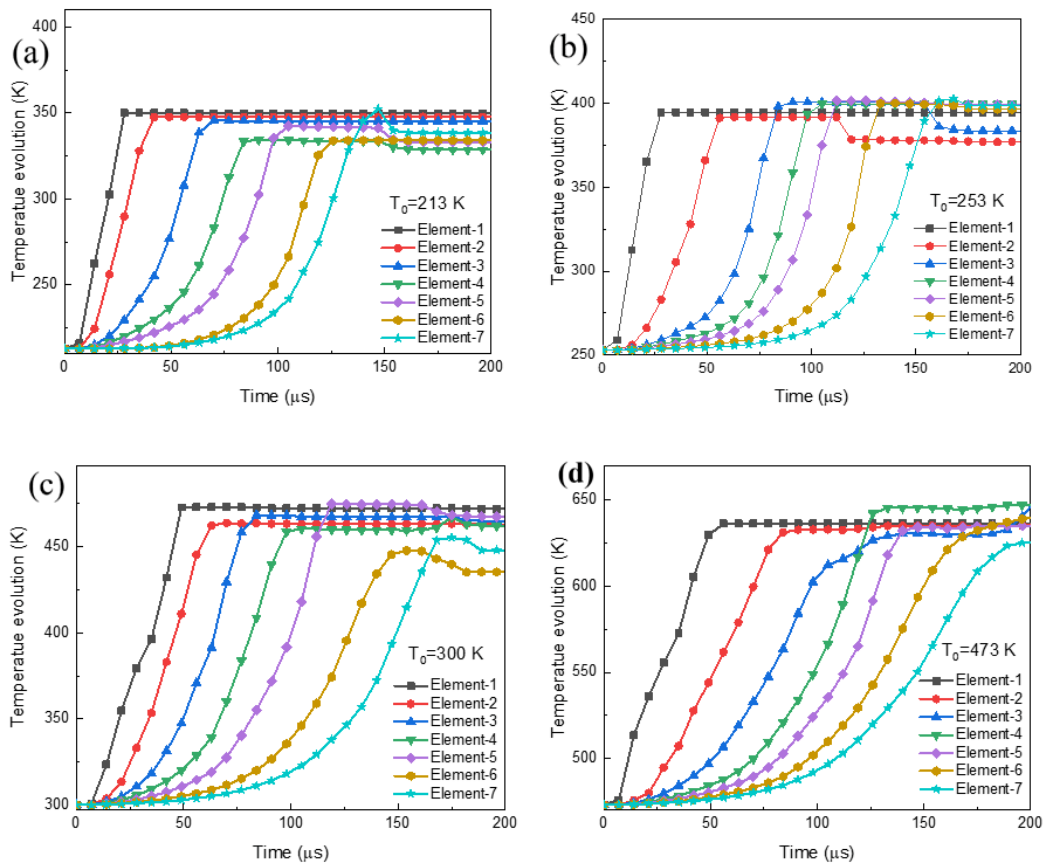


Fig. 4.35. Temperature evolution along the fracture surface of petals under different initial testing temperatures: (a) -60°C, (b) -20°C, (c) 20°C and (d) 200°C.

7. Conclusions

With a newly developed cooling device for ballistic impact device, the influence of the temperature on perforation behavior of thin 304 ASS plates impacted by a conical projectile in the velocity range of 80 and 180 m/s was studied. Based on experimental observations, the following conclusions are drawn:

The cooling device helps to perform perforation tests at low temperatures ranging from -163°C to -20°C. The temperature uniformity on the plate surface is verified both experimentally and by numerical simulations. After a waiting time of 1200 s, the maximum temperature fluctuations on the plate surface are 2°C, 3°C, 4°C and 8°C for testing temperatures -20°C, -40°C, -60°C and -163°C, respectively; if only the center of the plate (with a radius of 20 mm) where plate deformation mainly occurs is considered, the maximum temperature fluctuations are 0.3°C, 0.4°C, 0.6°C and 1.4°C, respectively.

For the testing temperatures considered, petalling is the failure mode observed. The number of petals increases with decreasing testing temperatures. The average number of petals is 3 at 20°C or 200°C and increases continuously until 5 at -163°C. The shape of the petals is also affected by the testing temperature: it looks like a regular triangle at 20°C and 200°C while it becomes rugged and discontinuous at lower temperatures.

The ballistic limit velocity V_{bl} is affected by testing temperature. It increases slightly from 93 m/s at 200°C to 103 m/s at -20°C and then remains constant at lower temperatures. The ballistic curves V_0 - V_R are also influenced by testing temperature. For 20°C and 200°C, they seem to coincide when the initial projectile velocity is much higher than the ballistic limit velocity; at -20°C, -60°C and -163°C, they are

almost the same and slightly lower than those at 20°C and 200°C.

Although the plastic deformation of the target is smaller at lower testing temperatures, the energy absorption capacity of 304 ASS is obviously higher than at room or high temperatures. A high amount of martensite was observed in the perforated specimens, especially in the petals. The improved energy absorption capacity of 304 ASS at low temperatures comes from not only temperature sensitivity of the material but also the SIMT effect.

The extended RK model and the corresponding model parameters can be used to simulate the perforation behavior of 304 ASS accurately. The numerical results in terms of ballistic curves and fracture patterns were compared to the experimental ones and a good agreement is observed.

References

- [1] Kim J-H, Choi S-W, Park D-H, Lee J-M. Charpy impact properties of stainless steel weldment in liquefied natural gas pipelines: Effect of low temperatures. *Materials & Design* (1980-2015) 2015;65:914–22. doi:10.1016/j.matdes.2014.09.085.
- [2] Park WS, Chun MS, Han MS, Kim MH, Lee JM. Comparative study on mechanical behavior of low temperature application materials for ships and offshore structures: Part I—Experimental investigations. *Materials Science and Engineering: A* 2011;528:5790–803. doi:10.1016/j.msea.2011.04.032.
- [3] Jayahari L, Gangadhar J, Singh SK, Balunaik B. Investigation of high temperature forming of ASS 304 using BARLAT 3-Parameter Model. *Materials Today: Proceedings* 2017;4:799–804. doi:10.1016/j.matpr.2017.01.088.
- [4] Sun G, Du L, Hu J, Zhang B, Misra RDK. On the influence of deformation mechanism during cold and warm rolling on annealing behavior of a 304 stainless

steel. *Materials Science and Engineering: A* 2019;746:341–55. doi:10.1016/j.msea.2019.01.020.

[5] Rusinek A, Bernier R, Boumbimba RM, Klosak M, Jankowiak T, Voyiadjis GZ. New devices to capture the temperature effect under dynamic compression and impact perforation of polymers, application to PMMA. *Polymer Testing* 2018;65:1–9. doi:10.1016/j.polymertesting.2017.10.015.

[6] Fras T, Faderl N, Roth CC, Mohr D. Strikers with different nose shape impacting an armour steel-numerical modelling 2019.

[7] Kpenyigba KM, Jankowiak T, Rusinek A, Pesci R. Influence of projectile shape on dynamic behavior of steel sheet subjected to impact and perforation. *Thin-Walled Structures* 2013;65:93–104. doi:10.1016/j.tws.2013.01.003.

[8] Rodriguez-Millan M, Garcia-Gonzalez D, Rusinek A, Abed F, Arias A. Perforation mechanics of 2024 aluminium protective plates subjected to impact by different nose shapes of projectiles. *Thin-Walled Structures* 2018;123:1–10. doi:10.1016/j.tws.2017.11.004.

[9] Duthil P. Material Properties at Low Temperature. ArXiv:150107100 [Cond-Mat, Physics:Physics] 2015. doi:10.5170/CERN-2014-005.77.

[10] Jankowiak T, Rusinek A, Wood P. A numerical analysis of the dynamic behaviour of sheet steel perforated by a conical projectile under ballistic conditions. *Finite Elements in Analysis and Design* 2013;65:39–49. doi:10.1016/j.finel.2012.10.007.

[11] Recht RF, Ipson TW. Ballistic Perforation Dynamics. *J Appl Mech* 1963;30:384–90. doi:10.1115/1.3636566.

[12] Børvik T, Langseth M, Hopperstad OS, Malo KA. Perforation of 12mm thick steel plates by 20mm diameter projectiles with flat, hemispherical and conical noses:

Part I: Experimental study. *International Journal of Impact Engineering* 2002;27:19–35. doi:10.1016/S0734-743X(01)00034-3.

[13] Nazeer MM, Khan MA, Naeem A, Haq A. Analysis of conical tool perforation of ductile metal sheets. *International Journal of Mechanical Sciences* 2000;42:1391–403. doi:10.1016/S0020-7403(99)00065-X.

[14] Rodríguez-Martínez JA, Pesci R, Rusinek A, Arias A, Zaera R, Pedroche DA. Thermo-mechanical behaviour of TRIP 1000 steel sheets subjected to low velocity perforation by conical projectiles at different temperatures. *International Journal of Solids and Structures* 2010;47:1268–84. doi:10.1016/j.ijsolstr.2010.01.013.

[15] Pérez-Castellanos J-L, Rusinek A. Temperature increase associated with plastic deformation under dynamic compression: Application to aluminium alloy Al 6082. *Journal of Theoretical and Applied Mechanics* 2012;50:377-398–398.

[16] Park WS, Yoo SW, Kim MH, Lee JM. Strain-rate effects on the mechanical behavior of the AISI 300 series of austenitic stainless steel under cryogenic environments. *Materials & Design* 2010;31:3630–40. doi:10.1016/j.matdes.2010.02.041.

[17] Standard A. E975-03: standard practice for x-ray determination of retained austenite in steel with near random crystallographic orientation. ASTM, West Conshohocken, PA 2008.

[18] Rodríguez-Martínez JA, Rusinek A, Pesci R, Zaera R. Experimental and numerical analysis of the martensitic transformation in AISI 304 steel sheets subjected to perforation by conical and hemispherical projectiles. *International Journal of Solids and Structures* 2013;50:339–51. doi:10.1016/j.ijsolstr.2012.09.019.

[19] Zaera R, Rodríguez-Martínez JA, Casado A, Fernández-Sáez J, Rusinek A, Pesci R. A constitutive model for analyzing martensite formation in austenitic steels

deforming at high strain rates. *International Journal of Plasticity* 2012;29:77–101. doi:10.1016/j.ijplas.2011.08.003.

[20] Rodríguez-Martínez JA, Rusinek A, Pesci R. Experimental survey on the behaviour of AISI 304 steel sheets subjected to perforation. *Thin-Walled Structures* 2010;48:966–78. doi:10.1016/j.tws.2010.07.005.

[21] Beese AM, Mohr D. Effect of stress triaxiality and Lode angle on the kinetics of strain-induced austenite-to-martensite transformation. *Acta Materialia* 2011;59:2589–600. doi:10.1016/j.actamat.2010.12.040.

[22] Byun TS, Hashimoto N, Farrell K. Temperature dependence of strain hardening and plastic instability behaviors in austenitic stainless steels. *Acta Materialia* 2004;52:3889–99. doi:10.1016/j.actamat.2004.05.003.

[23] Talonen J, Hänninen H. Formation of shear bands and strain-induced martensite during plastic deformation of metastable austenitic stainless steels. *Acta Materialia* 2007;55:6108–18. doi:10.1016/j.actamat.2007.07.015.

[24] Hamada AS, Karjalainen LP, Misra RDK, Talonen J. Contribution of deformation mechanisms to strength and ductility in two Cr–Mn grade austenitic stainless steels. *Materials Science and Engineering: A* 2013;559:336–44. doi:10.1016/j.msea.2012.08.108.

[25] Pham H T, Iwamoto T. An evaluation of fracture properties of type-304 austenitic stainless steel at high deformation rate using the small punch test[J]. *International Journal of Mechanical Sciences*, 2018, 144: 249-261.

Conclusions

In this work, the deformation behavior of 304 ASS under different strain rates and temperatures has been studied and divided in two parts. The first part focused on different deformation conditions. Two techniques including the commonly used uniaxial compression and a newly developed simple shear method were adopted. In the second part, ballistic impact tests of 304 ASS plates were conducted under different projectile velocities and initial temperatures. On the one hand, the perforation behavior of 304 ASS was investigated; on the other hand, the defined constitutive model was verified.

The bibliography has been studied in chapter 1. The effects of strain rate and temperature on the deformation behavior of 304 ASS have been reviewed. Then representative constitutive models for deformation behavior and martensitic transformation behavior modeling have been introduced, with special focus on the advantages and disadvantages of each model. It was found that the deformation behavior of 304 ASS was influenced by a combination of dislocation slip and martensitic transformation, with different contribution as a function of the deformation conditions.

Chapter 2 presented the compression behavior of 304 ASS under different strain rates and temperatures. Self-designed heating furnace/cooling device were coupled to the conventional SHPB device for dynamic compression tests not only at low but also at elevated temperatures. The stress-strain relations of 304 ASS were obtained experimentally and the effects of strain rate and temperature on the strain hardening was explained. In addition, an extension of the RK model considering martensitic transformation phenomenon was used for constitutive behavior modeling.

In chapter 3, a new shear specimen was designed for the dynamic behavior characterization using the SHPB system within a maximum shear strain rate of

39000 s⁻¹. The technique was validated by both experiments and numerical simulations from several aspects including the specimen repeatability, the force equilibrium state within the specimen and the reliability of strain signal measurement. According to numerical results, the distribution and evolution of stress/strain components in the shear specimen were analyzed. The stress state in the shear zone was found to be simple shear with pretty low stress triaxiality and Lode angle parameter values. Moreover, a correction coefficients method was used to extract the real shear stress-shear strain response from the experimentally obtained force-displacement data. Finally, the shear behavior of 304 ASS under a wide range of shear strain rates (0.001 s⁻¹ to 39000 s⁻¹) and three different temperatures were analyzed. The strain hardening rate and flow stress of 304 ASS were strongly affected by temperature and strain rate. Several phenomena such as enhanced strain rate sensitivity in extremely high strain rates, increasing strain hardening rate at low temperatures and decreasing strain hardening rate with shear strain rates were observed. They were explained according to the thermally activated dislocation motion theory.

Chapter 4 focused on the ballistic impact behavior of 304 steel plates. A cooling device was specially designed for perforation tests at low temperatures. Through experiments and numerical simulations, the temperature distribution on the plate was verified to be uniform. With the cooling device, perforation tests were performed at temperatures between -163°C and 200°C. The effect of temperature was analyzed according to the failure mode, the ballistic curves and the energy absorption capacity, and improved ballistic impact resistance capacity was observed at low temperatures. Based on martensite fraction measurement by X-ray diffraction, the enhanced perforation resistance phenomenon came from not only temperature sensitivity but also the SIMT effect. In addition, the perforation process was simulated using the extended RK model determined in chapter 2 and a good agreement between experiment and numerical results was observed.

Future work

Limited by time, there are still some work remaining to be done.

First, an extension of the RK model was used in this work to simulate the deformation behavior of 304 ASS. A phenomenological item was developed to describe the flow stress increase due to martensitic transformation effect. However, the model works in a limited range of temperature (-60°C to 172°C). When looking at the deformation behavior under even lower temperatures, an obvious difference still exists between the experimental and numerical stress-strain curves. Therefore, a further improvement to describe the martensitic transformation process more accurately is needed.

Second, it was showed that the SSS specimen is valid for simple shear behavior characterization under extremely high strain rates. It would be also interesting to study the failure behavior: the failure morphology characterization will help to understand the deformation process more clearly. Hence, more work is needed to investigate the dynamic failure behavior of 304 ASS using the SSS specimen.

In addition, we used the stop ring technique to study the evolution of martensitic transformation with strain (we can stop the tests with a strain increase of 0.5% step by step). By this way, the effect of strain rate on the transformation process could be decoupled from the adiabatic heating effect. It was observed the martensite fraction under dynamic strain rate was obviously lower than for the quasi-static tests. Hence, martensitic transformation was strongly suppressed by dynamic strain rates, but this was not due to the adiabatic heating effect. Some other mechanisms dominate the transformation process under dynamic strain rates: a deeper insight into the effect of strain rate on the martensitic transformation is necessary.

CARACTERISATION EXPERIMENTALE ET MODELISATION DU COMPOTEMENT DE L'ACIER INOXYDABLE 304 SOUS DIFFERENTES VITESSES DE DEFORMATION ET TEMPERATURES

RESUME : L'acier inox austénitique 304 est utilisé pour de nombreuses applications industrielles, notamment à cause de l'effet TRIP qui lui confère des propriétés particulières. Au cours de son élaboration ou lorsqu'il est utilisé en service, il peut être soumis à différentes vitesses de déformation et températures. Le travail présenté ici vise à étudier le comportement de cet acier sous différents trajets de chargement. Tout d'abord, un système de refroidissement a été ajouté aux barres de Hopkinson pour étudier le comportement de cet acier en compression avec des vitesses de déformation comprises entre 0.001 s^{-1} et 3000 s^{-1} et des températures entre -163°C et 172°C . Le modèle de Rusinek-Klepaczko, qui prend en compte le phénomène de transformation martensitique, a été utilisé en parallèle pour simuler son comportement thermo-viscoplastique. Pour les vitesses de déformation au-delà de 3000 s^{-1} , un nouveau design d'éprouvette de cisaillement a ensuite été proposé et validé et l'effet de la vitesse de déformation entre 3000 s^{-1} et 39000 s^{-1} a été étudié. Enfin, un autre système de refroidissement a été développé pour les essais d'impact et de perforation à différentes vitesses (entre 80 et 180 m.s^{-1}) et températures (entre -163°C et 200°C) et les lois de comportement ont été validées en comparant expériences et simulations numériques.

Mots clés : caractérisation expérimentale, comportement, vitesse de déformation, température, simulation numérique

EXPERIMENTAL CHARACTERIZATION AND BEHAVIOR MODELING OF 304 STAINLESS STEEL UNDER VARIOUS STRAIN RATES AND TEMPERATURES

ABSTRACT : Due to the unique Transformation Induced Plasticity (TRIP) effect, 304 austenitic stainless steel (ASS) is widely used in many engineering areas. During working and manufacturing process or in service, it may undergo deformation over a wide range of strain rates and temperatures. The current work presents a systematic deformation behavior study of 304 ASS by both experiments and numerical simulations. With an original cooling device coupled to the split Hopkinson pressure bar system, the compression behavior at strain rates between 0.001 s^{-1} and 3000 s^{-1} and temperatures between -163°C and 172°C was investigated. An extension of the Rusinek-Klepaczko (RK) model considering strain-induced martensitic transformation (SIMT) phenomenon was also used to simulate the thermo-viscoplastic behavior of this steel. To study the deformation behavior at extremely high strain rates exceeding 3000 s^{-1} , a new single shear zone (SSS) specimen has been proposed and validated. Then, the effects of strain rate between 3000 s^{-1} and 39000 s^{-1} was analyzed. Finally, with a specially designed cooling device, the ballistic impact behavior under initial projectile velocities between 80 and 180 m.s^{-1} and temperatures between -163°C and 200°C was studied. By comparison between experiments and numerical simulations for perforation, the previously obtained constitutive relations were validated.

Keywords : experimental characterization, behavior, strain rate, temperature, numerical simulation

